

STARBURST99: SYNTHESIS MODELS FOR GALAXIES WITH ACTIVE STAR FORMATION

CLAUS LEITHERER

Space Telescope Science Institute,¹ 3700 San Martin Drive, Baltimore, MD 21218; leitherer@stsci.edu

DANIEL SCHAEERER

Observatoire Midi-Pyrenees, 14, Av. E. Belin, F-31400 Toulouse, France; schaeerer@obs-mip.fr

JEFFREY D. GOLDADER

University of Pennsylvania, Department of Physics and Astronomy, Philadelphia, PA 19104-6396; jdgoldad@dept.physics.upenn.edu

ROSA M. GONZÁLEZ DELGADO

Instituto Astrofisica de Andalucía, Apartado 3004, E-18080 Granada, Spain; rosa@iaa.es

CARMELLE ROBERT

Département de Physique and Observatoire du mont Mégantic, Université Laval, Québec, QC, G1K 7P4, Canada; carobert@phy.ulaval.ca

DENIS FOO KUNE²

Macalester College, Department of Physics and Astronomy, 1600 Grand Avenue, St. Paul, MN 55105; dfookune@macalester.edu

DUÍLIA F. DE MELLO

Space Telescope Science Institute, 3700 San Martin Drive, Baltimore, MD 21218; demello@stsci.edu

DANIEL DEVOST³

Space Telescope Science Institute, 3700 San Martin Drive, Baltimore, MD 21218; devost@stsci.edu

AND

TIMOTHY M. HECKMAN

Physics and Astronomy Department, Johns Hopkins University, Homewood Campus, Baltimore, MD 21218; heckman@pha.jhu.edu

Received 1998 September 16; accepted 1999 February 23

ABSTRACT

Starburst99 is a comprehensive set of model predictions for spectrophotometric and related properties of galaxies with active star formation. The models are an improved and extended version of the data set previously published by Leitherer & Heckman. We have upgraded our code by implementing the latest set of stellar evolution models of the Geneva group and the model atmosphere grid compiled by Lejeune et al. Several predictions which were not included in the previous publication are shown here for the first time. The models are presented in a homogeneous way for five metallicities between $Z = 0.040$ and 0.001 and three choices of the initial mass function. The age coverage is 10^6 – 10^9 yr. We also show the spectral energy distributions which are used to compute colors and other quantities. The full data set is available for retrieval at a Web site, which allows users to run specific models with nonstandard parameters as well. We also make the source code available to the community.

Subject headings: galaxies: evolution — galaxies: fundamental parameters — galaxies: starburst — galaxies: stellar content — methods: numerical

1. INTRODUCTION

Synthesis models for comparison with observed galaxy properties, and in particular with spectral energy distributions, have become increasingly popular in recent years. This is partly due to improvements in stellar libraries and models. An overview over the latest achievements can be found in the conference volume edited by Leitherer, Fritze-v. Alvensleben, & Huchra (1996b). At least equally important is the possibility of electronic dissemination of the data, either by CD-ROM or via the internet. Most groups who provide such models to the community make them available electronically. See Leitherer et al. (1996a) for a compilation of a suite of models.

This paper concerns a particular set of synthesis models: models which are optimized to reproduce properties of galaxies with active star formation. In the absence of an active

galactic nucleus, most radiative properties of such galaxies are determined by their massive-star content. The most extreme examples are referred to as starbursts (Weedman et al. 1981; Weedman 1987; Moorwood 1996) but the models in this paper are often applicable to less extreme star-forming regions and galaxies, like 30 Doradus and M33, as well. Leitherer & Heckman (1995, hereafter LH95) published a homogeneous grid of synthetic starburst models. These models, together with those of Bressan et al. and Bruzual & Charlot (both published on the CD-ROM of Leitherer et al. 1996a), Fioc & Rocca-Volmerange (1997), and Cerviño & Mas-Hesse (1994), are widely used to aide the interpretation of galaxy observations.

Although the LH95 models are still recently up-to-date and no major error was found, we decided to generate and release a new generation of models. There are two reasons for this. First, stellar modeling is continuously advancing, and some known shortcomings of the stellar atmosphere and evolution models used in LH95 have been improved. Specifically, we have included the new model atmosphere grid of Lejeune, Buser, & Cuisinier (1997) and the latest Geneva evolutionary tracks in our code. Other modifications include the possibility to perform isochrone synthe-

¹ Operated by AURA for NASA under contract NAS 5-26555.

² Space Telescope Science Institute, 3700 San Martin Drive, Baltimore, MD 21218.

³ Département de Physique and Observatoire du mont Mégantic, Université Laval, Québec, QC, G1K 7P4, Canada.

sis, a technique that was pioneered by Charlot & Bruzual (1991).

The second motivation for an update to LH95 concerns the distribution method. While the LH95 data set is unofficially available via our Web site, the principal publication is on paper. Many users found this inconvenient and encouraged us to publish fully electronically. Therefore, we decided not to include any tables with model predictions and only a subset of the figures in the print edition of this paper.⁴ The full data set with all the figures is available in the electronic edition of the journal.

The organization of the paper is as follows: In § 2 we outline our computation technique, the model assumptions, and the improvements over LH95. This section also explains how to reach our Web site and how to navigate. The spectral energy distributions are presented in § 3. Spectral line profiles in the ultraviolet (UV) are discussed in § 4. In § 5 we provide numbers for the stellar inventory. Luminosities and colors are in §§ 6 and 7, respectively. Properties related to the far-UV are presented in § 8. Some other useful diagnostic lines are in § 9. Section 10 covers the mass and energy return of a stellar population. We conclude with § 11.

2. MODEL ASSUMPTIONS AND COMPUTATIONAL TECHNIQUE

The present model set is an extension of our previous work which was published in several papers. Most of the earlier tables are in LH95. The energy distributions used in LH95 were made available electronically in Leitherer et al. (1996a) and on our Web site. Ultraviolet spectra between 1200 and 1850 Å at 0.75 Å resolution were originally published in Leitherer, Robert, & Heckman (1995) and distributed electronically in Leitherer et al. (1996a). A set of spectra around O VI λ 1035 and Ly β was discussed by González Delgado, Leitherer, & Heckman (1997). All mentioned models have been recomputed and included in the present database. The covered parameter space is similar to the one in LH95. Since arguments are given in LH95 for the choice of these particular parameters, we will be brief and only address those issues in more detail which are different from LH95.

We consider two limiting cases for the *star formation law*: an instantaneous burst of star formation and star formation proceeding continuously at a constant rate. The instantaneous models (also referred to as a single stellar population) are normalized to a total mass of $10^6 M_{\odot}$. The star formation rate of the continuous model is $1 M_{\odot} \text{ yr}^{-1}$. These normalizations were chosen to produce properties that are typical for actual star-forming regions in galaxies.

As we did in LH95, we offer three choices for the *stellar initial mass function* (IMF). The reference model is a power law with exponent $\alpha = 2.35$ between low-mass and high-mass cutoff masses of $M_{\text{low}} = 1 M_{\odot}$ and $M_{\text{up}} = 100 M_{\odot}$, respectively. This approximates the classical Salpeter (1955) IMF. Most observations of star-forming and starburst regions are consistent with a Salpeter IMF—although the uncertainties can be large (Leitherer 1998; Scalo 1998). For comparison, we also show the results for an IMF with $\alpha = 3.3$ between 1 and $100 M_{\odot}$, which has a higher propor-

tion of low-mass stars. Finally, we computed models with a truncated Salpeter IMF: $\alpha = 2.35$, $M_{\text{low}} = 1 M_{\odot}$, $M_{\text{up}} = 30 M_{\odot}$. The models can easily be renormalized to other M_{low} -values. The lower mass cutoff is often only a scaling factor since low-mass stars have a negligible contribution to the properties of the stellar population, except for the mass locked into stars. Absolute quantities (such as, e.g., the number of ionizing photons) can be rescaled to other M_{low} -values by multiplying our results by factors of 0.39, 1.00, 1.80, 3.24 for $M_{\text{low}} = 0.1, 1.0, 3.5, 10 M_{\odot}$. Relative quantities (like colors) should, of course, not be scaled. Note that $10 M_{\odot}$ stars are no longer negligible for many model predictions, and the models should be recalculated for this cutoff mass, rather than scaling the existing data. Common sense is necessary when applying this scaling factor to instantaneous models in particular. The lifetime of a $2 M_{\odot}$ star is only somewhat above 1 Gyr. Therefore, burst models at 1 Gyr are actually only represented by a population of 1–2 M_{\odot} stars. Clearly even a small change of the lower mass cutoff will drastically alter the model predictions.⁵

We have implemented the new set of *stellar evolution models* of the Geneva group—as opposed to the Maeder (1990) models in LH95. For masses of 12–25 M_{\odot} (depending on metallicity) and above we are using the tracks with enhanced mass loss of Meynet et al. (1994). The tracks of Schaller et al. (1992), Schaerer et al. (1993a, 1993b), and Charbonnel et al. (1993) with standard mass loss are used between 12 and $0.8 M_{\odot}$. We have favored the enhanced mass-loss models over the standard ones because they are a better representation of most Wolf-Rayet (WR) star properties, except for the mass-loss rate (\dot{M}) itself. The high mass-loss rates of WR stars are in conflict with observations (Leitherer, Chapman, & Koribalski 1995). This may suggest the lack of one or another ingredient in the evolution models, like rotation-induced mixing processes (Maeder 1995). The evolutionary tracks do not take into account binary evolution. Inclusion of Roche-lobe overflow in binary systems can modify some of the predictions, in particular during the WR phase. Models taking these effects into account were computed by Cerviño, Mas-Hesse, & Kunth (1997), Vanbeveren, Van Bever, & de Donder (1997), Schaerer & Vacca (1998), and Dionne (1999).

The Geneva models include the early asymptotic giant branch (AGB) evolution until the first thermal pulse for masses greater than $1.7 M_{\odot}$. Stellar evolution models in the AGB phase are rather dependent on input assumptions and therefore quite uncertain. A recent comparison between different sets of AGB models was made by Girardi & Bertelli (1998).

Five *metallicities* are available: $Z = 0.040, 0.020 (= Z_{\odot}), 0.008, 0.004$, and 0.001 . These are the metallicities of the evolutionary models. All element and isotope ratios are independent of metallicity. Note that we do not treat chemical evolution self-consistently: each stellar generation has the same metallicity during the evolution of the population. The error introduced by this simplification is negligible as long as star formation proceeds for less than about 1 Gyr, otherwise self-consistent models are needed, such as those by Möller, Fritze-v. Alvensleben, & Fricke (1997).

The models cover the *age range* 10^6 – 10^9 yr. In principle we could have evolved the populations up to a Hubble time,

⁴ The reader should visit the Web site at <http://www.stsci.edu/science/starburst99/> to view the figures and to download the tables. Moreover, this Web site offers the opportunity to run tailored models remotely and to access our source code. The reader should use this paper as a guide when visiting our Web page.

⁵ A typographical error was introduced in eq. (3) of LH95: the numerator should be 0.80 instead of -0.35 .

TABLE 1
LIST OF MODELS

Topic	Quantity	Star Formation	Metallicity	IMF ³	Figure
Stellar continua	Stellar + nebular continuum	Instantaneous	0.040–0.001	2.35	1
	Stellar + nebular continuum	Continuous	0.040–0.001	2.35	2
	Stellar + nebular continuum	Instantaneous	0.040–0.001	3.3	3
	Stellar + nebular continuum	Continuous	0.040–0.001	3.3	4
	Stellar + nebular continuum	Instantaneous	0.040–0.001	30	5
	Stellar + nebular continuum	Continuous	0.040–0.001	30	6
	Stellar continuum only	Instantaneous	0.040–0.001	2.35	7
	Stellar continuum only	Continuous	0.040–0.001	2.35	8
	Stellar continuum only	Instantaneous	0.040–0.001	3.3	9
	Stellar continuum only	Continuous	0.040–0.001	3.3	10
	Stellar continuum only	Instantaneous	0.040–0.001	30	11
	Stellar continuum only	Continuous	0.040–0.001	30	12
UV line spectra	Rectified spectra	Instantaneous	0.020	2.35	13
	Rectified spectra	Continuous	0.020	2.35	14
	Spectra in ergs s ⁻¹ Å ⁻¹	Instantaneous	0.020	2.35	15
	Spectra in ergs s ⁻¹ Å ⁻¹	Continuous	0.020	2.35	16
	Rectified spectra	Instantaneous	0.020	3.3	17
	Rectified spectra	Continuous	0.020	3.3	18
	Spectra in ergs s ⁻¹ Å ⁻¹	Instantaneous	0.020	3.3	19
	Spectra in ergs s ⁻¹ Å ⁻¹	Continuous	0.020	3.3	20
	Rectified spectra	Instantaneous	0.020	30	21
	Rectified spectra	Continuous	0.020	30	22
	Spectra in ergs s ⁻¹ Å ⁻¹	Instantaneous	0.020	30	23
	Spectra in ergs s ⁻¹ Å ⁻¹	Continuous	0.020	30	24
O VI λ 1035 + Ly β	Rectified spectra	Instantaneous	0.020	2.35	25
	Rectified spectra	Continuous	0.020	2.35	26
	Spectra in ergs s ⁻¹ Å ⁻¹	Instantaneous	0.020	2.35	27
	Spectra in ergs s ⁻¹ Å ⁻¹	Continuous	0.020	2.35	28
	Rectified spectra	Instantaneous	0.020	3.3	29
	Rectified spectra	Continuous	0.020	3.3	30
	Spectra in ergs s ⁻¹ Å ⁻¹	Instantaneous	0.020	3.3	31
	Spectra in ergs s ⁻¹ Å ⁻¹	Continuous	0.020	3.3	32
	Rectified spectra	Instantaneous	0.020	30	33
	Rectified spectra	Continuous	0.020	30	34
	Spectra in ergs s ⁻¹ Å ⁻¹	Instantaneous	0.020	30	35
	Spectra in ergs s ⁻¹ Å ⁻¹	Continuous	0.020	30	36
Stellar inventory	Number of O stars	Instantaneous	0.040–0.001	2.35, 3.3, 30	37
	Number of O stars	Continuous	0.040–0.001	2.35, 3.3, 30	38
	WR/O stars	Instantaneous	0.040–0.001	2.35, 3.3, 30	39
	WR/O stars	Continuous	0.040–0.001	2.35, 3.3, 30	40
	WC/WN stars	Instantaneous	0.040–0.001	2.35, 3.3, 30	41
	WC/WN stars	Continuous	0.040–0.001	2.35, 3.3, 30	42
	Supernova rate	Instantaneous	0.040–0.001	2.35, 3.3, 30	43
	Supernova rate	Continuous	0.040–0.001	2.35, 3.3, 30	44
Luminosities	M_{Bol}	Instantaneous	0.040–0.001	2.35, 3.3, 30	45
	M_{Bol}	Continuous	0.040–0.001	2.35, 3.3, 30	46
	M_V	Instantaneous	0.040–0.001	2.35, 3.3, 30	47
	M_V	Continuous	0.040–0.001	2.35, 3.3, 30	48
	M_B	Instantaneous	0.040–0.001	2.35, 3.3, 30	49
	M_B	Continuous	0.040–0.001	2.35, 3.3, 30	50
	M_K	Instantaneous	0.040–0.001	2.35, 3.3, 30	51
	M_K	Continuous	0.040–0.001	2.35, 3.3, 30	52
Colors	Luminosity at 1500 Å	Instantaneous	0.040–0.001	2.35, 3.3, 30	53
	Luminosity at 1500 Å	Continuous	0.040–0.001	2.35, 3.3, 30	54
	(U–B)	Instantaneous	0.040–0.001	2.35, 3.3, 30	55
	(U–B)	Continuous	0.040–0.001	2.35, 3.3, 30	56
	(B–V)	Instantaneous	0.040–0.001	2.35, 3.3, 30	57
	(B–V)	Continuous	0.040–0.001	2.35, 3.3, 30	58
	(V–R)	Instantaneous	0.040–0.001	2.35, 3.3, 30	59
	(V–R)	Continuous	0.040–0.001	2.35, 3.3, 30	60
	(V–I)	Instantaneous	0.040–0.001	2.35, 3.3, 30	61
	(V–I)	Continuous	0.040–0.001	2.35, 3.3, 30	62
	(V–J)	Instantaneous	0.040–0.001	2.35, 3.3, 30	63
	(V–J)	Continuous	0.040–0.001	2.35, 3.3, 30	64
	(V–H)	Instantaneous	0.040–0.001	2.35, 3.3, 30	65

TABLE 1—*Continued*

Topic	Quantity	Star Formation	Metallicity	IMF ³	Figure
	($V-H$)	Continuous	0.040–0.001	2.35, 3.3, 30	66
	($V-K$)	Instantaneous	0.040–0.001	2.35, 3.3, 30	67
	($V-K$)	Continuous	0.040–0.001	2.35, 3.3, 30	68
	($V-L$)	Instantaneous	0.040–0.001	2.35, 3.3, 30	69
	($V-L$)	Continuous	0.040–0.001	2.35, 3.3, 30	70
	Continuum slope at 1550 Å	Instantaneous	0.040–0.001	2.35, 3.3, 30	71
	Continuum slope at 1550 Å	Continuous	0.040–0.001	2.35, 3.3, 30	72
	Continuum slope at 2500 Å	Instantaneous	0.040–0.001	2.35, 3.3, 30	73
	Continuum slope at 2500 Å	Continuous	0.040–0.001	2.35, 3.3, 30	74
Far-UV properties	Lyman discontinuity	Instantaneous	0.040–0.001	2.35, 3.3, 30	75
	Lyman discontinuity	Continuous	0.040–0.001	2.35, 3.3, 30	76
	Photons below 912 Å	Instantaneous	0.040–0.001	2.35, 3.3, 30	77
	Photons below 912 Å	Continuous	0.040–0.001	2.35, 3.3, 30	78
	Photons below 504 Å	Instantaneous	0.040–0.001	2.35, 3.3, 30	79
	Photons below 504 Å	Continuous	0.040–0.001	2.35, 3.3, 30	80
	Photons below 228 Å	Instantaneous	0.040–0.001	2.35, 3.3, 30	81
	Photons below 228 Å	Continuous	0.040–0.001	2.35, 3.3, 30	82
	H α equivalent width	Instantaneous	0.040–0.001	2.35, 3.3, 30	83
	H α equivalent width	Continuous	0.040–0.001	2.35, 3.3, 30	84
	H β equivalent width	Instantaneous	0.040–0.001	2.35, 3.3, 30	85
	H β equivalent width	Continuous	0.040–0.001	2.35, 3.3, 30	86
	Pa β equivalent width	Instantaneous	0.040–0.001	2.35, 3.3, 30	87
	Pa β equivalent width	Continuous	0.040–0.001	2.35, 3.3, 30	88
	Br γ equivalent width	Instantaneous	0.040–0.001	2.35, 3.3, 30	89
	Br γ equivalent width	Continuous	0.040–0.001	2.35, 3.3, 30	90
Other diagnostic lines	Stellar He II λ 4686	Instantaneous	0.040–0.001	2.35, 3.3, 30	91
	Stellar He II λ 4686	Continuous	0.040–0.001	2.35, 3.3, 30	92
	[Fe II] λ 1.26	Instantaneous	0.040–0.001	2.35, 3.3, 30	93
	[Fe II] λ 1.26	Continuous	0.040–0.001	2.35, 3.3, 30	94
	CO index	Instantaneous	0.040–0.001	2.35, 3.3, 30	95
	CO index	Continuous	0.040–0.001	2.35, 3.3, 30	96
	Calcium triplet	Instantaneous	0.040–0.001	2.35, 3.3, 30	97
	Calcium triplet	Continuous	0.040–0.001	2.35, 3.3, 30	98
	CO λ 1.62	Instantaneous	0.040–0.001	2.35, 3.3, 30	99
	CO λ 1.62	Continuous	0.040–0.001	2.35, 3.3, 30	100
	CO λ 2.29	Instantaneous	0.040–0.001	2.35, 3.3, 30	101
	CO λ 2.29	Continuous	0.040–0.001	2.35, 3.3, 30	102
	Si I λ 1.59	Instantaneous	0.040–0.001	2.35, 3.3, 30	103
	Si I λ 1.59	Continuous	0.040–0.001	2.35, 3.3, 30	104
Mass + energy return	Mass-loss rate	Instantaneous	0.040–0.001	2.35, 3.3, 30	105
	Mass-loss rate	Continuous	0.040–0.001	2.35, 3.3, 30	106
	Mass-loss rate by subtype	Instantaneous	0.040–0.001	2.35	107
	Mass-loss rate by subtype	Continuous	0.040–0.001	2.35	108
	Integrated mass loss	Instantaneous	0.040–0.001	2.35, 3.3, 30	109
	Integrated mass loss	Continuous	0.040–0.001	2.35, 3.3, 30	110
	Mechanical luminosity	Instantaneous	0.040–0.001	2.35, 3.3, 30	111
	Mechanical luminosity	Continuous	0.040–0.001	2.35, 3.3, 30	112
	Mech. luminosity by subtype	Instantaneous	0.040–0.001	2.35	113
	Mech. luminosity by subtype	Continuous	0.040–0.001	2.35	114
	Energy input	Instantaneous	0.040–0.001	2.35, 3.3, 30	115
	Energy input	Continuous	0.040–0.001	2.35, 3.3, 30	116
	Ion./bolom. luminosity	Instantaneous	0.040–0.001	2.35, 3.3, 30	117
	Ion./bolom. luminosity	Continuous	0.040–0.001	2.35, 3.3, 30	118
	Mech./bolom. luminosity	Instantaneous	0.040–0.001	2.35, 3.3, 30	119
	Mech./bolom. luminosity	Continuous	0.040–0.001	2.35, 3.3, 30	120

NOTES.—3–2.35: $\alpha = 2.35$, $M_{\text{up}} = 100 M_{\odot}$; 3.3: $\alpha = 3.30$, $M_{\text{up}} = 100 M_{\odot}$; 30: $\alpha = 2.35$, $M_{\text{up}} = 30 M_{\odot}$.

but we decided not to do so. The evolutionary models are optimized for massive stars and become less reliable for older ages. Many properties can still be safely predicted beyond 1 Gyr, whereas others (such as, e.g., near-infrared colors) become increasingly uncertain. We will comment on uncertainties when the individual figures are discussed.

Atmosphere models in LH95 were from Kurucz (1992) for most stars, supplemented by the Schmutz, Leitherer, &

Gruenwald (1992) models for stars with strong winds, and black bodies for the coolest stars. Lejeune et al. (1997) have produced a new, homogeneous grid of atmospheres covering the entire Hertzsprung-Russell diagram (HRD) populated by the evolutionary models, including the coolest stars. This new grid has been implemented in our synthesis code. We used the corrected grid whose fluxes produce colors in agreement with empirical color-temperature rela-

tions. The original atmosphere models do not include metallicities of 0.008 and 0.004. We interpolated between adjacent metallicities to obtain grids whose metallicities match those of the evolutionary models. No interpolation was required for 0.040, 0.020, and 0.001. As in LH95, the Schmutz et al. (1992) extended model atmospheres are used for stars with strong mass loss. The prescription for the switch between extended and plane-parallel atmospheres is the same as in LH95. The extended atmospheres are assigned to all stars with surface temperature greater than 25,000 K and hydrogen content on the surface less than 0.4. We decided not to use extended model atmospheres for stars closer to the main-sequence since the benefit of improved wind treatment would be more than compensated by the limited metallicity range available for such models.

The *nebular continuum* has been added to all spectrophotometric quantities, except to the energy distributions in Figures 7a–7e, 8a–8e, 9a–9e, 10a–10e, 11a–11e, and 12a–12e. We have assumed that all the stellar far-UV photons below 912 Å are converted into free-free and free-bound photons at longer wavelengths (case B). However, the stellar far-UV flux has *not* been removed in the spectral energy distributions, as this would probably not be desirable for the user. To alert the user, the hydrogen and helium emission coefficients of Ferland (1980) do not extend longward of 4.5 μm . Therefore, the nebular continuum at these wavelengths is undefined in our code. In practice, this is hardly relevant since dust emission often dominates at $\lambda > 3 \mu\text{m}$ (Carico et al. 1988) and our models become inapplicable anyway.

All models shown here have been computed with the *isochrone synthesis* method, as opposed to the classical evolutionary synthesis method in LH95. Isochrone synthesis was introduced by Charlot & Bruzual (1991) as a technique to overcome the discrete appearance of the model predictions at late evolutionary stages when the resolution in mass of the evolutionary models becomes inadequate. Instead of binning stars in mass and assigning them to a specific track, continuous isochrones are calculated by interpolating between the tracks in the HRD on a variable mass grid using a subroutine originally provided by G. Meynet. This scheme generally produces smooth output products, the only exception being quantities related to supernovae (see below).

The *time resolution* of the model series is 0.1 Myr. Spectral energy distributions, however, are given only at time steps during which significant changes occur.

The model predictions are discussed in the following sections. A summary of all the figures is in Table 1. Each figure has five panels (a–e) for each of the five metallicities. An exception are Figures 13–36, which show UV line spectra. These spectra are for Z_{\odot} only, as the library stars are currently available only for this metallicity. The models will be extended as soon as nonsolar library stars become available (Robert 1999). The data files which were used for the generation of the plots can be viewed and downloaded (see instructions on the Web site). The files with spectra (Figs. 1–36) contain data at more time steps than plotted. For clarity reasons we included only a subset of all time steps in the plots. Only the figures for solar metallicity models are reproduced in the print edition of the journal (*b* panels of Figs. 1–13 and 37–120, and Figs. 13–36). The full data set for all metallicities is included in the electronic edition of the

journal and can be accessed on our Web site at <http://www.stsci.edu/science/starburst99/>.

3. SPECTRAL ENERGY DISTRIBUTIONS

Spectral energy distributions for all five metallicities, the three IMF parameterizations, and the two star formation laws were calculated. The wavelength coverage and spectral resolution are identical to those of the model atmosphere set Lejeune et al. (1997). The minimum and maximum wavelengths are 91 Å and 160 μm , respectively. The spectral resolution is wavelength dependent. It is typically about 10–20 Å in the UV to optical range. The energy distributions were calculated at intervals of 1, 10, and 100 Myr between 1 and 20 Myr, 20 and 100 Myr, and 100 and 1000 Myr, respectively.

The standard IMF case ($\alpha = 2.35$; $M_{\text{up}} = 100 M_{\odot}$) is in Figure 1. Panels a–e show the energy distributions for the five considered metallicities. Not all time steps are plotted in the figures, but they are included in the ASCII table file which can be downloaded. The wavelength range has been restricted to 100–10,000 Å in the figures, but the full range is covered in the tables.

The most dramatic changes occur in the far-UV below 912 Å, and even more below 228 Å in the He^{++} continuum. O stars dominate during the first few Myr, followed by a brief period at ~ 4 Myr when WR stars contribute with their strong far-UV flux. Eventually the burst population fades away. Metallicity enters both via the continuum and line opacity (compare the 2600 Å region at low and high metallicity) and via stellar evolution. The latter effect can most readily be seen in the strength of the He^{++} continuum. It is strongest at high metallicity when WR stars preferentially form, and it is weakest at low metallicity (see also the discussion in § 8).

The continuous star formation case for the same IMF is in Figures 2a–2e. Most of the prior discussion holds for this

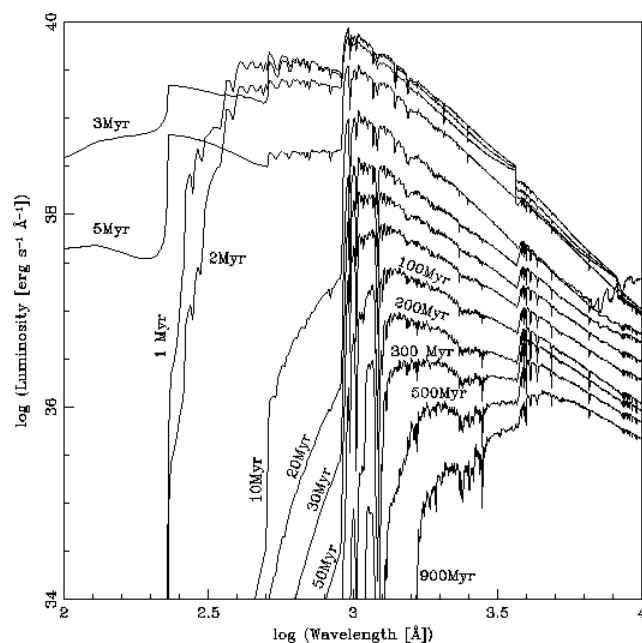


FIG. 1b

FIG. 1.—Spectral energy distributions from 100 Å to 1 μm between 1 Myr and 1 Gyr. Star formation law: instantaneous; IMF: $\alpha = 2.35$, $M_{\text{up}} = 100 M_{\odot}$; nebular continuum included; (a) $Z = 0.040$; (b) $Z = 0.020$; (c) $Z = 0.008$; (d) $Z = 0.004$; (e) $Z = 0.001$.

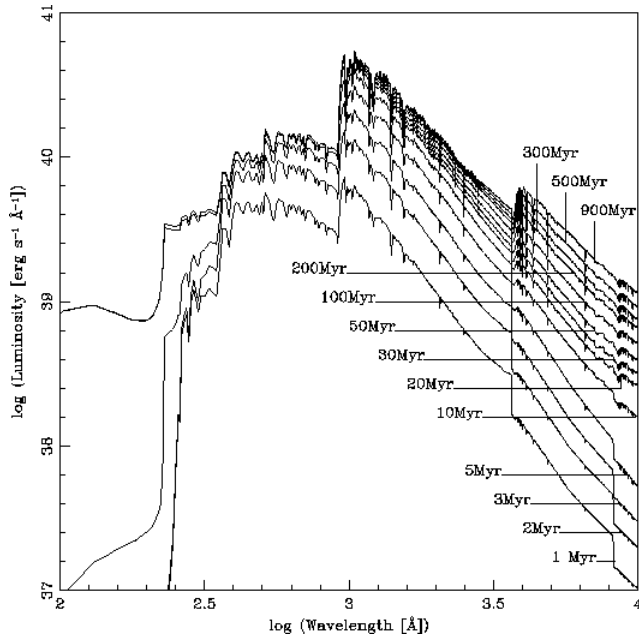


FIG. 2b

FIG. 2.—Spectral energy distributions from 100 Å to 1 μm between 1 Myr and 1 Gyr. Star formation law: continuous; IMF: $\alpha = 2.35$, $M_{\text{up}} = 100 M_{\odot}$; nebular continuum included; (a) $Z = 0.040$; (b) $Z = 0.020$; (c) $Z = 0.008$; (d) $Z = 0.004$; (e) $Z = 0.001$.

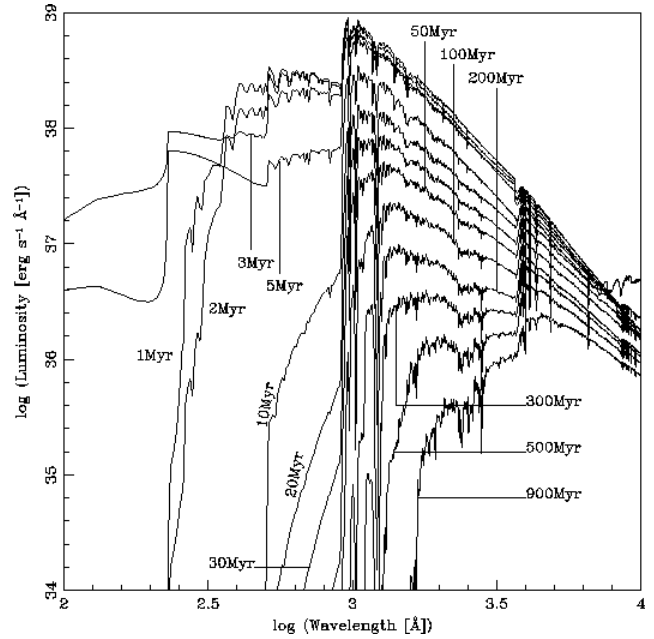


FIG. 3b

FIG. 3.—Spectral energy distributions from 100 Å to 1 μm between 1 Myr and 1 Gyr. Star formation law: instantaneous; IMF: $\alpha = 3.30$, $M_{\text{up}} = 100 M_{\odot}$; nebular continuum included; (a) $Z = 0.040$; (b) $Z = 0.020$; (c) $Z = 0.008$; (d) $Z = 0.004$; (e) $Z = 0.001$.

figure as well. Once the stellar types responsible for the photon contribution to a wavelength interval have reached equilibrium between birth and death, the particular wavelength region becomes time independent.

We move on to different IMFs. The instantaneous and continuous cases, with $\alpha = 3.3$, $M_{\text{up}} = 100 M_{\odot}$ are in Figures 3a–3e and 4a–4e, respectively. The truncated IMF, $\alpha = 2.35$, $M_{\text{up}} = 30 M_{\odot}$ is covered in Figures 5a–5e and 6a–6e. The spectral energy distributions produce a softer radiation field as compared with the standard IMF, in particular if stars with $M_{\text{up}} > 30 M_{\odot}$ are suppressed.

The radiative properties shown later in the paper were obtained from these energy distributions. For instance, colors were derived by convolving the spectra by the filter profiles. Users who wish to compute colors in different filter systems can do so with the spectra in Figures 1–6. Another application would be to use the spectral energy distributions as input to a photoionization code. In this case, Figures 1–6 should *not* be used because the nebular continuum was added to the stellar flux. We computed an additional set of stellar spectra with exactly the same parameters as before, but without including the nebular continuum. This set may also be useful to compute magnitudes and colors for comparison with objects which have no nebular continuum contribution. An example could be a background-subtracted star cluster, where the background subtraction removed the nebular emission as well. There may also be cases where the nebular emission of a galaxy or H II region is more extended than the ionizing cluster, and part of the nebular flux is outside the instrument aperture. Finally, the H II region may not be ionization-bounded. Such cases may be easier to model using energy distributions without nebular continuum and applying an empirical correction, e.g., from the observed H α flux in the aperture. The models without nebular continuum are in Figures

7a–7e ($\alpha = 2.35$, $M_{\text{up}} = 100 M_{\odot}$, instantaneous star formation), Figures 8a–8e ($\alpha = 2.35$, $M_{\text{up}} = 100 M_{\odot}$, continuous star formation), Figures 9a–9e ($\alpha = 3.3$, $M_{\text{up}} = 100 M_{\odot}$, instantaneous star formation), Figures 10a–10e ($\alpha = 3.3$, $M_{\text{up}} = 100 M_{\odot}$, continuous star formation), Figures 11a–11e ($\alpha = 2.35$, $M_{\text{up}} = 30 M_{\odot}$, instantaneous star formation), and Figures 12a–12e ($\alpha = 2.35$, $M_{\text{up}} = 30$

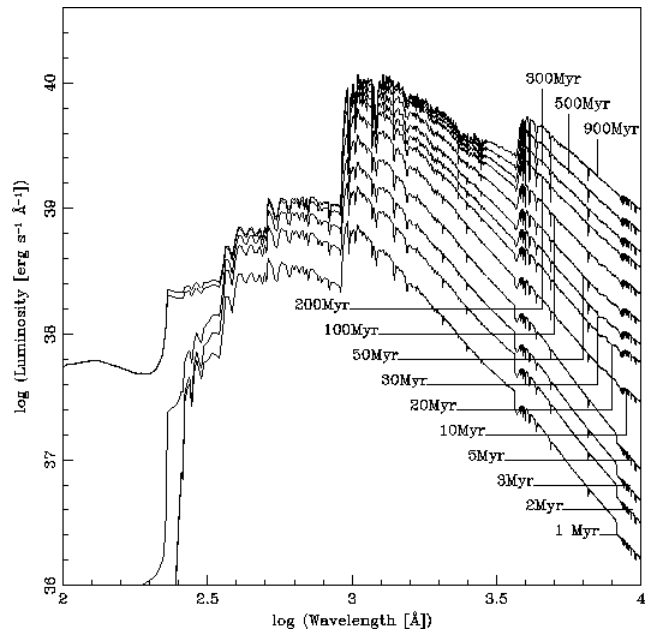


FIG. 4b

FIG. 4.—Spectral energy distributions from 100 Å to 1 μm between 1 Myr and 1 Gyr. Star formation law: continuous; IMF: $\alpha = 3.30$, $M_{\text{up}} = 100 M_{\odot}$; nebular continuum included; (a) $Z = 0.040$; (b) $Z = 0.020$; (c) $Z = 0.008$; (d) $Z = 0.004$; (e) $Z = 0.001$.

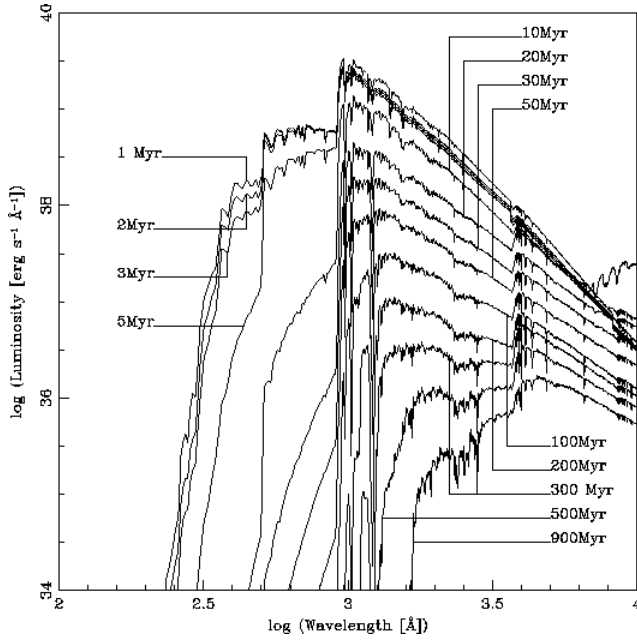


FIG. 5b

FIG. 5.—Spectral energy distributions from 100 Å to 1 μm between 1 Myr and 1 Gyr. Star formation law: instantaneous; IMF: $\alpha = 2.35$, $M_{\text{up}} = 30 M_{\odot}$; nebular continuum included; (a) $Z = 0.040$; (b) $Z = 0.020$; (c) $Z = 0.008$; (d) $Z = 0.004$; (e) $Z = 0.001$.

M_{\odot} , continuous star formation). The spectra in Figures 7–12 and the curves in Figures 45, 46, 75, and 76 are the only models in this paper that do not include the nebular continuum.

4. ULTRAVIOLET LINE PROFILES

Two spectral regions with useful diagnostic lines were computed at higher resolution. The wavelength range from

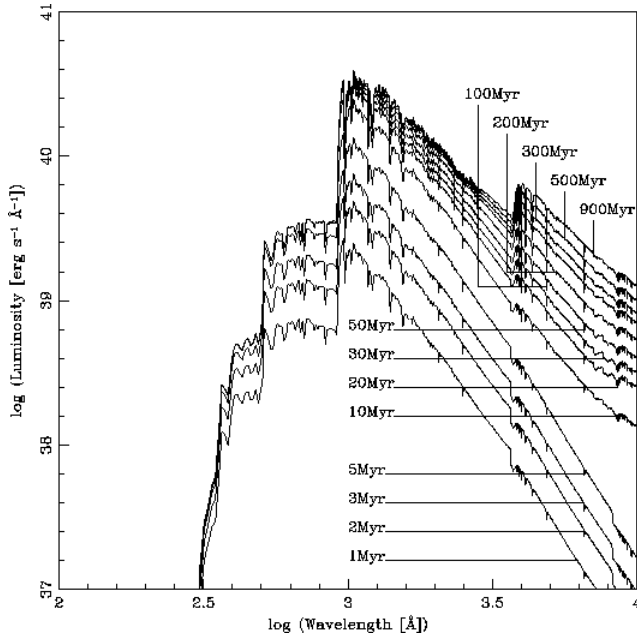


FIG. 6b

FIG. 6.—Spectral energy distributions from 100 Å to 1 μm between 1 Myr and 1 Gyr. Star formation law: continuous; IMF: $\alpha = 2.35$, $M_{\text{up}} = 30 M_{\odot}$; nebular continuum included; (a) $Z = 0.040$; (b) $Z = 0.020$; (c) $Z = 0.008$; (d) $Z = 0.004$; (e) $Z = 0.001$.

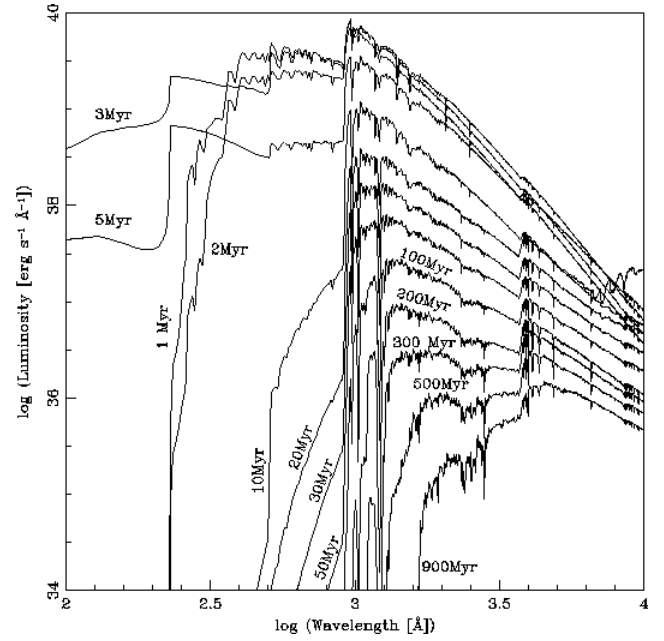


FIG. 7b

FIG. 7.—Spectral energy distributions from 100 Å to 1 μm between 1 Myr and 1 Gyr. Star formation law: instantaneous; IMF: $\alpha = 2.35$, $M_{\text{up}} = 100 M_{\odot}$; nebular continuum not included; (a) $Z = 0.040$; (b) $Z = 0.020$; (c) $Z = 0.008$; (d) $Z = 0.004$; (e) $Z = 0.001$.

1200 to 1850 Å has the strong resonance lines of C iv $\lambda 1550$, Si iv $\lambda 1400$, and N v $\lambda 1240$. At shorter wavelengths, O vi $\lambda 1035$ and Ly β are of interest. The spectra described in this section were computed with a normalized library of stellar UV spectra and absolute fluxes derived from the energy distributions shown in the previous section. We did not use

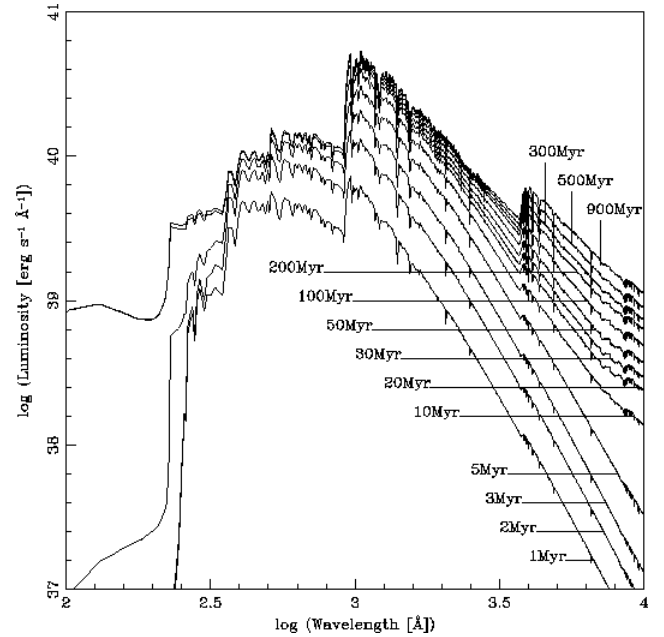


FIG. 8b

FIG. 8.—Spectral energy distributions from 100 Å to 1 μm between 1 Myr and 1 Gyr. Star formation law: continuous; IMF: $\alpha = 2.35$, $M_{\text{up}} = 100 M_{\odot}$; nebular continuum not included; (a) $Z = 0.040$; (b) $Z = 0.020$; (c) $Z = 0.008$; (d) $Z = 0.004$; (e) $Z = 0.001$.

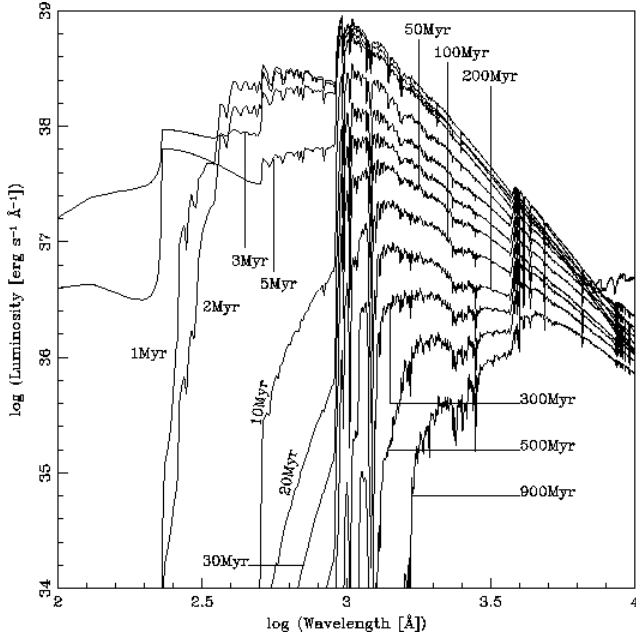


FIG. 9b

FIG. 9.—Spectral energy distributions from 100 Å to 1 μm between 1 Myr and 1 Gyr. Star formation law: instantaneous; IMF: $\alpha = 3.30$, $M_{\text{up}} = 100 M_{\odot}$; nebular continuum not included; (a) $Z = 0.040$; (b) $Z = 0.020$; (c) $Z = 0.008$; (d) $Z = 0.004$; (e) $Z = 0.001$.

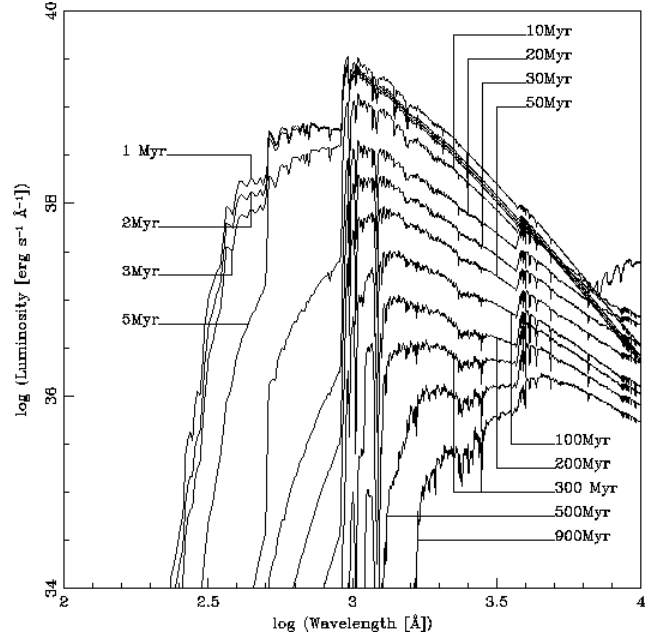


FIG. 11b

FIG. 11.—Spectral energy distributions from 100 Å to 1 μm between 1 Myr and 1 Gyr. Star formation law: instantaneous; IMF: $\alpha = 2.35$, $M_{\text{up}} = 30 M_{\odot}$; nebular continuum not included; (a) $Z = 0.040$; (b) $Z = 0.020$; (c) $Z = 0.008$; (d) $Z = 0.004$; (e) $Z = 0.001$.

the energy distributions directly since they are not featureless. Rather we derived a featureless continuum by fitting a spline through line-free sections of the model atmospheres.

4.1. The 1200 Å to 1850 Å Region

The 1200–1850 Å region is readily accessible to many satellites, like *IUE* or *HST*. We synthesized spectra from an

IUE high-dispersion library of O- and WR-spectra and a low-dispersion for B stars. The spectral library and the method are discussed in Robert, Leitherer, & Heckman (1993) and Leitherer et al. (1995). The resolution is 0.75 Å, adequate for typical spectral data of extragalactic objects. This resolution is only reached during phases dominated by

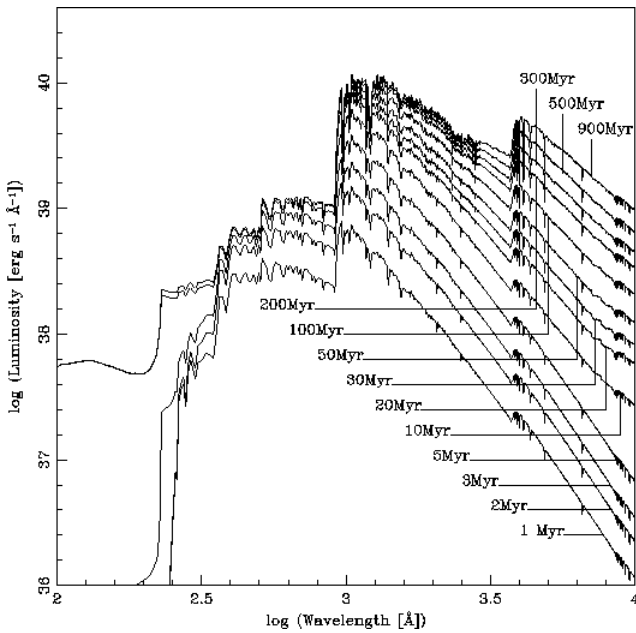


FIG. 10b

FIG. 10.—Spectral energy distributions from 100 Å to 1 μm between 1 Myr and 1 Gyr. Star formation law: continuous; IMF: $\alpha = 3.30$, $M_{\text{up}} = 100 M_{\odot}$; nebular continuum not included; (a) $Z = 0.040$; (b) $Z = 0.020$; (c) $Z = 0.008$; (d) $Z = 0.004$; (e) $Z = 0.001$.

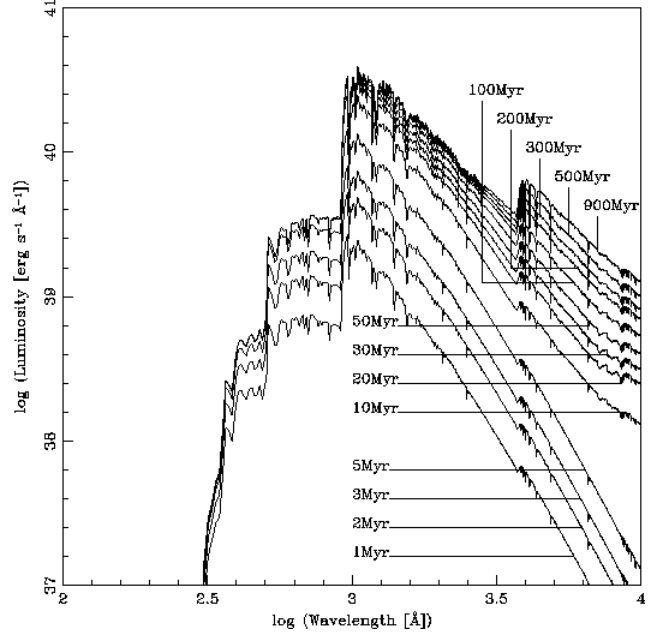


FIG. 12b

FIG. 12.—Spectral energy distributions from 100 Å to 1 μm between 1 Myr and 1 Gyr. Star formation law: continuous; IMF: $\alpha = 2.35$, $M_{\text{up}} = 30 M_{\odot}$; nebular continuum not included; (a) $Z = 0.040$; (b) $Z = 0.020$; (c) $Z = 0.008$; (d) $Z = 0.004$; (e) $Z = 0.001$.

O- and WR stars, as is the case for young ($t < 7$ Myr) bursts and for the continuous case at any time. Otherwise the effective spectral resolution approaches the resolution of *IUE* low-dispersion spectra (6 Å). The upgrade of the B-star library from low to high dispersion has been completed and will be implemented in the future (de Mello, Leitherer, & Heckman 1999, in preparation; Robert, Leitherer, & Heckman 1999, in preparation).

Only solar metallicity models are shown since the library stars have solar or somewhat subsolar metallicity. A spectral library of massive stars in the Magellanic Clouds is being developed and will be available in the future (Robert 1999; Robert, Leitherer, & Heckman 1999, in preparation).

Figure 13 shows rectified spectra between 1 and 20 Myr for an instantaneous burst. A standard IMF was used. The evolution of the strongest *stellar-wind* features of C iv $\lambda 1550$, Si iv $\lambda 1400$, N v $\lambda 1240$, N iv $\lambda 1720$, and He ii $\lambda 1640$ can be readily seen. These features disappear or become *photospheric* lines after about 7 Myr when the transition from an O-star to a B-star dominated population occurs. A purely photospheric line is, e.g., S v $\lambda 1502$. The library stars have strong *interstellar* lines as well. One of the strongest lines is C ii $\lambda 1335$.

The continuous case for the same IMF is shown in Figure 14. The same basic effects are there as well, but the time dependence is much weaker, and a quasi-equilibrium state is reached after about 5 Myr. Figures 15 and 16 show spectra with the same parameters as in Figures 13 and 14, but in absolute luminosity units.

As we did for the spectral energy distributions in the previous section, we recomputed the UV spectra for the two other IMFs, a steeper IMF with $\alpha = 3.3$ and a truncated IMF with $M_{\text{up}} = 30 M_{\odot}$. These spectra are in Figures 17–24. The general trend is a weakening of all stellar-wind lines, most notably C iv $\lambda 1550$ and Si iv $\lambda 1400$, as these lines are due to massive O stars. These lines are very sensitive IMF tracers. Their detection immediately indicates an

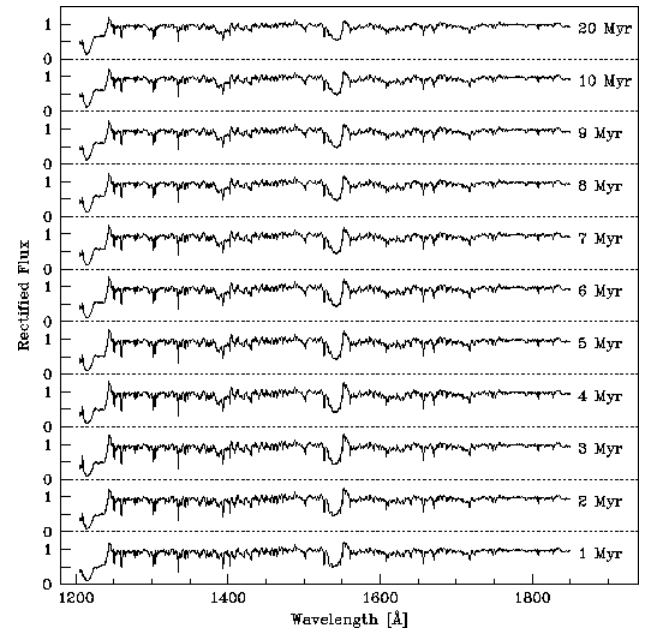


FIG. 14.—Spectral region from 1200 to 1850 Å between 1 and 20 Myr. The spectra are rectified. Star formation law: continuous; IMF: $\alpha = 2.35$, $M_{\text{up}} = 100 M_{\odot}$; $Z = 0.020$.

O-star population and therefore star formation over the past ~ 10 Myr.

4.2. The 1015 Å to 1060 Å Region

The wavelength region shortward of Ly α in local starburst galaxies is accessible to, e.g., the FUSE mission (Sahnou et al. 1996) and can be observed in star-forming galaxies at high redshift from the ground. One of the strongest stellar-wind lines is O vi $\lambda 1035$ (Walborn & Bohlin 1996). Synthetic spectra for the region between 1015 and 1060 Å were presented by González Delgado et al. (1997)

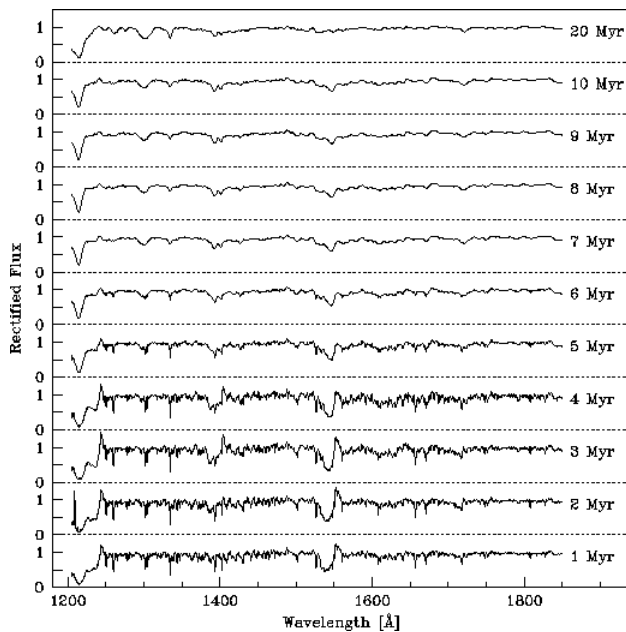


FIG. 13.—Spectral region from 1200 to 1850 Å between 1 and 20 Myr. The spectra are rectified. Star formation law: instantaneous; IMF: $\alpha = 2.35$, $M_{\text{up}} = 100 M_{\odot}$; $Z = 0.020$.

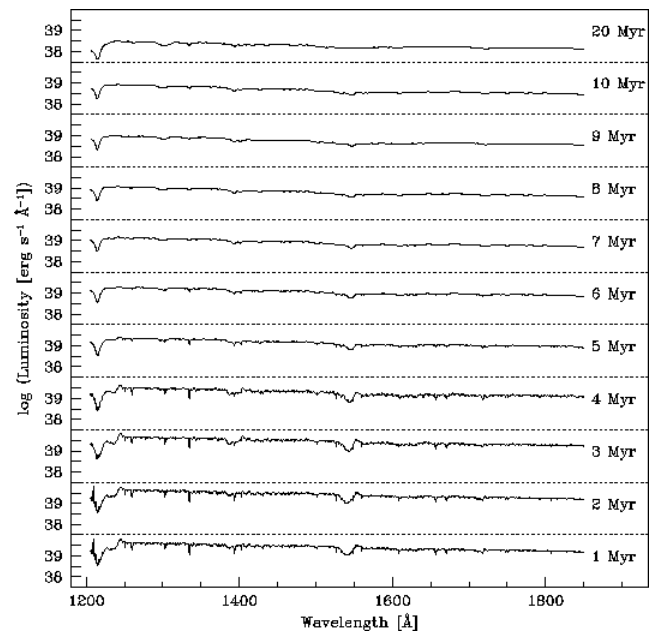


FIG. 15.—Spectral region from 1200 to 1850 Å between 1 and 20 Myr. The spectra are in luminosity units. Star formation law: instantaneous; IMF: $\alpha = 2.35$, $M_{\text{up}} = 100 M_{\odot}$; $Z = 0.020$.

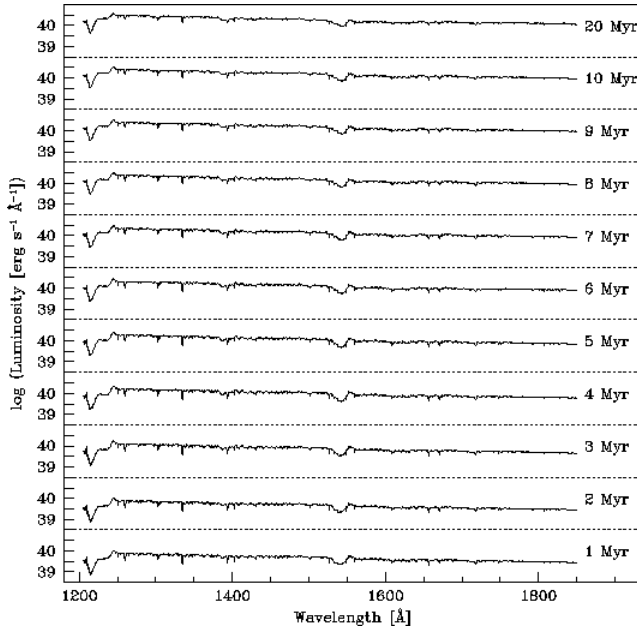


FIG. 16.—Spectral region from 1200 to 1850 Å between 1 and 20 Myr. The spectra are in luminosity units. Star formation law: continuous; IMF: $\alpha = 2.35$, $M_{\text{up}} = 100 M_{\odot}$; $Z = 0.020$.

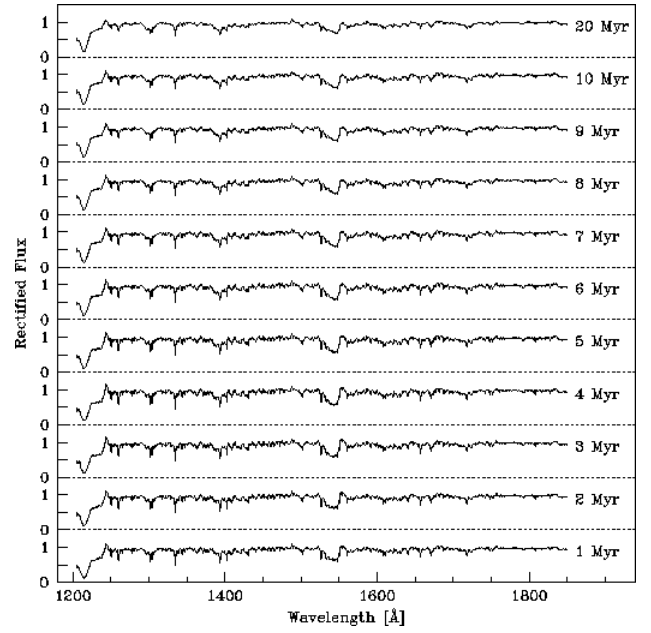


FIG. 18.—Spectral region from 1200 to 1850 Å between 1 and 20 Myr. The spectra are rectified. Star formation law: continuous; IMF: $\alpha = 3.30$, $M_{\text{up}} = 100 M_{\odot}$; $Z = 0.020$.

and were regenerated for the Starburst99 package. They are based on an empirical Copernicus library of O and B stars and have a resolution of 0.2 Å. A few library stars were observed with HUT at a spectral resolution of about 3 Å. Only solar metallicity models are considered, as we have no library stars with nonsolar metallicity. Available time steps are 1–20 Myr at $\Delta t = 1$ Myr and 20–100 Myr at $\Delta t = 10$ Myr. Not every time step is plotted in the figures.

We discuss the most notable features using the standard IMF, instantaneous burst, rectified model (Fig. 25). The strongest lines are O VI $\lambda 1035$, Ly β , C II $\lambda 1036$, and the

Lyman and Werner bands of H₂, like the one at 1050 Å. In the first few Myr of the starburst, O VI $\lambda 1035$ has a strong P Cygni profile, indicating winds from massive O stars. O VI $\lambda 1035$ becomes weaker with age and gradually blends with Ly β at 1026 Å. Ly β is mostly stellar, with some interstellar contribution. The line increases in strength with increasing B-star fraction. C II $\lambda 1036$ follows Ly β in its temporal behavior. It is a strong B-star line with some interstellar contribution and can be used to estimate the starburst age (González Delgado et al. 1997). The continuous case with the same IMF parameters behaves accordingly (Fig. 26).

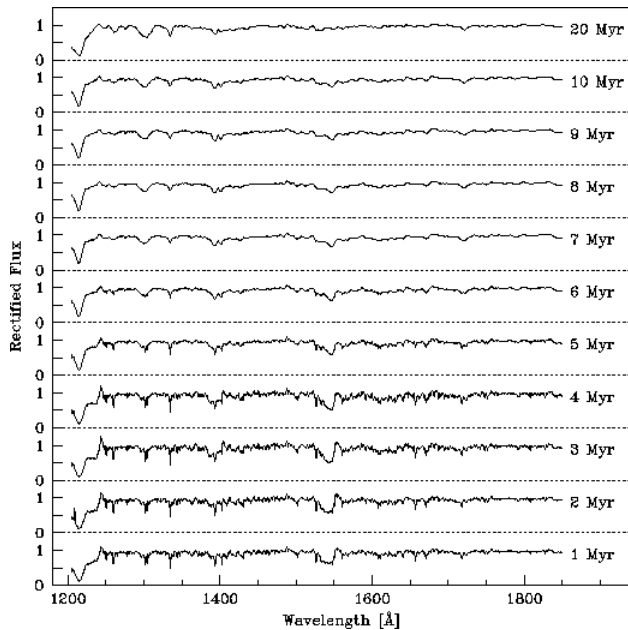


FIG. 17.—Spectral region from 1200 to 1850 Å between 1 and 20 Myr. The spectra are rectified. Star formation law: instantaneous; IMF: $\alpha = 3.30$, $M_{\text{up}} = 100 M_{\odot}$; $Z = 0.020$.

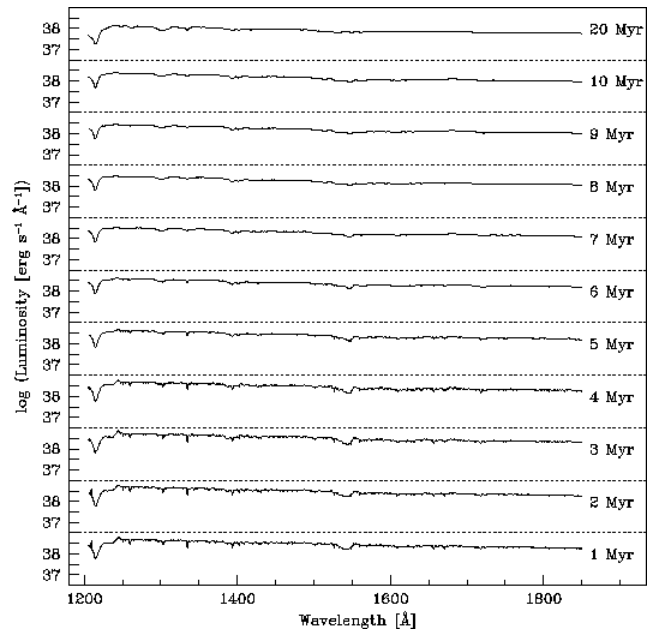


FIG. 19.—Spectral region from 1200 to 1850 Å between 1 and 20 Myr. The spectra are in luminosity units. Star formation law: instantaneous; IMF: $\alpha = 3.30$, $M_{\text{up}} = 100 M_{\odot}$; $Z = 0.020$.

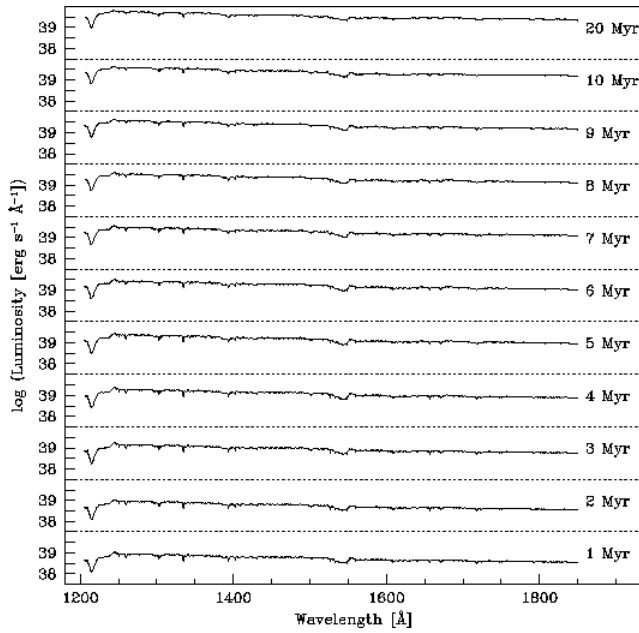


FIG. 20.—Spectral region from 1200 to 1850 Å between 1 and 20 Myr. The spectra are in luminosity units. Star formation law: continuous; IMF: $\alpha = 3.30$, $M_{\text{up}} = 100 M_{\odot}$; $Z = 0.020$.

The counterparts of Figures 25 and 26 in luminosity units are in Figures 27 and 28.

The remaining figures for O VI $\lambda 1035$ are organized the same way as the figures for the 1200–1850 Å region. They are intended to highlight IMF variations (Figs. 29–36). An IMF biased against massive O stars suppresses O VI $\lambda 1035$ and strengthens C II $\lambda 1036$. Even at the earliest ages the absorption trough around 1025 Å is mostly due to Ly β and not O VI $\lambda 1035$.

5. MASSIVE-STAR INVENTORY

In this section we give number predictions for massive

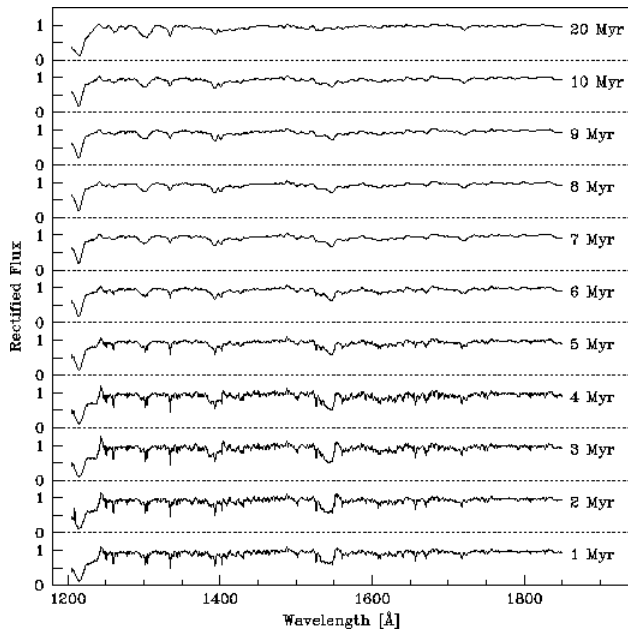


FIG. 21.—Spectral region from 1200 to 1850 Å between 1 and 20 Myr. The spectra are rectified. Star formation law: instantaneous; IMF: $\alpha = 2.35$, $M_{\text{up}} = 30 M_{\odot}$; $Z = 0.020$.

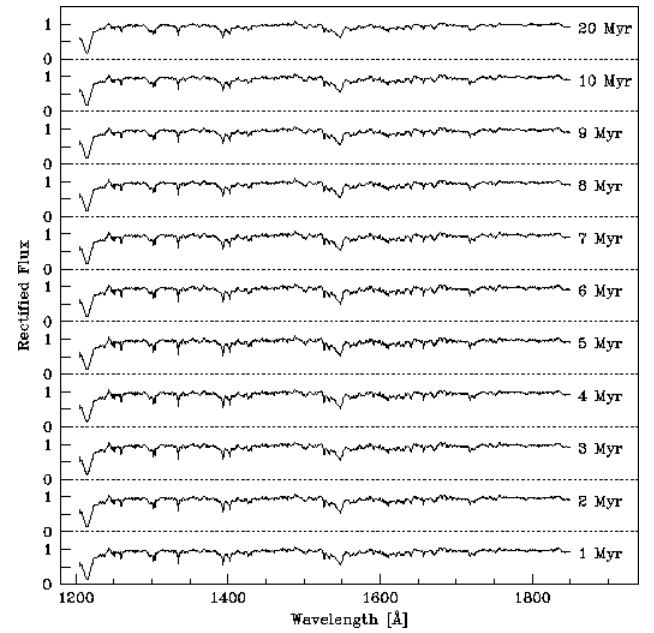


FIG. 22.—Spectral region from 1200 to 1850 Å between 1 and 20 Myr. The spectra are rectified. Star formation law: continuous; IMF: $\alpha = 2.35$, $M_{\text{up}} = 30 M_{\odot}$; $Z = 0.020$.

stellar types that can be easily “counted” even in distant galaxies: O stars, WR stars, and supernovae (SNe).

O-star numbers are in Figures 37a–37e and 38a–38e for the instantaneous and continuous case, respectively. Panels *a*, *b*, *c*, *d*, and *e* are for metallicities 0.040, 0.020, 0.008, 0.004, and 0.001, respectively. All remaining figures in this paper have the same structure. The O-star numbers include stars with spectral types O3 to O9.5 of all luminosity classes. The adopted spectral type versus effective temperature (T_{eff}) and luminosity (L) relation is from Schmidt-Kaler (1982). The chosen star formation histories produce up to about 10^3 to

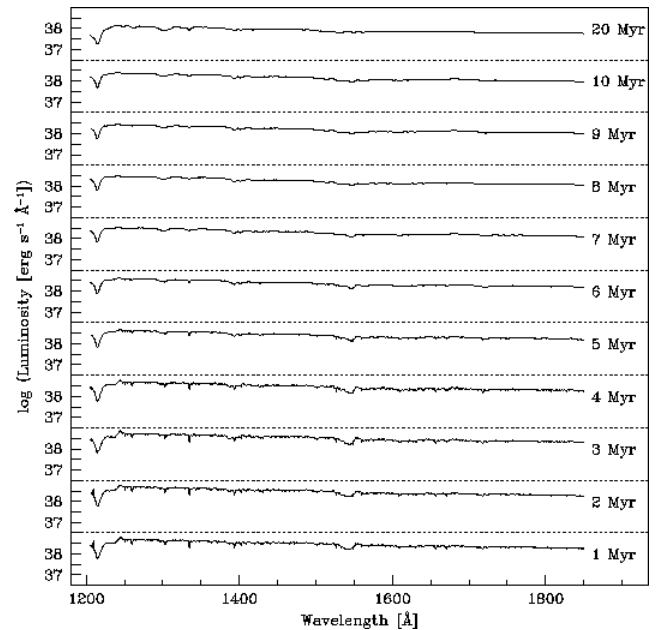


FIG. 23.—Spectral region from 1200 to 1850 Å between 1 and 20 Myr. The spectra are in luminosity units. Star formation law: instantaneous; IMF: $\alpha = 2.35$, $M_{\text{up}} = 30 M_{\odot}$; $Z = 0.020$.

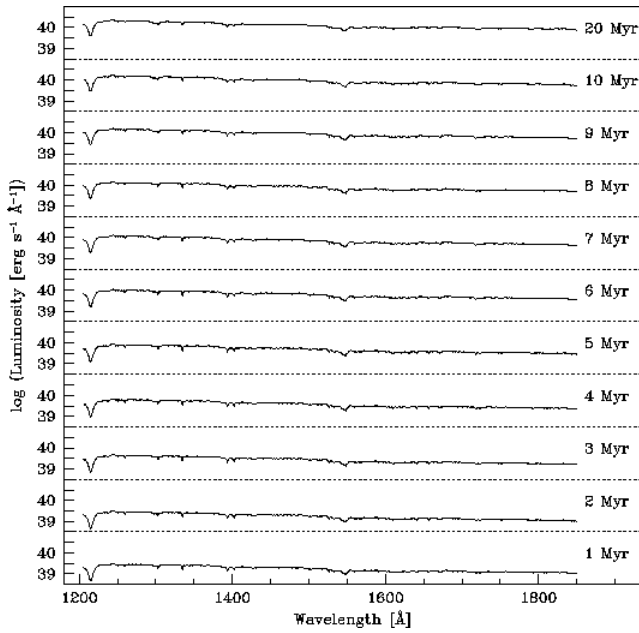


FIG. 24.—Spectral region from 1200 to 1850 Å between 1 and 20 Myr. The spectra are in luminosity units. Star formation law: continuous; IMF: $\alpha = 2.35$, $M_{\text{up}} = 30 M_{\odot}$; $Z = 0.020$.

10^4 O stars at any time, depending on the age of the population. A flatter IMF increases the O-star number.

WR stars are the evolved descendants of massive O stars. We define them as stars with $\log T_{\text{eff}} > 4.4$ and surface hydrogen abundance less than 0.4 by mass. The mass limits for the formation of WR stars are taken from Maeder & Meynet (1994). WR stars have very extended atmospheres producing strong emission lines that can be detected in distant starburst populations (Conti 1991). The quantity of interest for comparison with models is the WR/O ratio, which is plotted in Figures 39a–39e and 40a–40e for the

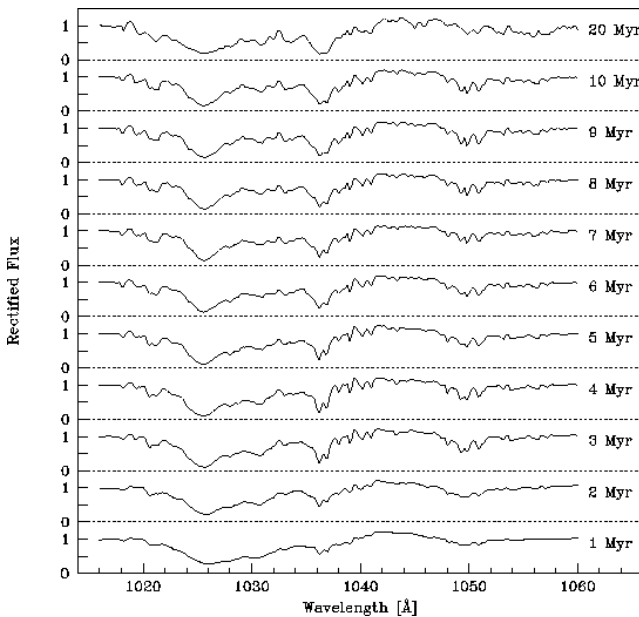


FIG. 25.—Spectral region around O VI $\lambda 1035$ between 1 and 100 Myr. The spectra are rectified. Star formation law: instantaneous; IMF: $\alpha = 2.35$, $M_{\text{up}} = 100 M_{\odot}$; $Z = 0.020$.

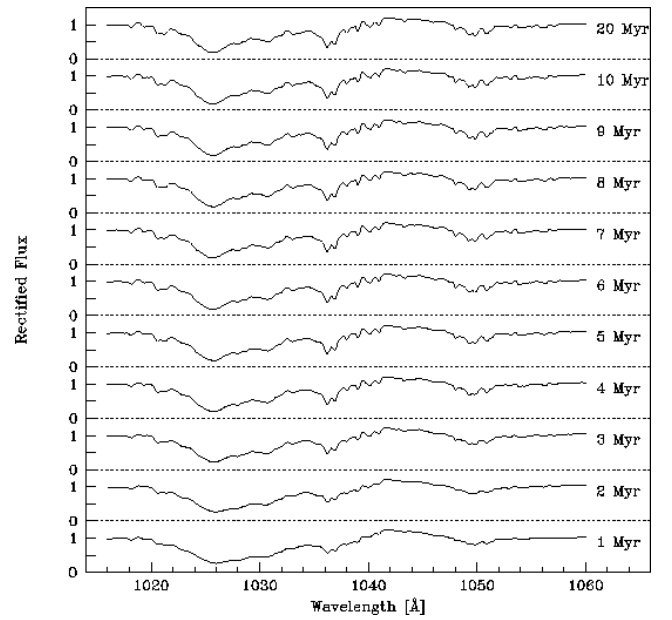


FIG. 26.—Spectral region around O VI $\lambda 1035$ between 1 and 100 Myr. The spectra are rectified. Star formation law: continuous; IMF: $\alpha = 2.35$, $M_{\text{up}} = 100 M_{\odot}$; $Z = 0.020$.

instantaneous and continuous case, respectively. This ratio is very metallicity dependent: metal-rich starbursts are predicted to have more WR stars at any time and to have longer phases when WR stars are present. This behavior is generally in agreement with observations (Meynet 1995). The panels with subsolar metallicity have no graph for the IMF with $M_{\text{up}} = 30 M_{\odot}$. This results from the absence of WR stars at low metallicity. The detailed shape of the graphs in Figures 39a–39e and 40a–40e is very model dependent, and future revisions of the evolutionary models may change the WR/O ratio. Dedicated evolutionary synthesis models with particular attention to the WR phase

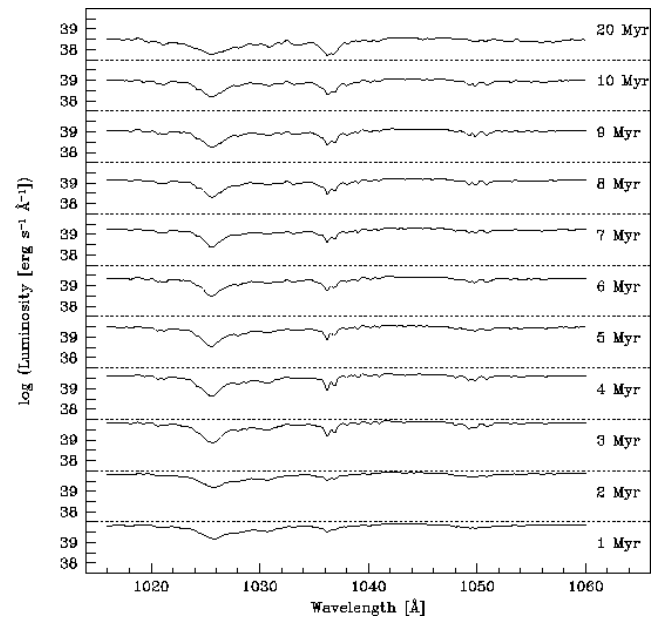


FIG. 27.—Spectral region around O VI $\lambda 1035$ between 1 and 100 Myr. The spectra are in luminosity units. Star formation law: instantaneous; IMF: $\alpha = 2.35$, $M_{\text{up}} = 100 M_{\odot}$; $Z = 0.020$.

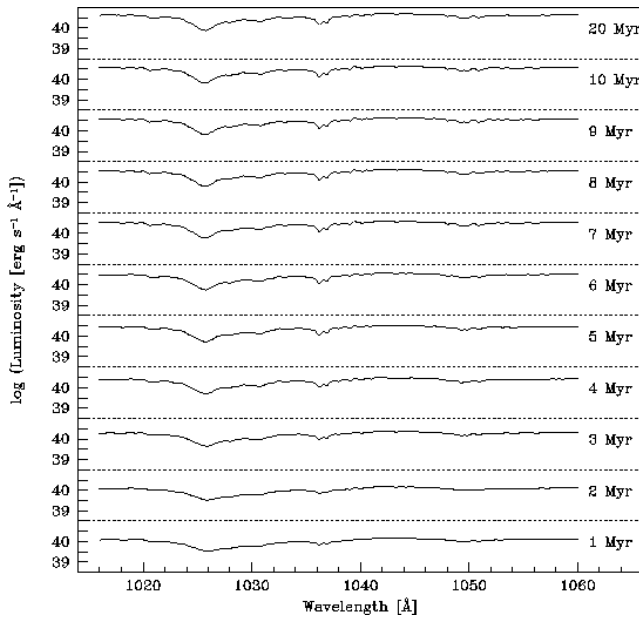


FIG. 28.—Spectral region around O VI $\lambda 1035$ between 1 and 100 Myr. The spectra are in luminosity units. Star formation law: continuous; IMF: $\alpha = 2.35$, $M_{\text{up}} = 100 M_{\odot}$; $Z = 0.020$.

were published by Meynet (1995) and Schaerer & Vacca (1998). The binary channel to form WR stars in stellar populations was investigated by Cerviño & Mas-Hesse (1997), Vanbeveren et al. (1997), Schaerer & Vacca (1998), and Dionne (1999).

WR stars come in two main subclasses: nitrogen-rich WN stars and carbon-rich WC stars. We adopt the classification schemes of Conti, Leep, & Perry (1983) for WN stars and of Smith & Hummer (1988) and Smith & Maeder (1991) for WC stars. The WC/WN ratio measures the relative lifetimes spent in the two phases (Figs. 41a–41e and 42a–42e). However, the calculations are affected by uncer-

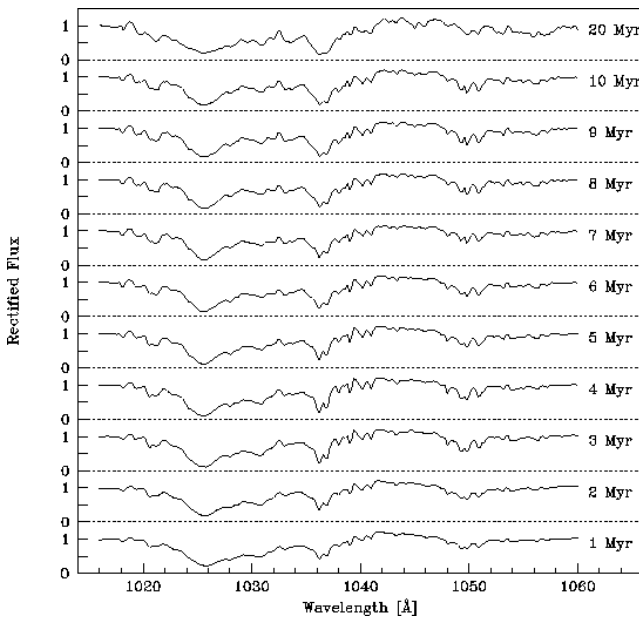


FIG. 29.—Spectral region around O VI $\lambda 1035$ between 1 and 100 Myr. The spectra are rectified. Star formation law: instantaneous; IMF: $\alpha = 3.30$, $M_{\text{up}} = 100 M_{\odot}$; $Z = 0.020$.

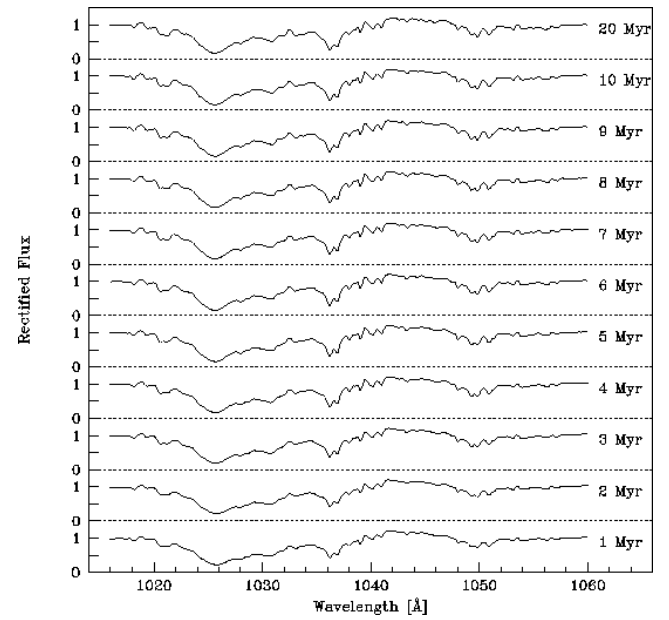


FIG. 30.—Spectral region around O VI $\lambda 1035$ between 1 and 100 Myr. The spectra are rectified. Star formation law: continuous; IMF: $\alpha = 3.30$, $M_{\text{up}} = 100 M_{\odot}$; $Z = 0.020$.

tainties in the interpolation of the relatively sparse tracks, as discussed in Schaerer & Vacca (1998). In this respect, the present models are identical to those of Schaerer & Vacca, who predict fewer WC stars than Meynet (1995) despite the use of the same tracks. Most of the comments on the WR/O ratio apply to these figures as well. The WC/WN ratio varies very little with the IMF exponent: the $\alpha = 2.35$ and 3.3 cases are almost indiscernible in the figures. This indicates that both stellar types have progenitors of very similar

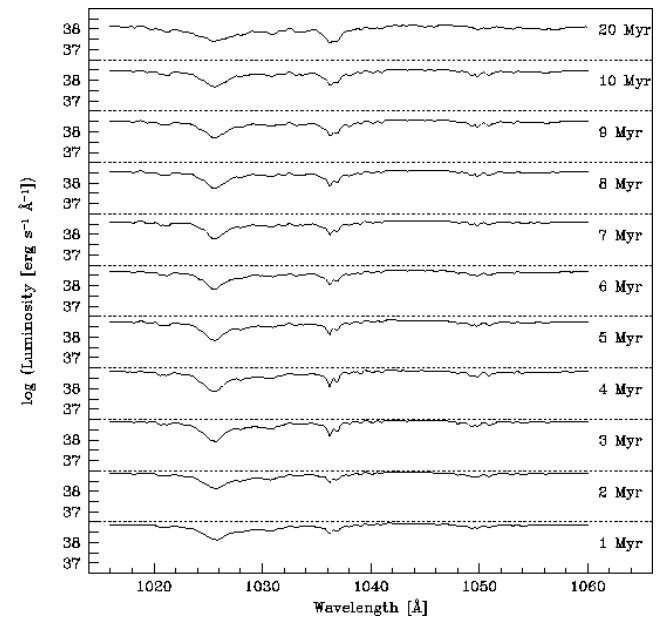


FIG. 31.—Spectral region around O VI $\lambda 1035$ between 1 and 100 Myr. The spectra are in luminosity units. Star formation law: instantaneous; IMF: $\alpha = 3.30$, $M_{\text{up}} = 100 M_{\odot}$; $Z = 0.020$.

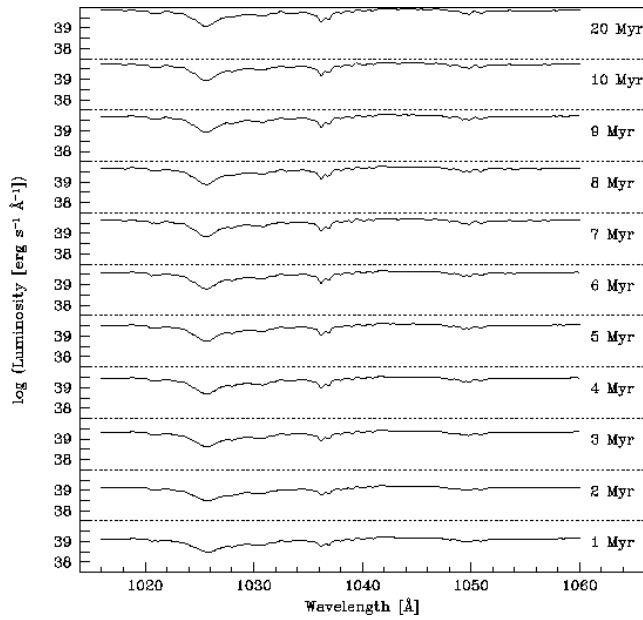


FIG. 32.—Spectral region around O VI $\lambda 1035$ between 1 and 100 Myr. The spectra are in luminosity units. Star formation law: continuous; IMF: $\alpha = 3.30$, $M_{\text{up}} = 100 M_{\odot}$; $Z = 0.020$.

mass. As a result, applying different weights to different mass intervals does not affect the ratio. The same argument applies to several other quantities discussed further below, like, e.g., the CO index (Fig. 95).

All massive stars with initial masses above $8 M_{\odot}$ are assumed to explode as SNe. This leaves open the question if a critical mass exists above which stars directly form a black hole rather than producing a core-collapse SN (Maeder 1992). If so, the predictions of Figures 43a–43e and 44a–44e

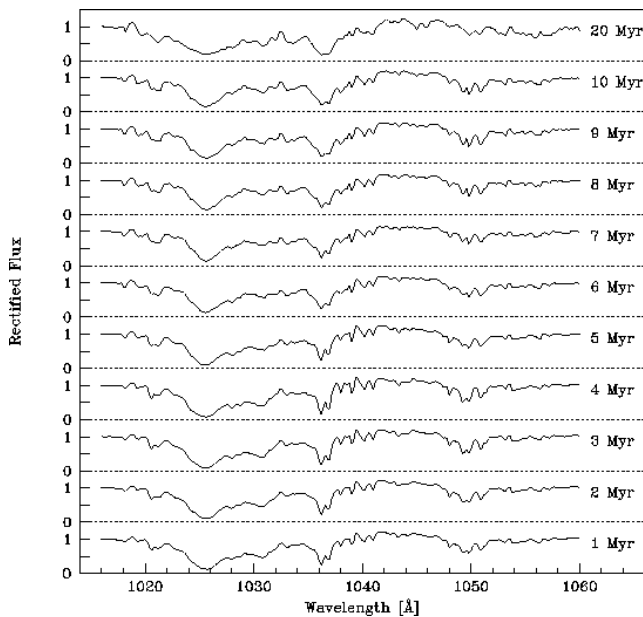


FIG. 33.—Spectral region around O VI $\lambda 1035$ between 1 and 100 Myr. The spectra are rectified. Star formation law: instantaneous; IMF: $\alpha = 2.35$, $M_{\text{up}} = 30 M_{\odot}$; $Z = 0.020$.

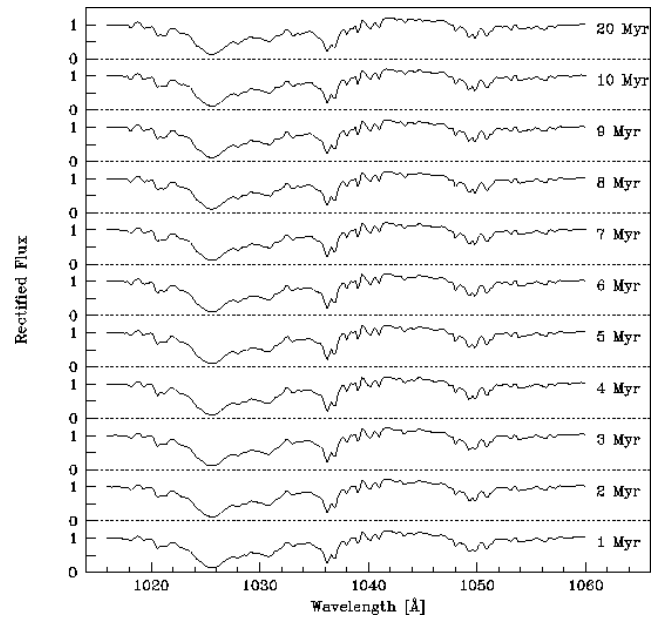


FIG. 34.—Spectral region around O VI $\lambda 1035$ between 1 and 100 Myr. The spectra are rectified. Star formation law: continuous; IMF: $\alpha = 2.35$, $M_{\text{up}} = 30 M_{\odot}$; $Z = 0.020$.

would hardly be changed because the SN rate is strongly weighted toward the lowest progenitor masses.

The user should be aware of a computational issue that can be seen in Figures 43a–43e and 44a–44e. The graphs show discontinuities at the factor-of-2 level where there should be none (e.g., around 10 Myr in Fig. 43). A simple argument suggests that the SN rate should be a smooth and almost constant function of time. The rate scales with the product of the IMF and the mass-age relation. For a Salpe-

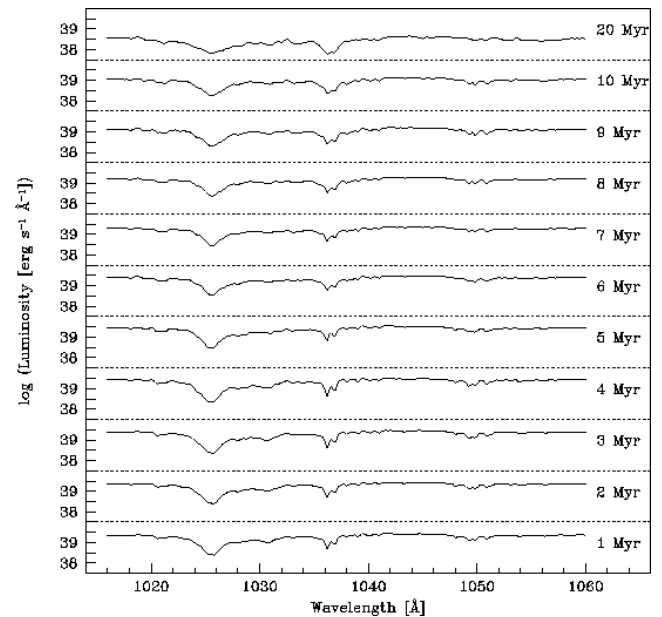


FIG. 35.—Spectral region around O VI $\lambda 1035$ between 1 and 100 Myr. The spectra are in luminosity units. Star formation law: instantaneous; IMF: $\alpha = 2.35$, $M_{\text{up}} = 30 M_{\odot}$; $Z = 0.020$.

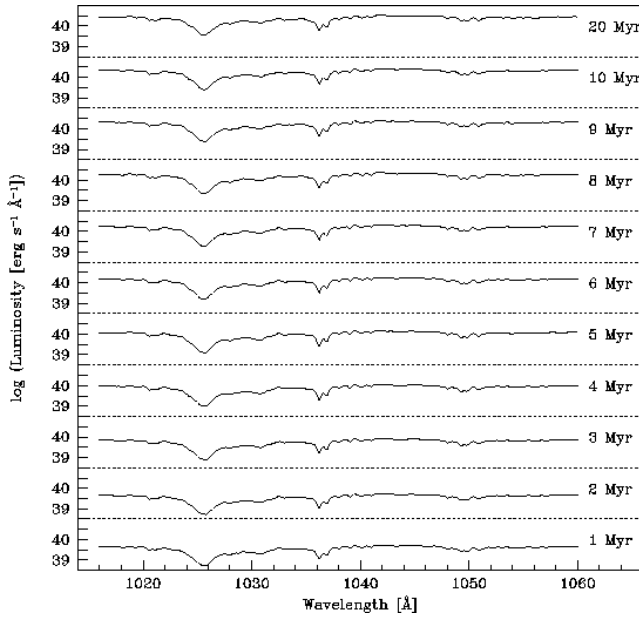


FIG. 36.—Spectral region around O VI $\lambda 1035$ between 1 and 100 Myr. The spectra are in luminosity units. Star formation law: continuous; IMF: $\alpha = 2.35$, $M_{\text{up}} = 30 M_{\odot}$; $Z = 0.020$.

ter IMF and a mass-age relation $t(m) \propto m^{-\gamma}$ with $\gamma \approx 1.2$ (Schaerer et al. 1993b) the SN rate of an instantaneous burst becomes essentially time independent (Shull & Saken 1995). In other words, there are more and more SN events for lower masses since there are more progenitors available, but

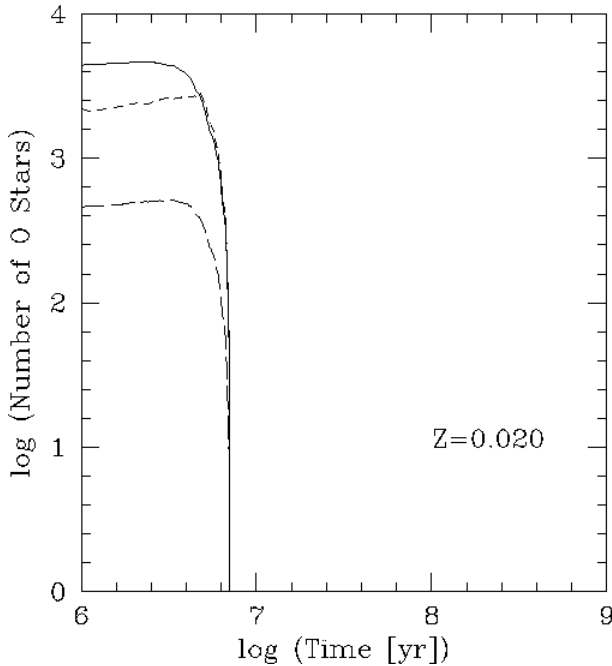


FIG. 37b

FIG. 37.—Number of O stars vs. time. Star formation law: instantaneous; solid line, $\alpha = 2.35$, $M_{\text{up}} = 100 M_{\odot}$; long-dashed line, $\alpha = 3.30$, $M_{\text{up}} = 100 M_{\odot}$; short-dashed line, $\alpha = 2.35$, $M_{\text{up}} = 30 M_{\odot}$; (a) $Z = 0.040$; (b) $Z = 0.020$; (c) $Z = 0.008$; (d) $Z = 0.004$; (e) $Z = 0.001$.

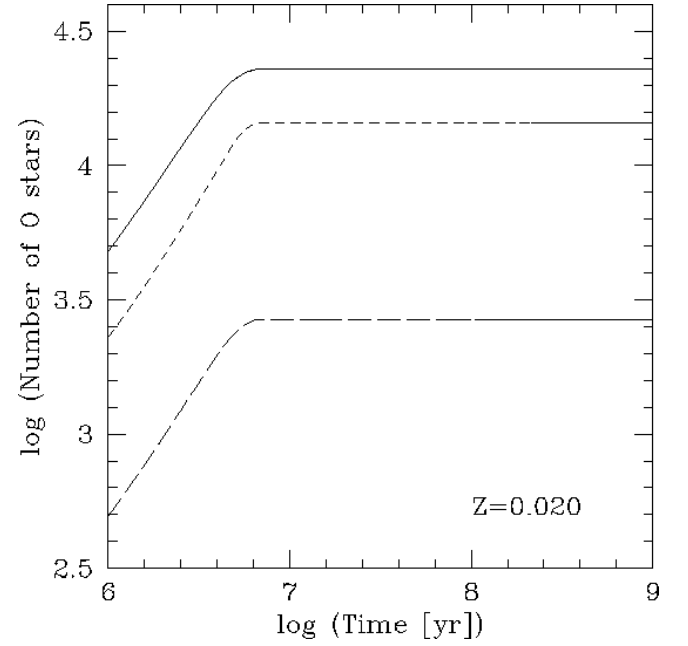


FIG. 38b

FIG. 38.—Number of O stars vs. time. Star formation law: continuous; solid line, $\alpha = 2.35$, $M_{\text{up}} = 100 M_{\odot}$; long-dashed line, $\alpha = 3.30$, $M_{\text{up}} = 100 M_{\odot}$; short-dashed line, $\alpha = 2.35$, $M_{\text{up}} = 30 M_{\odot}$; (a) $Z = 0.040$; (b) $Z = 0.020$; (c) $Z = 0.008$; (d) $Z = 0.004$; (e) $Z = 0.001$.

at the same time it takes longer for a star to turn into a SN. Obviously, the discontinuities in Figure 43 are not physical. They result from a peculiarity of the isochrone synthesis interpolation technique. The code attempts to optimize the

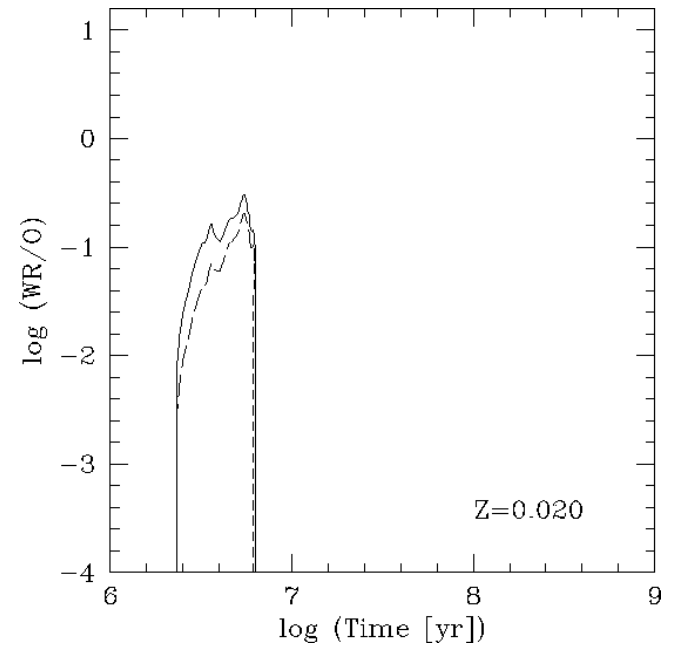


FIG. 39b

FIG. 39.—Ratio of WR over O stars vs. time. Star formation law: instantaneous; solid line, $\alpha = 2.35$, $M_{\text{up}} = 100 M_{\odot}$; long-dashed line, $\alpha = 3.30$, $M_{\text{up}} = 100 M_{\odot}$; short-dashed line, $\alpha = 2.35$, $M_{\text{up}} = 30 M_{\odot}$; (a) $Z = 0.040$; (b) $Z = 0.020$; (c) $Z = 0.008$; (d) $Z = 0.004$; (e) $Z = 0.001$.

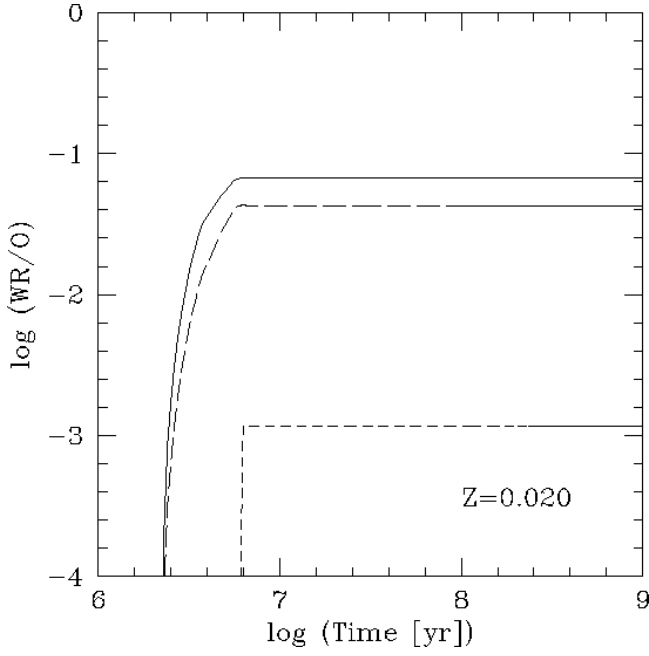


FIG. 40b

FIG. 40.—Ratio of WR over O stars vs. time. Star formation law: continuous; solid line, $\alpha = 2.35$, $M_{\text{up}} = 100 M_{\odot}$; long-dashed line, $\alpha = 3.30$, $M_{\text{up}} = 100 M_{\odot}$; short-dashed line, $\alpha = 2.35$, $M_{\text{up}} = 30 M_{\odot}$; (a) $Z = 0.040$; (b) $Z = 0.020$; (c) $Z = 0.008$; (d) $Z = 0.004$; (e) $Z = 0.001$.

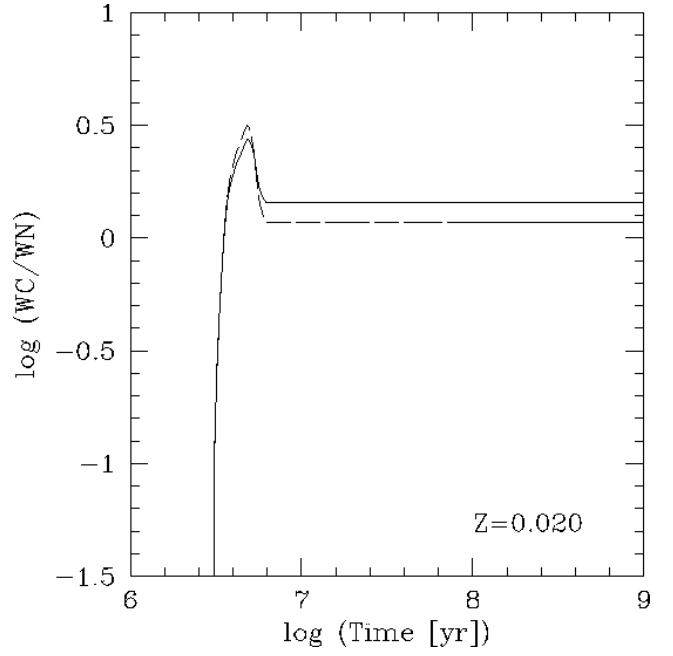


FIG. 42b

FIG. 42.—Ratio of WC over WN stars vs. time. Star formation law: continuous; solid line, $\alpha = 2.35$, $M_{\text{up}} = 100 M_{\odot}$; long-dashed line, $\alpha = 3.30$, $M_{\text{up}} = 100 M_{\odot}$; short-dashed line, $\alpha = 2.35$, $M_{\text{up}} = 30 M_{\odot}$; (a) $Z = 0.040$; (b) $Z = 0.020$; (c) $Z = 0.008$; (d) $Z = 0.004$; (e) $Z = 0.001$.

mass interval size for the interpolation. This works extremely well, except when only stars in an infinitesimal mass interval are relevant, as is the case for the SN rate. The same applies to all quantities that are directly dependent on

the SN rate, like the energy release from SNe. We decided not to artificially smooth the curves since this would be a subjective process and we did not want to treat SN-related quantities different from the other predictions. We remind

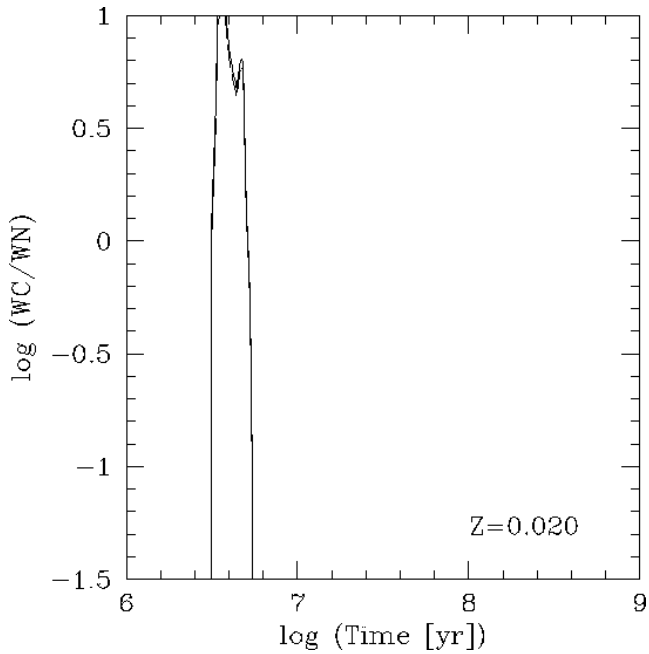


FIG. 41b

FIG. 41.—Ratio of WC over WN stars vs. time. Star formation law: instantaneous; solid line, $\alpha = 2.35$, $M_{\text{up}} = 100 M_{\odot}$; long-dashed line, $\alpha = 3.30$, $M_{\text{up}} = 100 M_{\odot}$; short-dashed line, $\alpha = 2.35$, $M_{\text{up}} = 30 M_{\odot}$; (a) $Z = 0.040$; (b) $Z = 0.020$; (c) $Z = 0.008$; (d) $Z = 0.004$; (e) $Z = 0.001$.

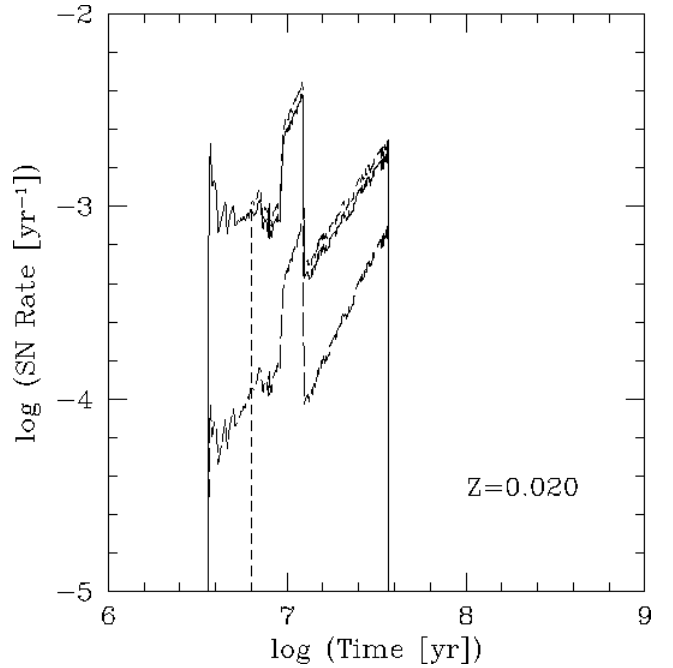


FIG. 43b

FIG. 43.—Supernova rate vs. time. Star formation law: instantaneous; solid line, $\alpha = 2.35$, $M_{\text{up}} = 100 M_{\odot}$; long-dashed line, $\alpha = 3.30$, $M_{\text{up}} = 100 M_{\odot}$; short-dashed line, $\alpha = 2.35$, $M_{\text{up}} = 30 M_{\odot}$; (a) $Z = 0.040$; (b) $Z = 0.020$; (c) $Z = 0.008$; (d) $Z = 0.004$; (e) $Z = 0.001$.

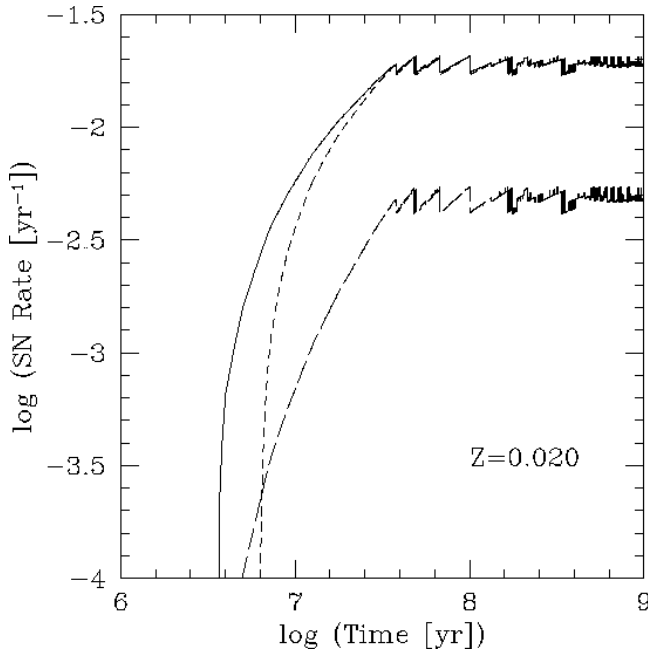


FIG. 44b

FIG. 44.—Supernova rate vs. time. Star formation law: continuous; solid line, $\alpha = 2.35$, $M_{\text{up}} = 100 M_{\odot}$; long-dashed line, $\alpha = 3.30$, $M_{\text{up}} = 100 M_{\odot}$; short-dashed line, $\alpha = 2.35$, $M_{\text{up}} = 30 M_{\odot}$; (a) $Z = 0.040$; (b) $Z = 0.020$; (c) $Z = 0.008$; (d) $Z = 0.004$; (e) $Z = 0.001$.

the user to apply common sense when interpreting the figures. The correct supernova rate between 5 and 35 Myr for an instantaneous burst in Figure 43 is about 10^{-3} yr^{-1} (LH95).

6. LUMINOSITIES

We give the total and monochromatic luminosities at selected wavelengths. We have chosen the V , B , and K passbands, as well as a UV wavelength at 1500 \AA , since these are the most interesting cases for comparison with observations. Luminosities for other bands can be obtained from the spectral energy distributions in Figures 1–6.

The bolometric luminosity (M_{bol}) is defined such that the Sun has $M_{\text{bol}} = 4.75$. The results in Figures 45a–45e and 46a–46e were obtained by integrating the spectral energy distributions without the nebular continuum. The total luminosity of the combined stellar and nebular continuum is smaller than the pure stellar continuum since only a fraction of the absorbed stellar ionizing flux is reemitted in the nebular continuum. The curves are smooth without strong discontinuities and reflect the behavior of the most massive stars which provide most of the radiative energy output.

The absolute magnitudes M_V , M_B , and M_K are in Figures 47a–47e (instantaneous) through 52a–52e (continuous). The absolute magnitude M_V was calculated from the bolometric luminosity and the bolometric correction, which is 0.00 for a solar metallicity star with $T_{\text{eff}} = 7000 \text{ K}$ and $\log g = 1.0$. The Sun has a bolometric correction of -0.19 in this system. The absolute magnitudes M_B and M_K follow from M_V and the $(B-V)$ and $(V-K)$ colors. All three luminosities have conspicuous variations around 10 Myr when red supergiants (RSG) appear. The effect is strongest in the K band, which is closest to the energy peak of RSGs. The RSG feature is very metallicity dependent. The RSG contri-

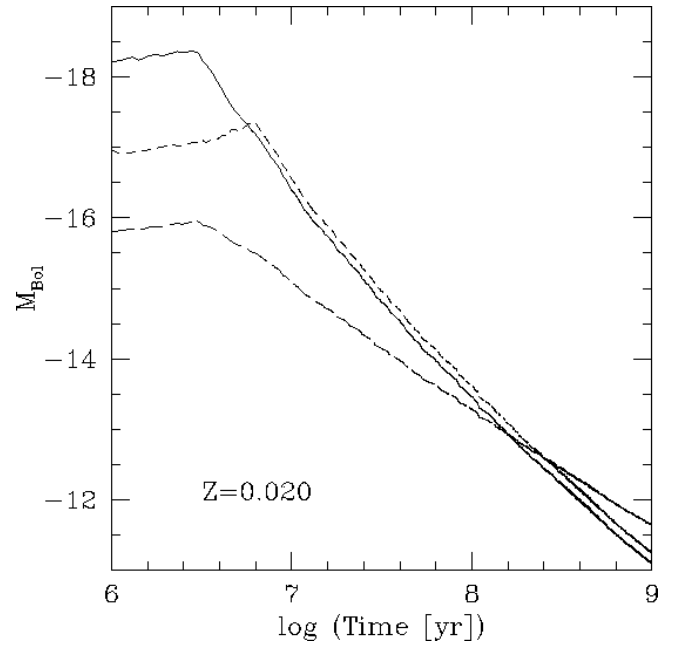


FIG. 45b

FIG. 45.—Absolute bolometric magnitude vs. time. Star formation law: instantaneous; solid line, $\alpha = 2.35$, $M_{\text{up}} = 100 M_{\odot}$; long-dashed line, $\alpha = 3.30$, $M_{\text{up}} = 100 M_{\odot}$; short-dashed line, $\alpha = 2.35$, $M_{\text{up}} = 30 M_{\odot}$; (a) $Z = 0.040$; (b) $Z = 0.020$; (c) $Z = 0.008$; (d) $Z = 0.004$; (e) $Z = 0.001$.

bution in Figures 51a–51e is strongest at $Z = 0.040$ and weakest at $Z = 0.001$. This apparent metallicity dependence results from the failure of the evolutionary models to predict correct RSG properties at $Z \leq 0.008$. This effect was pointed out before by Mayya (1997) and Origlia et al. (1998). Low-metallicity RSG models have too high surface

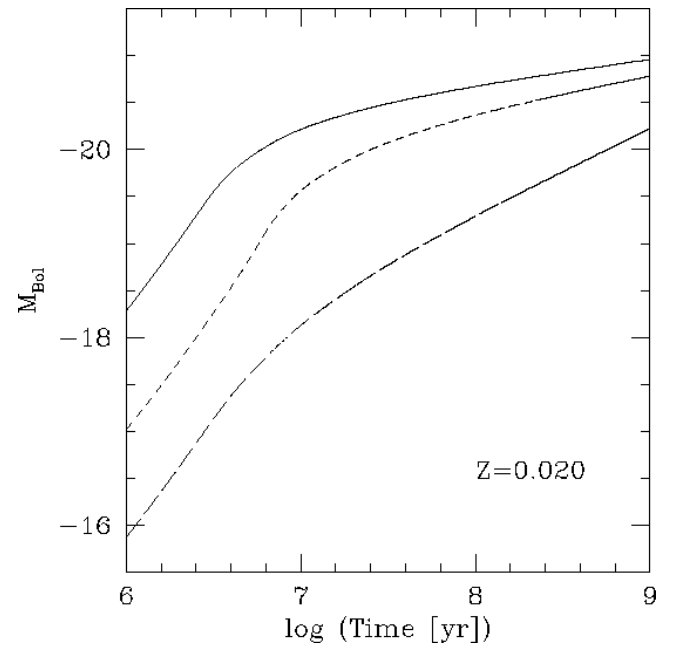


FIG. 46b

FIG. 46.—Absolute bolometric magnitude vs. time. Star formation law: continuous; solid line, $\alpha = 2.35$, $M_{\text{up}} = 100 M_{\odot}$; long-dashed line, $\alpha = 3.30$, $M_{\text{up}} = 100 M_{\odot}$; short-dashed line, $\alpha = 2.35$, $M_{\text{up}} = 30 M_{\odot}$; (a) $Z = 0.040$; (b) $Z = 0.020$; (c) $Z = 0.008$; (d) $Z = 0.004$; (e) $Z = 0.001$.

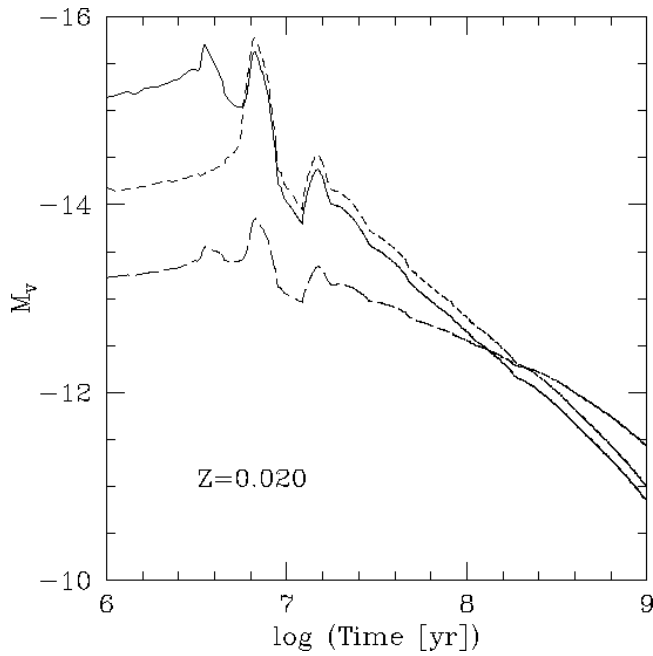


FIG. 47b

FIG. 47.—Absolute V magnitude vs. time. Star formation law: instantaneous; solid line, $\alpha = 2.35$, $M_{\text{up}} = 100 M_{\odot}$; long-dashed line, $\alpha = 3.30$, $M_{\text{up}} = 100 M_{\odot}$; short-dashed line, $\alpha = 2.35$, $M_{\text{up}} = 30 M_{\odot}$; (a) $Z = 0.040$; (b) $Z = 0.020$; (c) $Z = 0.008$; (d) $Z = 0.004$; (e) $Z = 0.001$.

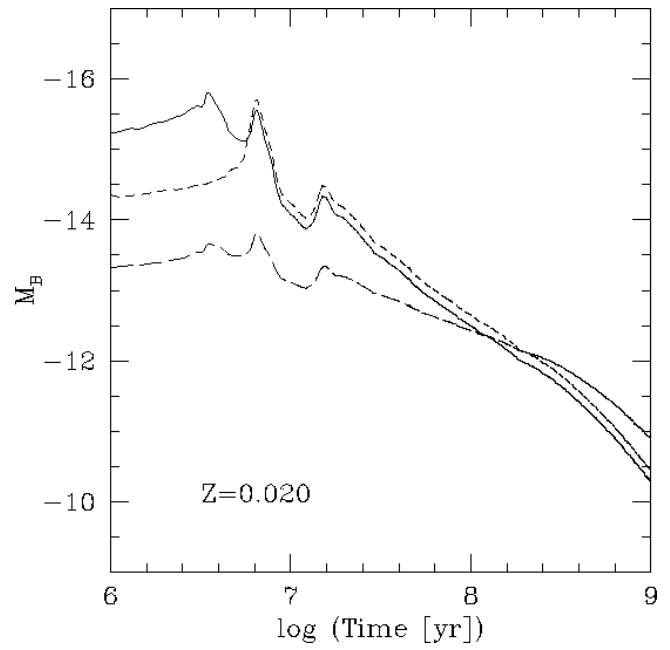


FIG. 49b

FIG. 49.—Absolute B magnitude vs. time. Star formation law: instantaneous; solid line, $\alpha = 2.35$, $M_{\text{up}} = 100 M_{\odot}$; long-dashed line, $\alpha = 3.30$, $M_{\text{up}} = 100 M_{\odot}$; short-dashed line, $\alpha = 2.35$, $M_{\text{up}} = 30 M_{\odot}$; (a) $Z = 0.040$; (b) $Z = 0.020$; (c) $Z = 0.008$; (d) $Z = 0.004$; (e) $Z = 0.001$.

temperatures and too short RSG lifetimes. Uncertainties in the mixing processes at low metallicity are a possible explanation (Langer & Maeder 1995). Currently there are no self-consistent stellar evolution models available that correctly predict the variations of blue-to-red supergiants with

metallicity. Therefore, our (and most other) synthesis models are incorrect during phases when RSGs are important. An empirically adjusted set of synthesis models was prepared by Origlia et al. (1998) but *these adjustments were not made for the model set in this paper.*

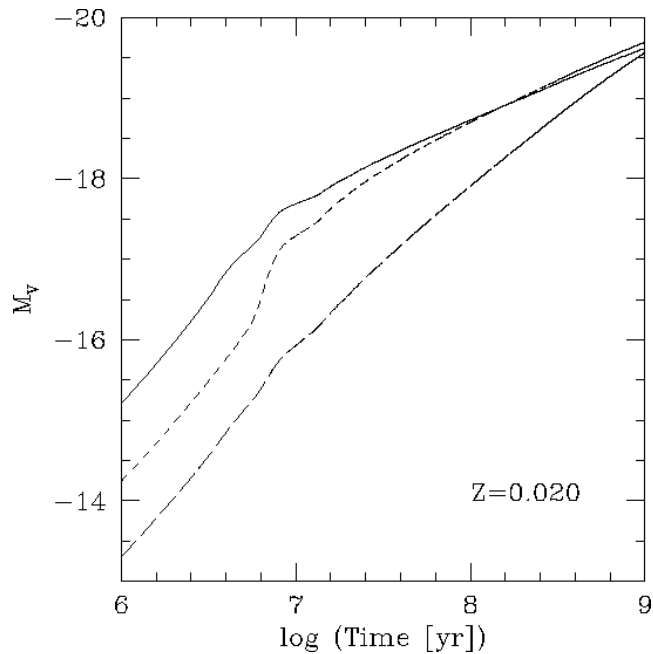


FIG. 48b

FIG. 48.—Absolute V magnitude vs. time. Star formation law: continuous; solid line, $\alpha = 2.35$, $M_{\text{up}} = 100 M_{\odot}$; long-dashed line, $\alpha = 3.30$, $M_{\text{up}} = 100 M_{\odot}$; short-dashed line, $\alpha = 2.35$, $M_{\text{up}} = 30 M_{\odot}$; (a) $Z = 0.040$; (b) $Z = 0.020$; (c) $Z = 0.008$; (d) $Z = 0.004$; (e) $Z = 0.001$.

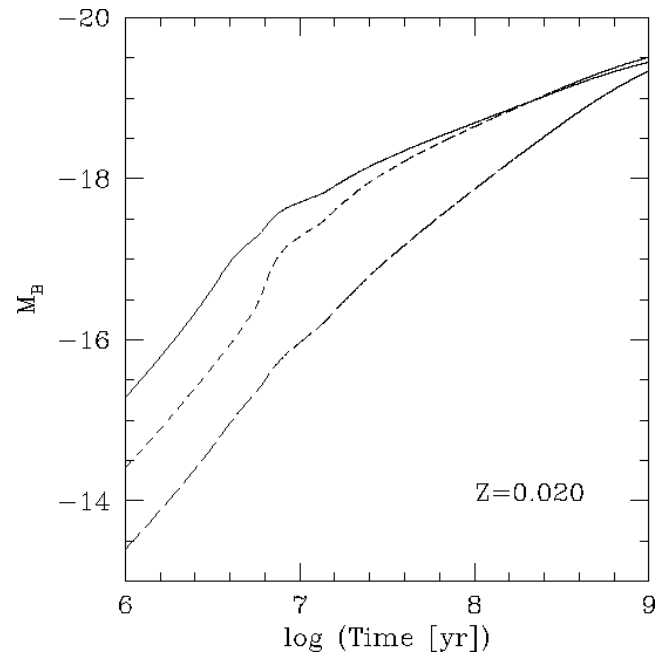


FIG. 50b

FIG. 50.—Absolute B magnitude vs. time. Star formation law: continuous; solid line, $\alpha = 2.35$, $M_{\text{up}} = 100 M_{\odot}$; long-dashed line, $\alpha = 3.30$, $M_{\text{up}} = 100 M_{\odot}$; short-dashed line, $\alpha = 2.35$, $M_{\text{up}} = 30 M_{\odot}$; (a) $Z = 0.040$; (b) $Z = 0.020$; (c) $Z = 0.008$; (d) $Z = 0.004$; (e) $Z = 0.001$.

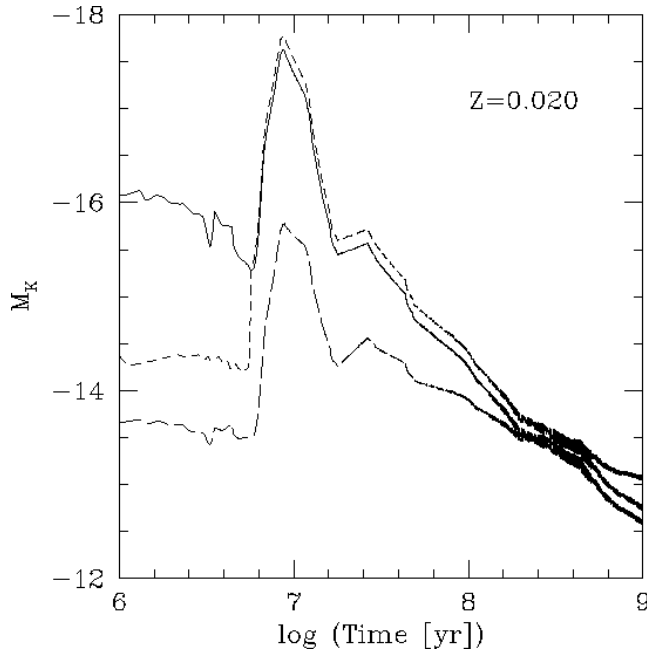


FIG. 51b

FIG. 51.—Absolute K magnitude vs. time. Star formation law: instantaneous; solid line, $\alpha = 2.35$, $M_{\text{up}} = 100 M_{\odot}$; long-dashed line, $\alpha = 3.30$, $M_{\text{up}} = 100 M_{\odot}$; short-dashed line, $\alpha = 2.35$, $M_{\text{up}} = 30 M_{\odot}$; (a) $Z = 0.040$; (b) $Z = 0.020$; (c) $Z = 0.008$; (d) $Z = 0.004$; (e) $Z = 0.001$.

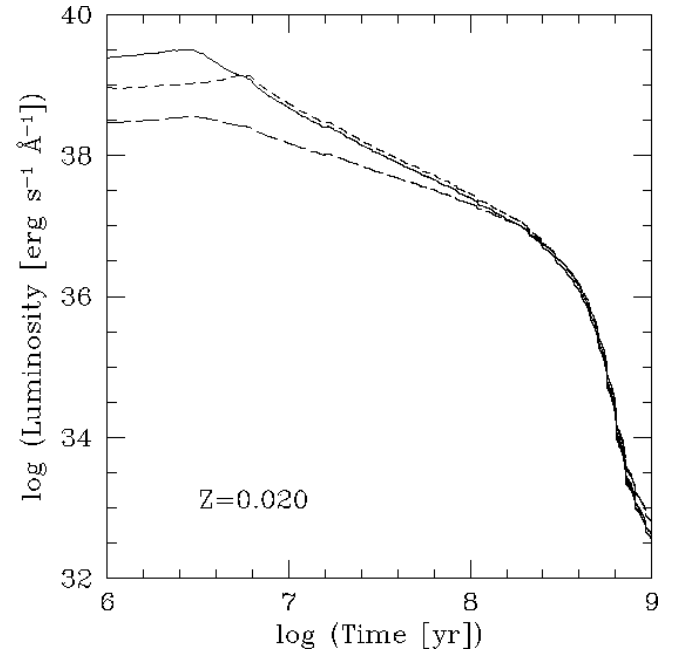


FIG. 53b

FIG. 53.—Monochromatic luminosity at 1500 \AA vs. time. Star formation law: instantaneous; solid line, $\alpha = 2.35$, $M_{\text{up}} = 100 M_{\odot}$; long-dashed line, $\alpha = 3.30$, $M_{\text{up}} = 100 M_{\odot}$; short-dashed line, $\alpha = 2.35$, $M_{\text{up}} = 30 M_{\odot}$; (a) $Z = 0.040$; (b) $Z = 0.020$; (c) $Z = 0.008$; (d) $Z = 0.004$; (e) $Z = 0.001$.

Luminosities at 1500 \AA (Figs. 53a–53e and 54a–54e) were computed by averaging over the wavelength interval $1490\text{--}1510 \text{ \AA}$. This wavelength becomes observable from the ground at redshifts larger than ~ 2 , and the luminosity at 1500 \AA is a useful indicator of the star formation rate, or, in

connection with the $H\alpha$ luminosity of dust obscuration (Pettini et al. 1997). The 1500 \AA luminosity is a very robust prediction, with few uncertainties since the continuum at this wavelength comes from well-understood late-O/early-B stars.

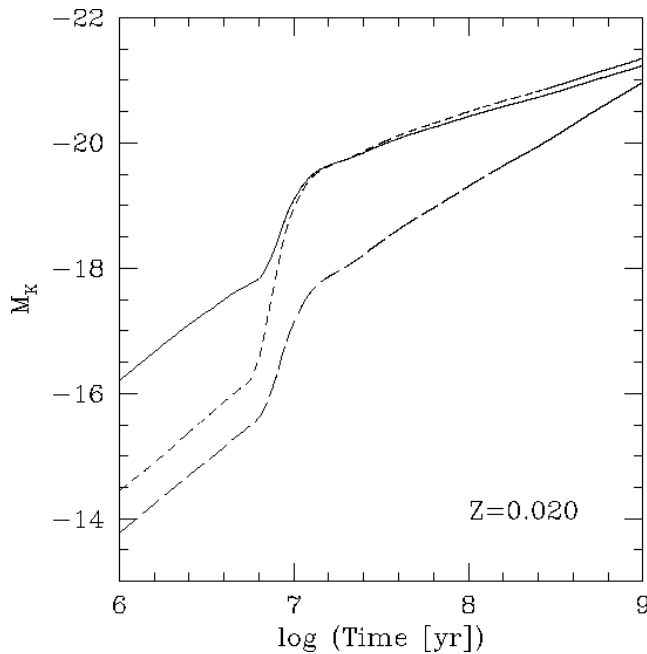


FIG. 52b

FIG. 52.—Absolute K magnitude vs. time. Star formation law: continuous; solid line, $\alpha = 2.35$, $M_{\text{up}} = 100 M_{\odot}$; long-dashed line, $\alpha = 3.30$, $M_{\text{up}} = 100 M_{\odot}$; short-dashed line, $\alpha = 2.35$, $M_{\text{up}} = 30 M_{\odot}$; (a) $Z = 0.040$; (b) $Z = 0.020$; (c) $Z = 0.008$; (d) $Z = 0.004$; (e) $Z = 0.001$.

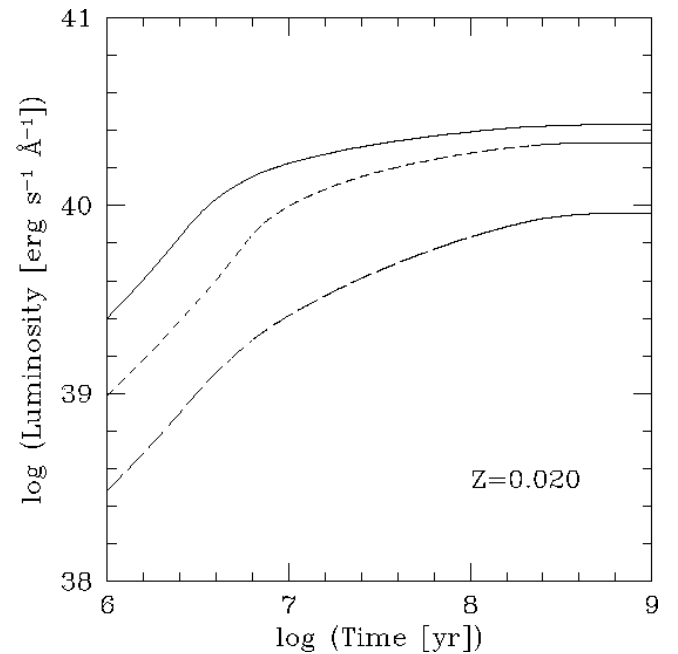


FIG. 54b

FIG. 54.—Monochromatic luminosity at 1500 \AA vs. time. Star formation law: continuous; solid line, $\alpha = 2.35$, $M_{\text{up}} = 100 M_{\odot}$; long-dashed line, $\alpha = 3.30$, $M_{\text{up}} = 100 M_{\odot}$; short-dashed line, $\alpha = 2.35$, $M_{\text{up}} = 30 M_{\odot}$; (a) $Z = 0.040$; (b) $Z = 0.020$; (c) $Z = 0.008$; (d) $Z = 0.004$; (e) $Z = 0.001$.

7. COLORS

Optical and near-infrared (IR) colors were calculated by convolving the spectral energy distributions with the filter profiles. The filters are in the Johnson (1966) system and are the same as in LH95. The zero point is defined by a star with $Z = 0.020$, $T_{\text{eff}} = 9400$ K, and $\log g = 3.95$, which has zero colors in all passbands. Colors in other photometric systems can be obtained by convolving the spectral energy distributions with the desired filter profiles.

These colors are available: $(U-B)$ (Figs. 55a–55e and 56a–56e), $(B-V)$ (Figs. 57a–57e and 58a–58e), $(V-R)$ (Figs. 59a–59e and 60a–60e), $(V-I)$ (Figs. 61a–61e and 62a–62e), $(V-J)$ (Figs. 63a–63e and 64a–64e), $(V-H)$ (Figs. 65a–65e and 66a–66e), $(V-K)$ (Figs. 67a–67e and 68a–68e), and $(V-L)$ (Figs. 69a–69e and 70a–70e). As a reminder, the *continuous* nebular emission is included in the colors, but not the line emission. The R filter is the most likely passband to suffer from nebular line contamination since $H\alpha$ is included. A first check of the expected degree of contamination can be made by comparing the $H\alpha$ equivalent widths of Figures 83a–83e and 84a–84e with the width of the R filter (about 2000 \AA). Line strengths of other strong lines in $H \text{ II}$ regions can be estimated from the photoionization models of Stasińska & Leitherer (1996).

The RSG issue raised before applies to some of the color plots for low metallicities as well. The strong metallicity dependence of the RSG feature around 10^7 yr is related to the effects discussed in § 6.

Rather than colors, we give continuum slopes in the UV. We define the slope β as the spectral index of the spectral energy distribution: $F_\lambda \propto \lambda^\beta$. Two indices are shown, one for the average slope between 1300 and 1800 \AA (Figs. 71a–71e and 72a–72e), and one for the 2200 – 2800 \AA region (Figs. 73a–73e and 74a–74e). The slopes were simply

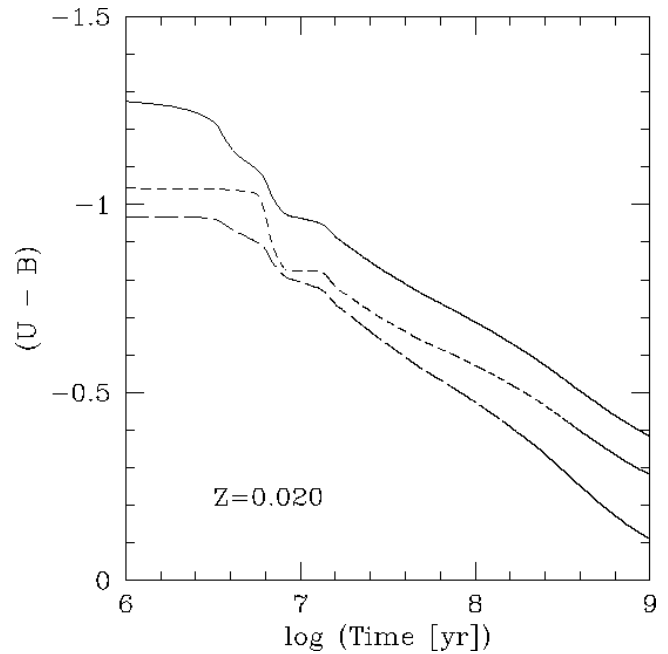


FIG. 56b

FIG. 56.— $(U-B)$ vs. time. Star formation law: continuous; solid line, $\alpha = 2.35$, $M_{\text{up}} = 100 M_\odot$; long-dashed line, $\alpha = 3.30$, $M_{\text{up}} = 100 M_\odot$; short-dashed line, $\alpha = 2.35$, $M_{\text{up}} = 30 M_\odot$; (a) $Z = 0.040$; (b) $Z = 0.020$; (c) $Z = 0.008$; (d) $Z = 0.004$; (e) $Z = 0.001$.

derived by fitting a first-order polynomial to the spectra through the wavelength intervals 1280 – 1320 \AA and 1780 – 1820 \AA for β_{1550} , and through 2180 – 2220 \AA and 2780 – 2820 \AA for β_{2500} . This should serve as an approximate guide for the variation of the slope with time but becomes increasingly meaningless if the actual spectrum deviates from a

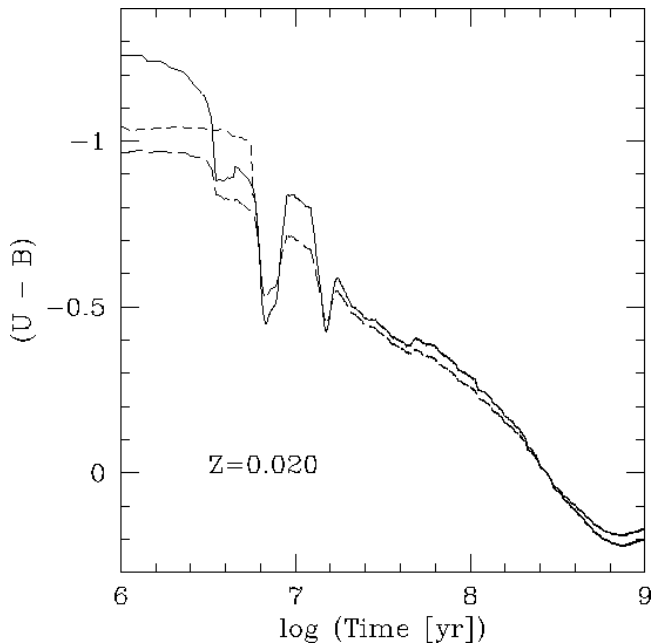


FIG. 55b

FIG. 55.— $(U-B)$ vs. time. Star formation law: instantaneous; solid line, $\alpha = 2.35$, $M_{\text{up}} = 100 M_\odot$; long-dashed line, $\alpha = 3.30$, $M_{\text{up}} = 100 M_\odot$; short-dashed line, $\alpha = 2.35$, $M_{\text{up}} = 30 M_\odot$; (a) $Z = 0.040$; (b) $Z = 0.020$; (c) $Z = 0.008$; (d) $Z = 0.004$; (e) $Z = 0.001$.

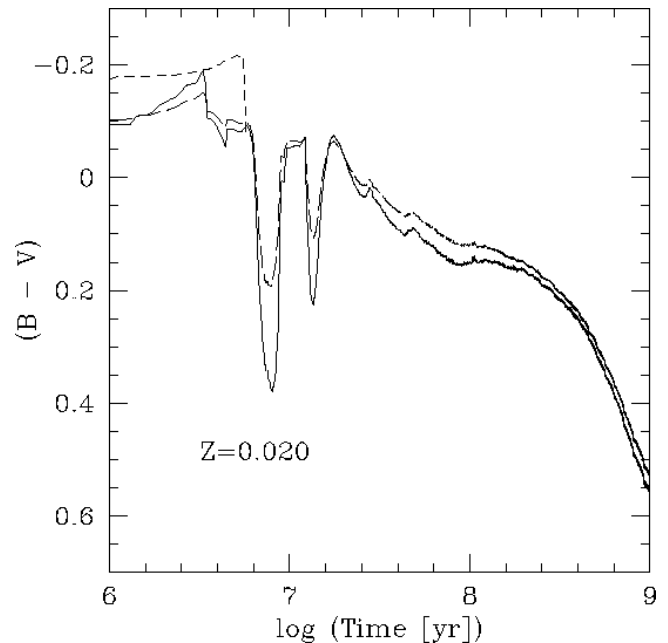


FIG. 57b

FIG. 57.— $(B-V)$ vs. time. Star formation law: instantaneous; solid line, $\alpha = 2.35$, $M_{\text{up}} = 100 M_\odot$; long-dashed line, $\alpha = 3.30$, $M_{\text{up}} = 100 M_\odot$; short-dashed line, $\alpha = 2.35$, $M_{\text{up}} = 30 M_\odot$; (a) $Z = 0.040$; (b) $Z = 0.020$; (c) $Z = 0.008$; (d) $Z = 0.004$; (e) $Z = 0.001$.

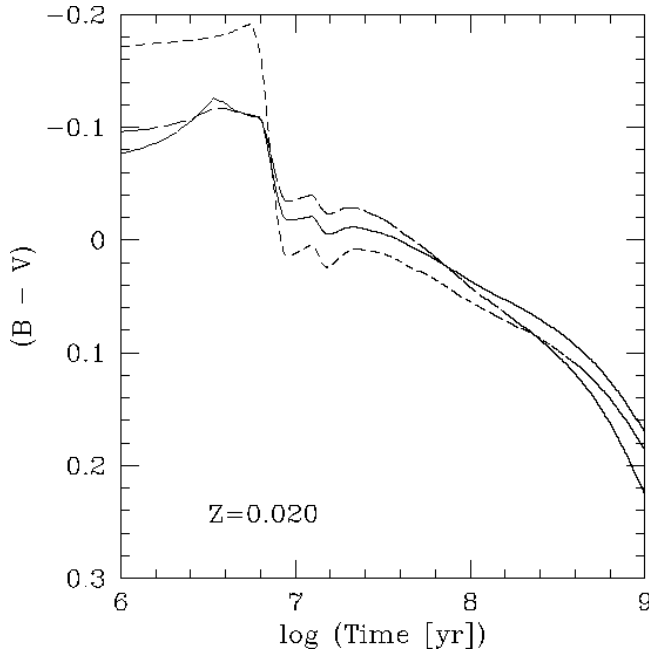


FIG. 58b

FIG. 58.— $(B-V)$ vs. time. Star formation law: continuous; *solid line*, $\alpha = 2.35$, $M_{\text{up}} = 100 M_{\odot}$; *long-dashed line*, $\alpha = 3.30$, $M_{\text{up}} = 100 M_{\odot}$; *short-dashed line*, $\alpha = 2.35$, $M_{\text{up}} = 30 M_{\odot}$; (a) $Z = 0.040$; (b) $Z = 0.020$; (c) $Z = 0.008$; (d) $Z = 0.004$; (e) $Z = 0.001$.

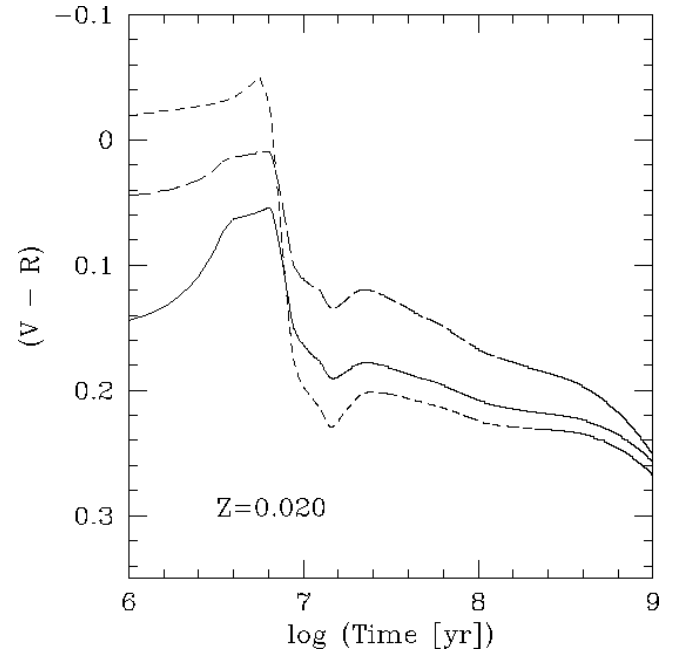


FIG. 60b

FIG. 60.— $(V-R)$ vs. time. Star formation law: continuous; *solid line*, $\alpha = 2.35$, $M_{\text{up}} = 100 M_{\odot}$; *long-dashed line*, $\alpha = 3.30$, $M_{\text{up}} = 100 M_{\odot}$; *short-dashed line*, $\alpha = 2.35$, $M_{\text{up}} = 30 M_{\odot}$; (a) $Z = 0.040$; (b) $Z = 0.020$; (c) $Z = 0.008$; (d) $Z = 0.004$; (e) $Z = 0.001$.

power law. Figures 1–6 suggest that spectral energy distributions with ages less than ~ 200 Myr are indeed well approximated by a power law in the UV but that this assumption is no longer correct at older ages. The UV slopes are quite independent of evolution and IMF effects

for the first 30 Myr. This property makes them very useful for deriving UV extinctions in galaxy spectra (Calzetti, Kinney, & Storchi-Bergmann 1994). Therefore, the spectral slope of the rest frame ultraviolet spectra of star-forming galaxies at high redshift can be used to estimate the effects

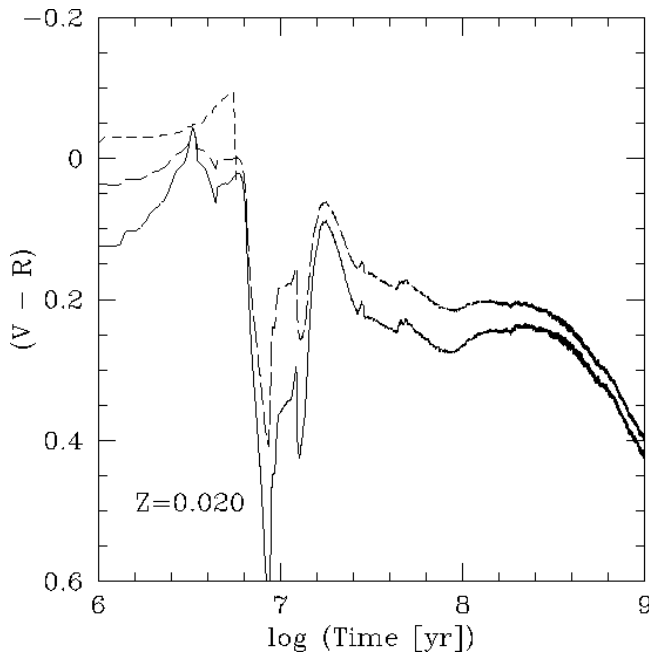


FIG. 59b

FIG. 59.— $(V-R)$ vs. time. Star formation law: instantaneous; *solid line*, $\alpha = 2.35$, $M_{\text{up}} = 100 M_{\odot}$; *long-dashed line*, $\alpha = 3.30$, $M_{\text{up}} = 100 M_{\odot}$; *short-dashed line*, $\alpha = 2.35$, $M_{\text{up}} = 30 M_{\odot}$; (a) $Z = 0.040$; (b) $Z = 0.020$; (c) $Z = 0.008$; (d) $Z = 0.004$; (e) $Z = 0.001$.

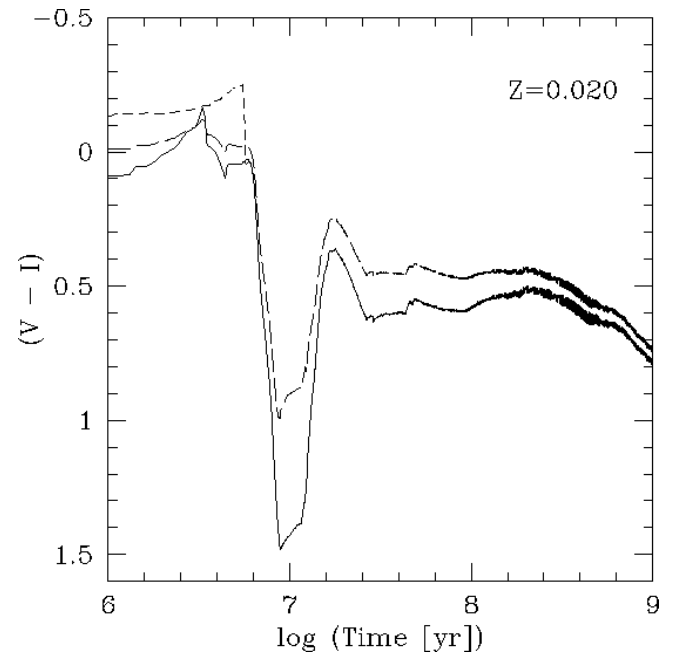


FIG. 61b

FIG. 61.— $(V-I)$ vs. time. Star formation law: instantaneous; *solid line*, $\alpha = 2.35$, $M_{\text{up}} = 100 M_{\odot}$; *long-dashed line*, $\alpha = 3.30$, $M_{\text{up}} = 100 M_{\odot}$; *short-dashed line*, $\alpha = 2.35$, $M_{\text{up}} = 30 M_{\odot}$; (a) $Z = 0.040$; (b) $Z = 0.020$; (c) $Z = 0.008$; (d) $Z = 0.004$; (e) $Z = 0.001$.

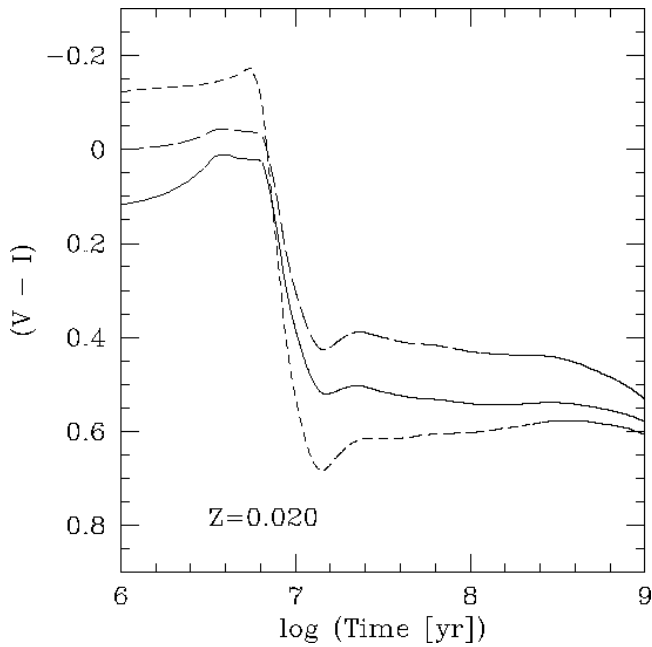


FIG. 62b

FIG. 62.— $(V-I)$ vs. time. Star formation law: continuous; *solid line*, $\alpha = 2.35$, $M_{\text{up}} = 100 M_{\odot}$; *long-dashed line*, $\alpha = 3.30$, $M_{\text{up}} = 100 M_{\odot}$; *short-dashed line*, $\alpha = 2.35$, $M_{\text{up}} = 30 M_{\odot}$; (a) $Z = 0.040$; (b) $Z = 0.020$; (c) $Z = 0.008$; (d) $Z = 0.004$; (e) $Z = 0.001$.

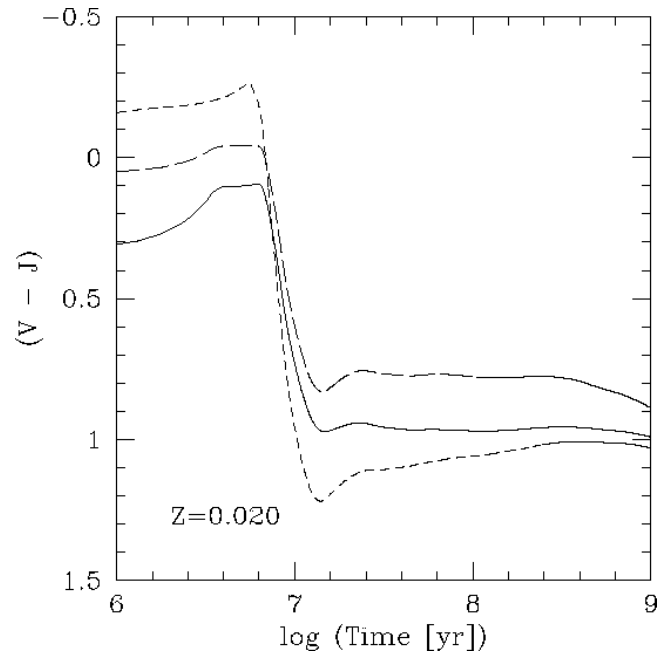


FIG. 64b

FIG. 64.— $(V-J)$ vs. time. Star formation law: continuous; *solid line*, $\alpha = 2.35$, $M_{\text{up}} = 100 M_{\odot}$; *long-dashed line*, $\alpha = 3.30$, $M_{\text{up}} = 100 M_{\odot}$; *short-dashed line*, $\alpha = 2.35$, $M_{\text{up}} = 30 M_{\odot}$; (a) $Z = 0.040$; (b) $Z = 0.020$; (c) $Z = 0.008$; (d) $Z = 0.004$; (e) $Z = 0.001$.

of dust obscuration in the early universe (Calzetti & Heckman 1999 and references therein).

8. FAR-ULTRAVIOLET PROPERTIES

The predictions in this section rely on our capabilities to model the stellar far-UV continuum below 912 Å since this

spectral region is generally not accessible to direct observations. A comparison between different models for *hot stars* in this spectral region has been made by Schaerer & de Koter (1997). The *internal* consistency, as judged from differences between the models, is within 0.1 dex between 912 and 504 Å, which is relevant for the flux ionizing neutral

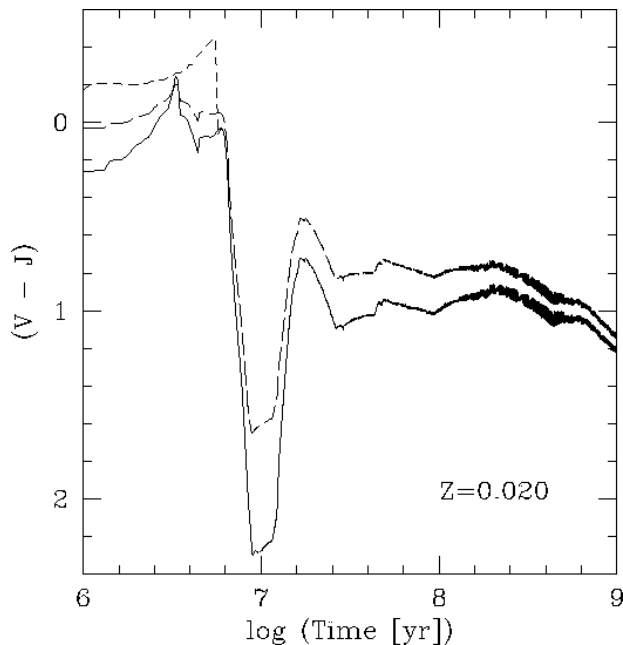


FIG. 63b

FIG. 63.— $(V-J)$ vs. time. Star formation law: instantaneous; *solid line*, $\alpha = 2.35$, $M_{\text{up}} = 100 M_{\odot}$; *long-dashed line*, $\alpha = 3.30$, $M_{\text{up}} = 100 M_{\odot}$; *short-dashed line*, $\alpha = 2.35$, $M_{\text{up}} = 30 M_{\odot}$; (a) $Z = 0.040$; (b) $Z = 0.020$; (c) $Z = 0.008$; (d) $Z = 0.004$; (e) $Z = 0.001$.

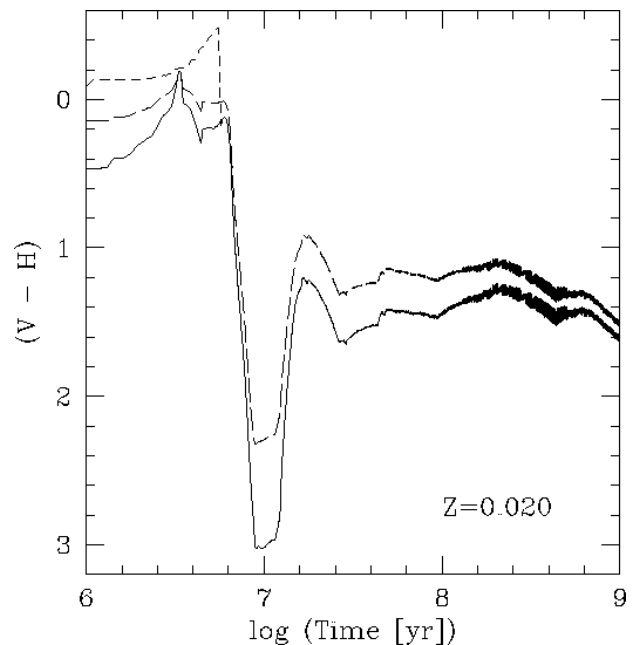


FIG. 65b

FIG. 65.— $(V-H)$ vs. time. Star formation law: instantaneous; *solid line*, $\alpha = 2.35$, $M_{\text{up}} = 100 M_{\odot}$; *long-dashed line*, $\alpha = 3.30$, $M_{\text{up}} = 100 M_{\odot}$; *short-dashed line*, $\alpha = 2.35$, $M_{\text{up}} = 30 M_{\odot}$; (a) $Z = 0.040$; (b) $Z = 0.020$; (c) $Z = 0.008$; (d) $Z = 0.004$; (e) $Z = 0.001$.

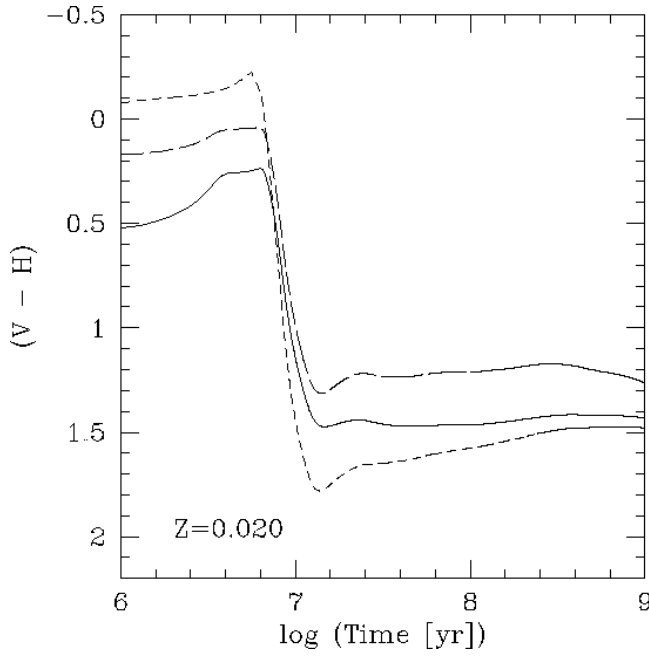


FIG. 66b

FIG. 66.— $(V-H)$ vs. time. Star formation law: continuous; *solid line*, $\alpha = 2.35$, $M_{\text{up}} = 100 M_{\odot}$; *long-dashed line*, $\alpha = 3.30$, $M_{\text{up}} = 100 M_{\odot}$; *short-dashed line*, $\alpha = 2.35$, $M_{\text{up}} = 30 M_{\odot}$; (a) $Z = 0.040$; (b) $Z = 0.020$; (c) $Z = 0.008$; (d) $Z = 0.004$; (e) $Z = 0.001$.

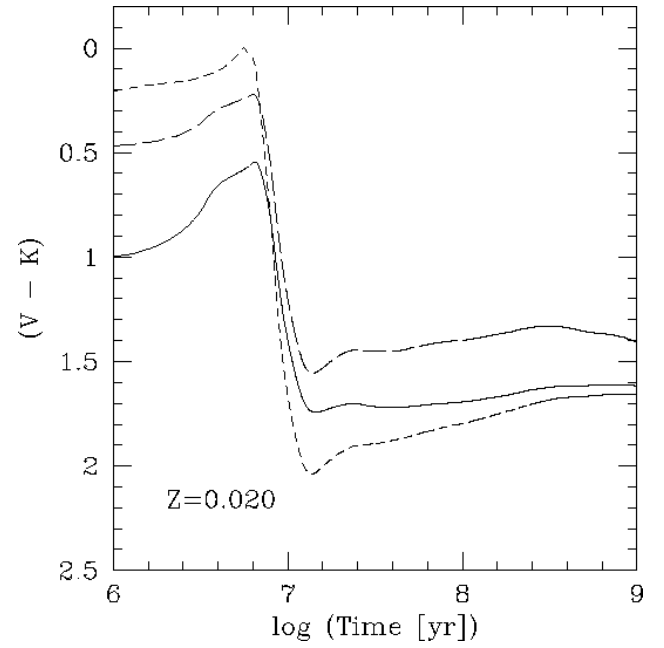


FIG. 68b

FIG. 68.— $(V-K)$ vs. time. Star formation law: continuous; *solid line*, $\alpha = 2.35$, $M_{\text{up}} = 100 M_{\odot}$; *long-dashed line*, $\alpha = 3.30$, $M_{\text{up}} = 100 M_{\odot}$; *short-dashed line*, $\alpha = 2.35$, $M_{\text{up}} = 30 M_{\odot}$; (a) $Z = 0.040$; (b) $Z = 0.020$; (c) $Z = 0.008$; (d) $Z = 0.004$; (e) $Z = 0.001$.

hydrogen $[N(\text{H}^0)]$. Uncertainties become larger toward shorter wavelengths, in particular below 228 \AA , where the emergent flux becomes strongly dependent on stellar-wind properties. This of course leaves open the question of the *external, absolute* uncertainties. Model atmospheres generally do a good job above 228 \AA when combined with photo-

ionization models and compared to H II region spectra (García-Vargas 1996), although there are some properties that are sensitive to the flux distribution in the neutral He continuum (Stasińska & Schaerer 1997). This makes errors in the integrated photon fluxes by more than 0.3 dex

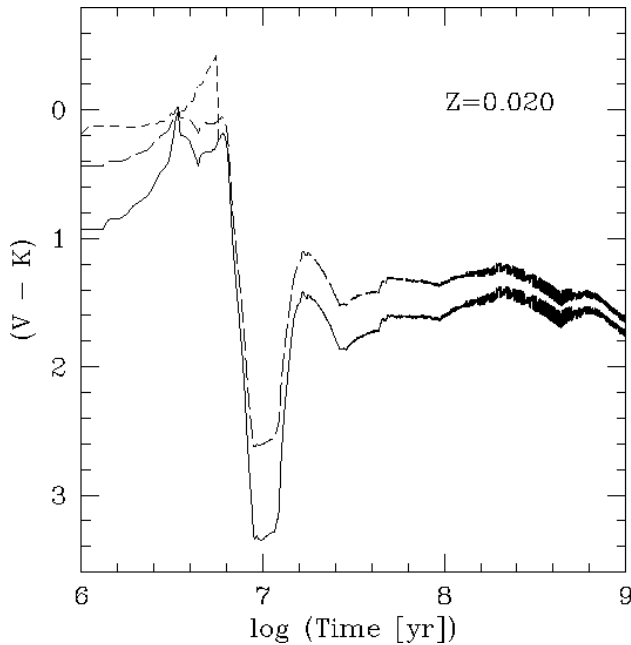


FIG. 67b

FIG. 67.— $(V-K)$ vs. time. Star formation law: instantaneous; *solid line*, $\alpha = 2.35$, $M_{\text{up}} = 100 M_{\odot}$; *long-dashed line*, $\alpha = 3.30$, $M_{\text{up}} = 100 M_{\odot}$; *short-dashed line*, $\alpha = 2.35$, $M_{\text{up}} = 30 M_{\odot}$; (a) $Z = 0.040$; (b) $Z = 0.020$; (c) $Z = 0.008$; (d) $Z = 0.004$; (e) $Z = 0.001$.

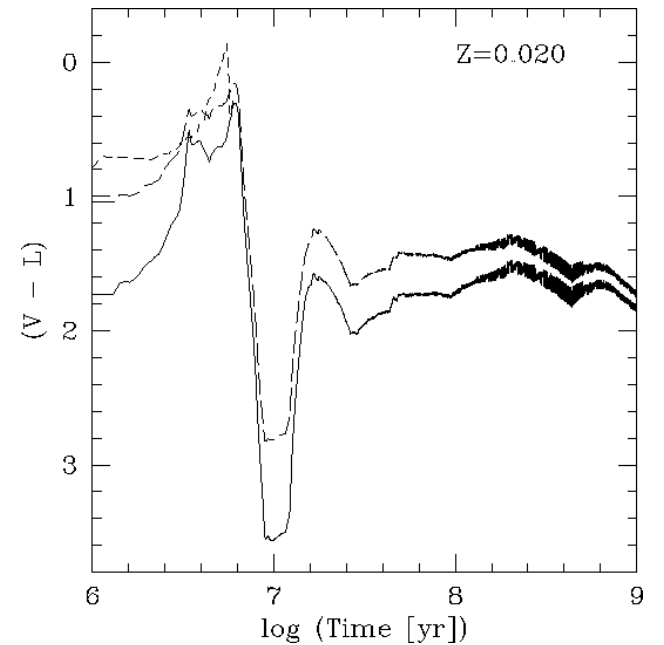


FIG. 69b

FIG. 69.— $(V-L)$ vs. time. Star formation law: instantaneous; *solid line*, $\alpha = 2.35$, $M_{\text{up}} = 100 M_{\odot}$; *long-dashed line*, $\alpha = 3.30$, $M_{\text{up}} = 100 M_{\odot}$; *short-dashed line*, $\alpha = 2.35$, $M_{\text{up}} = 30 M_{\odot}$; (a) $Z = 0.040$; (b) $Z = 0.020$; (c) $Z = 0.008$; (d) $Z = 0.004$; (e) $Z = 0.001$.

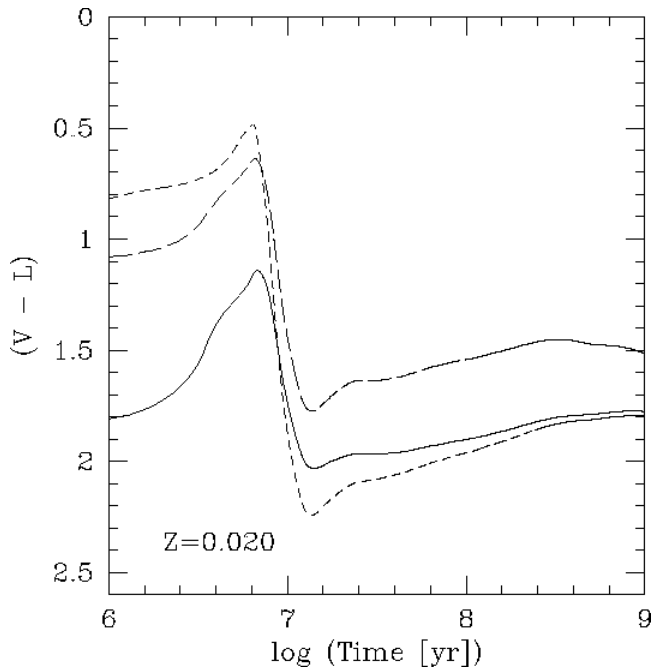


FIG. 70b

FIG. 70.— $(V-L)$ vs. time. Star formation law: continuous; solid line, $\alpha = 2.35$, $M_{\text{up}} = 100 M_{\odot}$; long-dashed line, $\alpha = 3.30$, $M_{\text{up}} = 100 M_{\odot}$; short-dashed line, $\alpha = 2.35$, $M_{\text{up}} = 30 M_{\odot}$; (a) $Z = 0.040$; (b) $Z = 0.020$; (c) $Z = 0.008$; (d) $Z = 0.004$; (e) $Z = 0.001$.

unlikely. The region below 228 \AA has not yet been tested in such detail, and the uncertainties are potentially large.

Far-UV models for stars colder than about $30,000 \text{ K}$ (types B and later) are lagging behind. Cassinelli et al. (1995) found discrepancies by 2 orders of magnitude between the

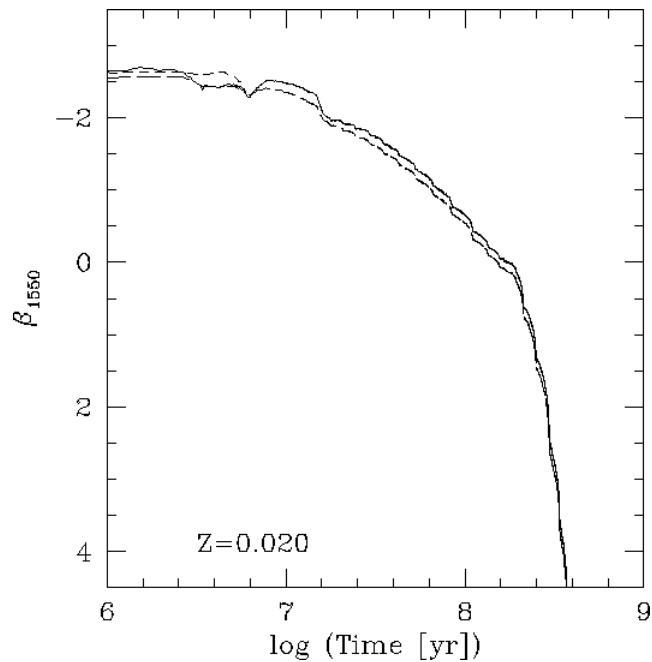


FIG. 71b

FIG. 71.—Slope of L_{λ} between 1200 and 1900 \AA vs. time. Star formation law: instantaneous; solid line, $\alpha = 2.35$, $M_{\text{up}} = 100 M_{\odot}$; long-dashed line, $\alpha = 3.30$, $M_{\text{up}} = 100 M_{\odot}$; short-dashed line, $\alpha = 2.35$, $M_{\text{up}} = 30 M_{\odot}$; (a) $Z = 0.040$; (b) $Z = 0.020$; (c) $Z = 0.008$; (d) $Z = 0.004$; (e) $Z = 0.001$.

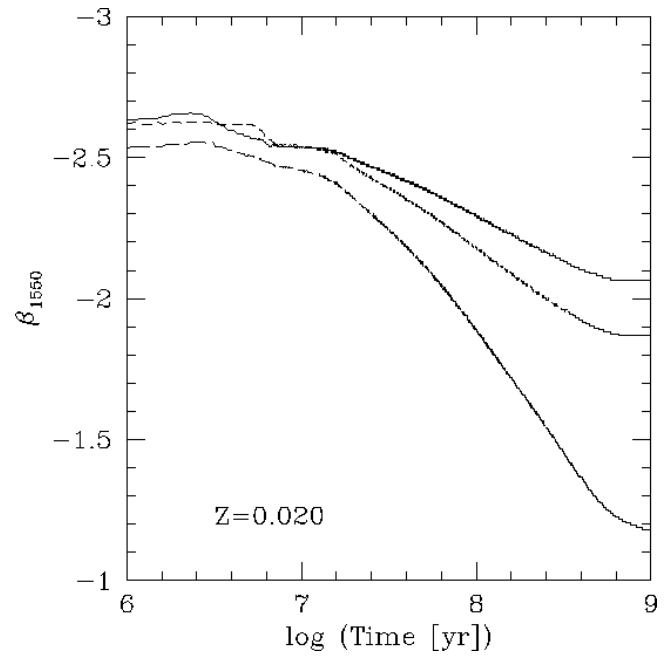


FIG. 72b

FIG. 72.—Slope of L_{λ} between 1200 and 1900 \AA vs. time. Star formation law: continuous; solid line, $\alpha = 2.35$, $M_{\text{up}} = 100 M_{\odot}$; long-dashed line, $\alpha = 3.30$, $M_{\text{up}} = 100 M_{\odot}$; short-dashed line, $\alpha = 2.35$, $M_{\text{up}} = 30 M_{\odot}$; (a) $Z = 0.040$; (b) $Z = 0.020$; (c) $Z = 0.008$; (d) $Z = 0.004$; (e) $Z = 0.001$.

observed extreme-UV flux of the B2 star $\epsilon \text{ CMa}$ and model predictions. Even slight errors in the adopted wind parameters can produce huge far-UV flux variations at these relatively low temperatures (Schaerer & de Koter 1997).

We define the Lyman break as the ratio of the average flux in the wavelength interval $1080\text{--}1120 \text{ \AA}$ over that

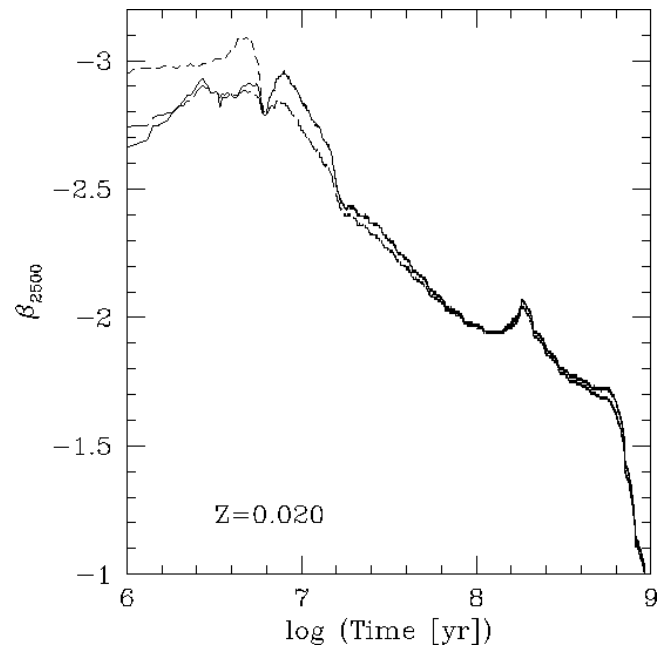


FIG. 73b

FIG. 73.—Slope of L_{λ} between 2200 and 2800 \AA vs. time. Star formation law: instantaneous; solid line, $\alpha = 2.35$, $M_{\text{up}} = 100 M_{\odot}$; long-dashed line, $\alpha = 3.30$, $M_{\text{up}} = 100 M_{\odot}$; short-dashed line, $\alpha = 2.35$, $M_{\text{up}} = 30 M_{\odot}$; (a) $Z = 0.040$; (b) $Z = 0.020$; (c) $Z = 0.008$; (d) $Z = 0.004$; (e) $Z = 0.001$.

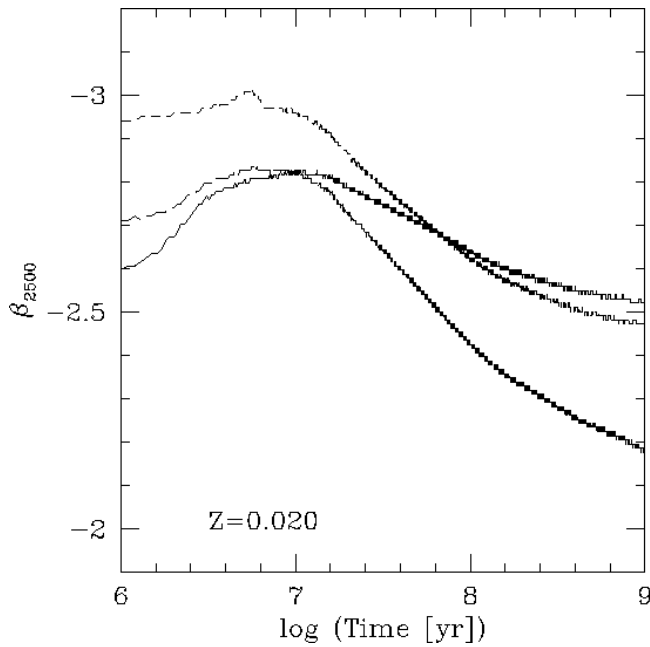


FIG. 74b

FIG. 74.—Slope of L_λ between 2200 and 2800 Å vs. time. Star formation law: continuous; solid line, $\alpha = 2.35$, $M_{\text{up}} = 100 M_\odot$; long-dashed line, $\alpha = 3.30$, $M_{\text{up}} = 100 M_\odot$; short-dashed line, $\alpha = 2.35$, $M_{\text{up}} = 30 M_\odot$; (a) $Z = 0.040$; (b) $Z = 0.020$; (c) $Z = 0.008$; (d) $Z = 0.004$; (e) $Z = 0.001$.

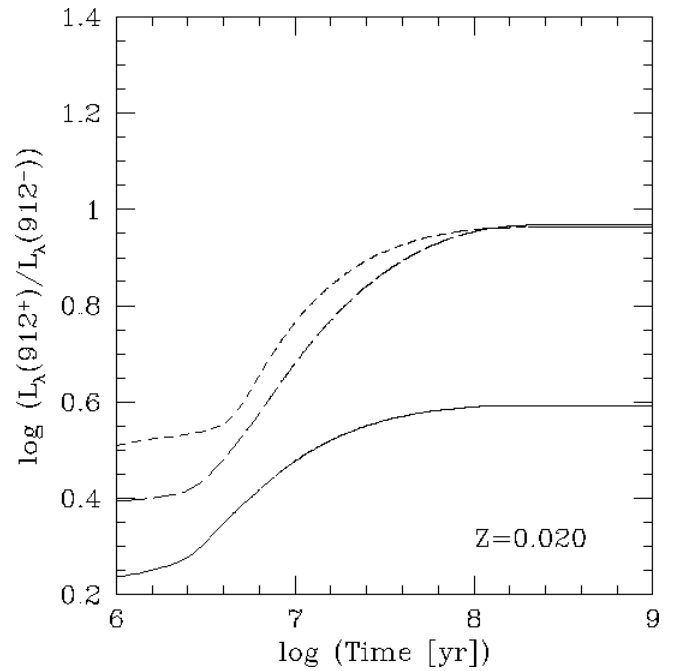


FIG. 76b

FIG. 76.—Lyman discontinuity vs. time. Star formation law: continuous; solid line, $\alpha = 2.35$, $M_{\text{up}} = 100 M_\odot$; long-dashed line, $\alpha = 3.30$, $M_{\text{up}} = 100 M_\odot$; short-dashed line, $\alpha = 2.35$, $M_{\text{up}} = 30 M_\odot$; (a) $Z = 0.040$; (b) $Z = 0.020$; (c) $Z = 0.008$; (d) $Z = 0.004$; (e) $Z = 0.001$.

between 870 and 900 Å. These wavelength intervals are relatively free of line-blanketing so that we measure mostly temperature rather than line opacity. The Lyman break is about a factor of 2–3 in O-star dominated phases and drops thereafter (Figs. 75a–75e and 76a–76e). The warnings about

model uncertainties for the Lyman continuum of cooler stars apply to the instantaneous case. Figures 75a–75e should not be overinterpreted after about 50 Myr since B stars like ϵ CMa (see previous paragraph) could dominate.

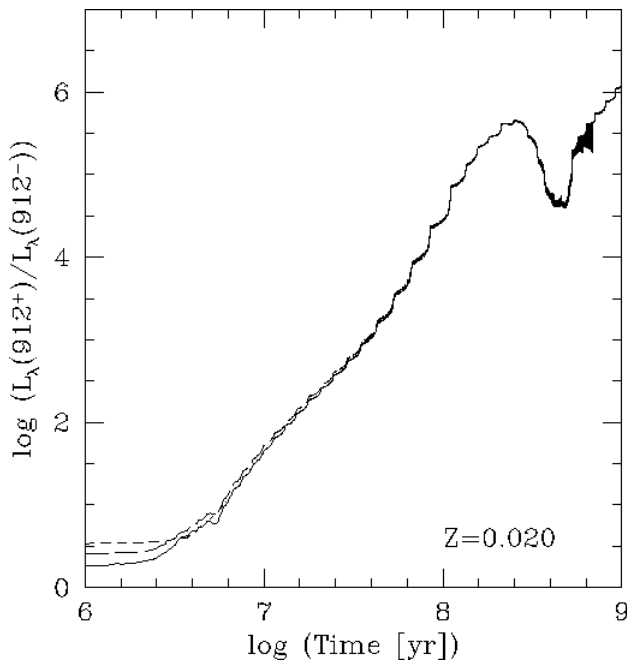


FIG. 75b

FIG. 75.—Lyman discontinuity vs. time. Star formation law: instantaneous; solid line, $\alpha = 2.35$, $M_{\text{up}} = 100 M_\odot$; long-dashed line, $\alpha = 3.30$, $M_{\text{up}} = 100 M_\odot$; short-dashed line, $\alpha = 2.35$, $M_{\text{up}} = 30 M_\odot$; (a) $Z = 0.040$; (b) $Z = 0.020$; (c) $Z = 0.008$; (d) $Z = 0.004$; (e) $Z = 0.001$.

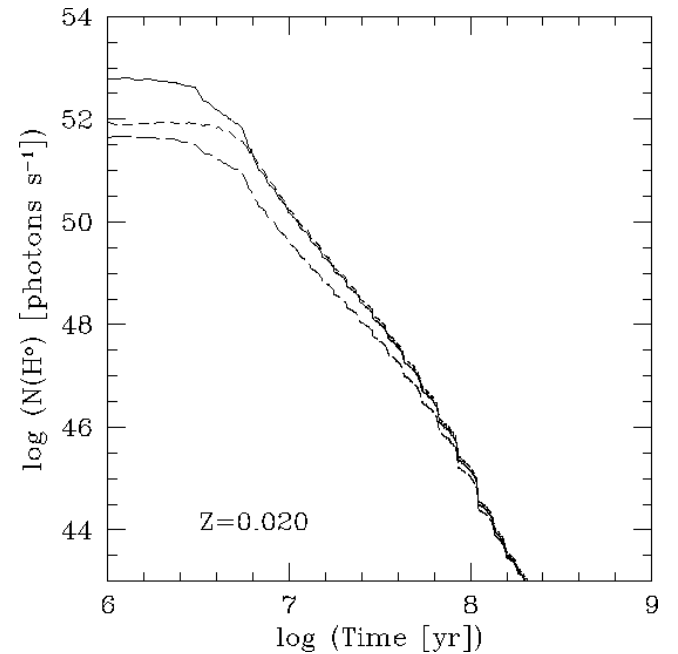


FIG. 77b

FIG. 77.—Number of photons with wavelength below 912 Å vs. time. Star formation law: instantaneous; solid line, $\alpha = 2.35$, $M_{\text{up}} = 100 M_\odot$; long-dashed line, $\alpha = 3.30$, $M_{\text{up}} = 100 M_\odot$; short-dashed line, $\alpha = 2.35$, $M_{\text{up}} = 30 M_\odot$; (a) $Z = 0.040$; (b) $Z = 0.020$; (c) $Z = 0.008$; (d) $Z = 0.004$; (e) $Z = 0.001$.

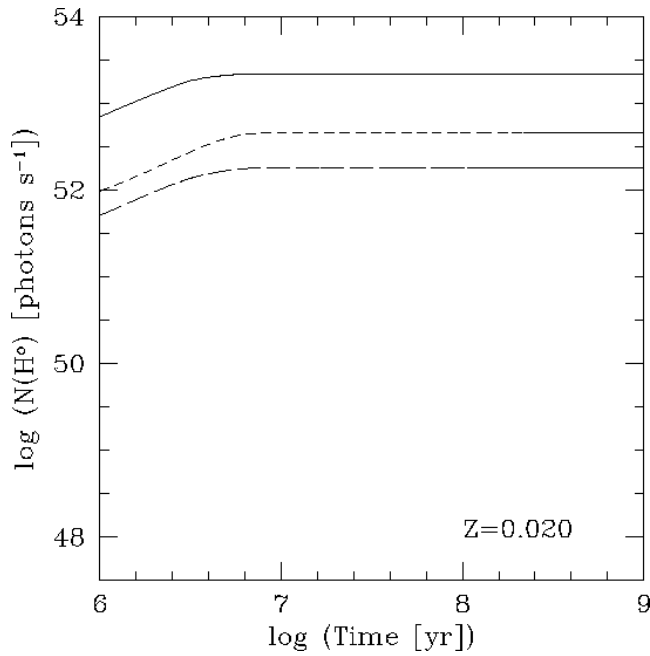


FIG. 78b

FIG. 78.—Number of photons with wavelength below 912 Å vs. time. Star formation law: continuous; solid line, $\alpha = 2.35$, $M_{\text{up}} = 100 M_{\odot}$; long-dashed line, $\alpha = 3.30$, $M_{\text{up}} = 100 M_{\odot}$; short-dashed line, $\alpha = 2.35$, $M_{\text{up}} = 30 M_{\odot}$; (a) $Z = 0.040$; (b) $Z = 0.020$; (c) $Z = 0.008$; (d) $Z = 0.004$; (e) $Z = 0.001$.

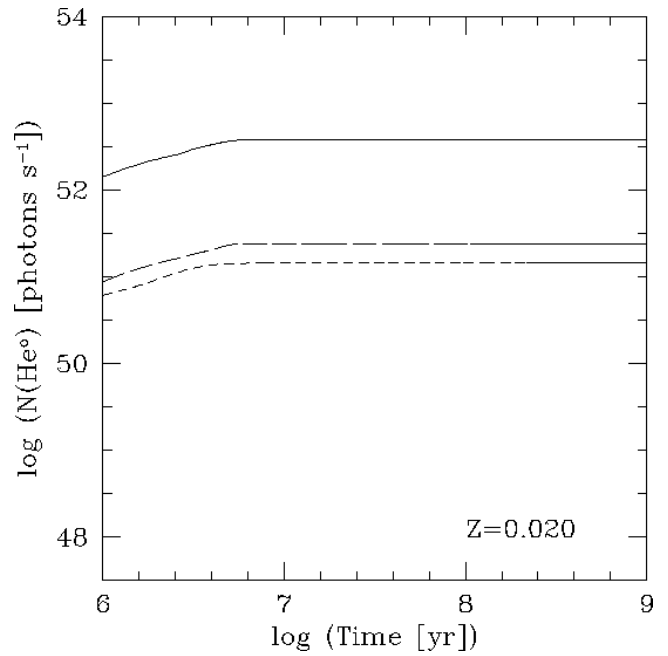


FIG. 80b

FIG. 80.—Number of photons with wavelength below 504 Å vs. time. Star formation law: continuous; solid line, $\alpha = 2.35$, $M_{\text{up}} = 100 M_{\odot}$; long-dashed line, $\alpha = 3.30$, $M_{\text{up}} = 100 M_{\odot}$; short-dashed line, $\alpha = 2.35$, $M_{\text{up}} = 30 M_{\odot}$; (a) $Z = 0.040$; (b) $Z = 0.020$; (c) $Z = 0.008$; (d) $Z = 0.004$; (e) $Z = 0.001$.

The Lyman break for a continuous population is always dominated by hot stars so that Figures 76a–76e can be trusted over the entire range plotted.

The number of photons capable of ionizing neutral hydrogen [$N(\text{H}^0)$], neutral helium [$N(\text{He}^0)$], and ionized

helium [$N(\text{He}^+)$] were calculated by integration of the spectra below 912 Å, 504 Å, and 228 Å, respectively. They are shown in Figures 77a–77e and 78a–78e [$N(\text{H}^0)$], Figures 79a–79e and 80a–80e [$N(\text{He}^0)$], and Figures

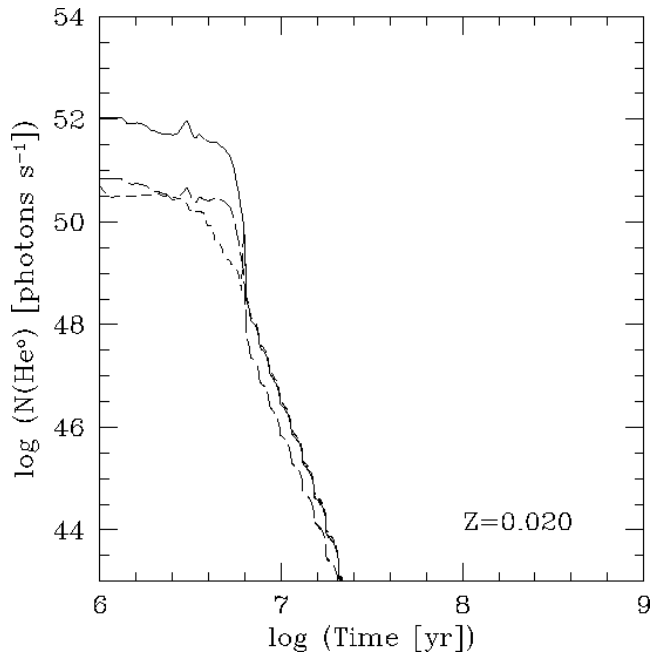


FIG. 79b

FIG. 79.—Number of photons with wavelength below 504 Å vs. time. Star formation law: instantaneous; solid line, $\alpha = 2.35$, $M_{\text{up}} = 100 M_{\odot}$; long-dashed line, $\alpha = 3.30$, $M_{\text{up}} = 100 M_{\odot}$; short-dashed line, $\alpha = 2.35$, $M_{\text{up}} = 30 M_{\odot}$; (a) $Z = 0.040$; (b) $Z = 0.020$; (c) $Z = 0.008$; (d) $Z = 0.004$; (e) $Z = 0.001$.

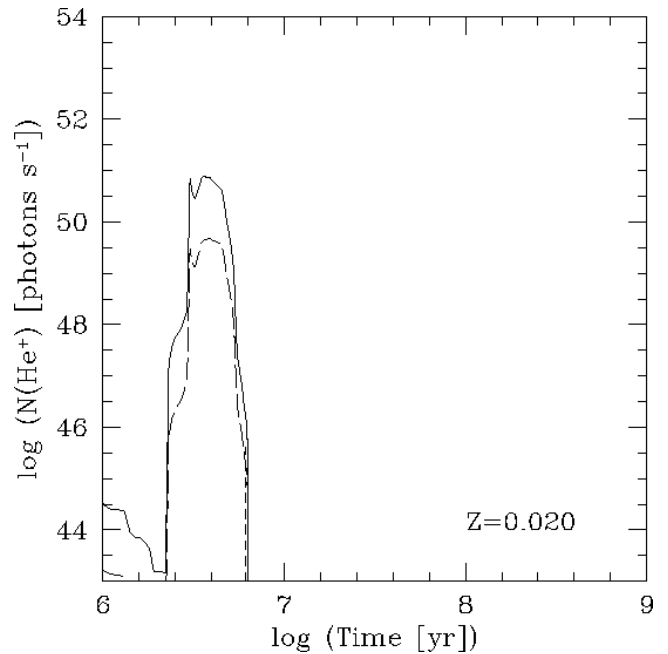


FIG. 81b

FIG. 81.—Number of photons with wavelength below 228 Å vs. time. Star formation law: instantaneous; solid line, $\alpha = 2.35$, $M_{\text{up}} = 100 M_{\odot}$; long-dashed line, $\alpha = 3.30$, $M_{\text{up}} = 100 M_{\odot}$; short-dashed line, $\alpha = 2.35$, $M_{\text{up}} = 30 M_{\odot}$; (a) $Z = 0.040$; (b) $Z = 0.020$; (c) $Z = 0.008$; (d) $Z = 0.004$; (e) $Z = 0.001$.

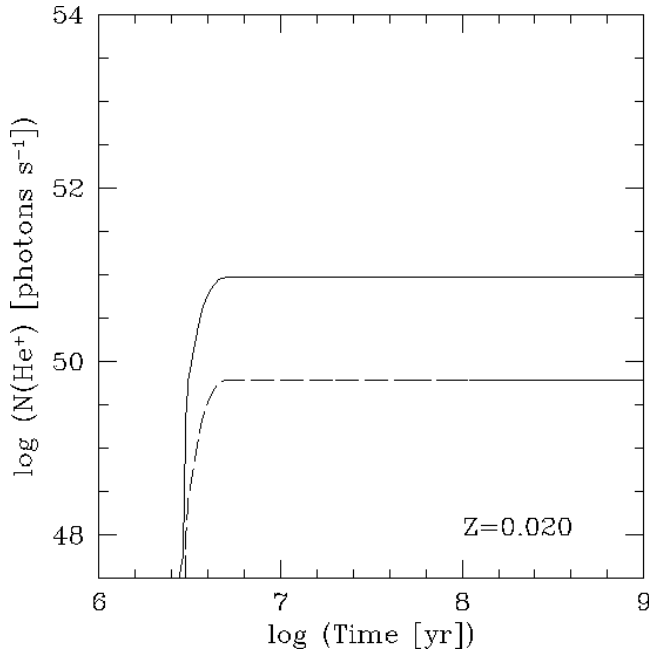


FIG. 82b

FIG. 82.—Number of photons with wavelength below 228 Å vs. time. Star formation law: continuous; solid line, $\alpha = 2.35$, $M_{\text{up}} = 100 M_{\odot}$; long-dashed line, $\alpha = 3.30$, $M_{\text{up}} = 100 M_{\odot}$; short-dashed line, $\alpha = 2.35$, $M_{\text{up}} = 30 M_{\odot}$; (a) $Z = 0.040$; (b) $Z = 0.020$; (c) $Z = 0.008$; (d) $Z = 0.004$; (e) $Z = 0.001$.

81a–81e and 82a–82e [$N(\text{He}^+)$]. As stated before, the numbers become increasingly uncertain with shorter wavelength. $N(\text{He}^+)$ is almost entirely produced by WR stars, and uncertainties in the wind properties enter.

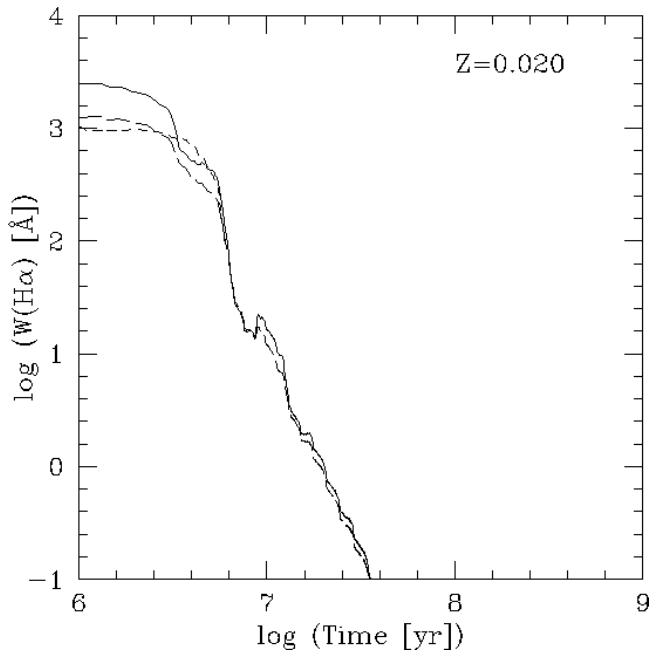


FIG. 83b

FIG. 83.—Hα equivalent width vs. time. Star formation law: instantaneous; solid line, $\alpha = 2.35$, $M_{\text{up}} = 100 M_{\odot}$; long-dashed line, $\alpha = 3.30$, $M_{\text{up}} = 100 M_{\odot}$; short-dashed line, $\alpha = 2.35$, $M_{\text{up}} = 30 M_{\odot}$; (a) $Z = 0.040$; (b) $Z = 0.020$; (c) $Z = 0.008$; (d) $Z = 0.004$; (e) $Z = 0.001$.

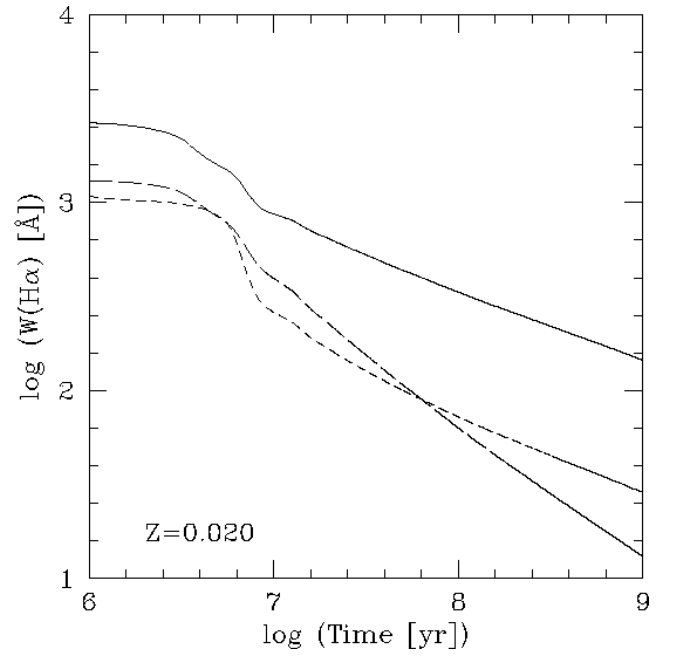


FIG. 84b

FIG. 84.—Hα equivalent width vs. time. Star formation law: continuous; solid line, $\alpha = 2.35$, $M_{\text{up}} = 100 M_{\odot}$; long-dashed line, $\alpha = 3.30$, $M_{\text{up}} = 100 M_{\odot}$; short-dashed line, $\alpha = 2.35$, $M_{\text{up}} = 30 M_{\odot}$; (a) $Z = 0.040$; (b) $Z = 0.020$; (c) $Z = 0.008$; (d) $Z = 0.004$; (e) $Z = 0.001$.

We also give equivalent widths of several popular hydrogen recombination lines. The continuum is taken from the model atmospheres and does not include underlying stellar absorption. The nebular continuum is of course taken into

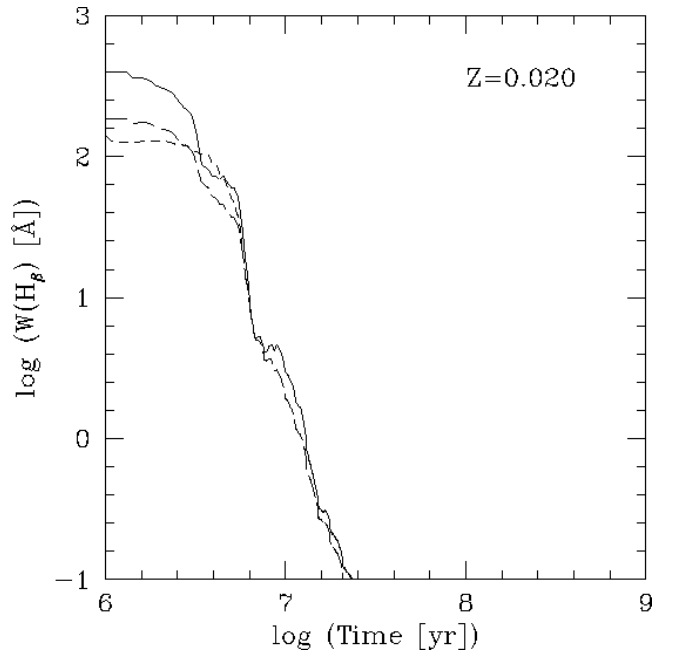


FIG. 85b

FIG. 85.—Hβ equivalent width vs. time. Star formation law: instantaneous; solid line, $\alpha = 2.35$, $M_{\text{up}} = 100 M_{\odot}$; long-dashed line, $\alpha = 3.30$, $M_{\text{up}} = 100 M_{\odot}$; short-dashed line, $\alpha = 2.35$, $M_{\text{up}} = 30 M_{\odot}$; (a) $Z = 0.040$; (b) $Z = 0.020$; (c) $Z = 0.008$; (d) $Z = 0.004$; (e) $Z = 0.001$.

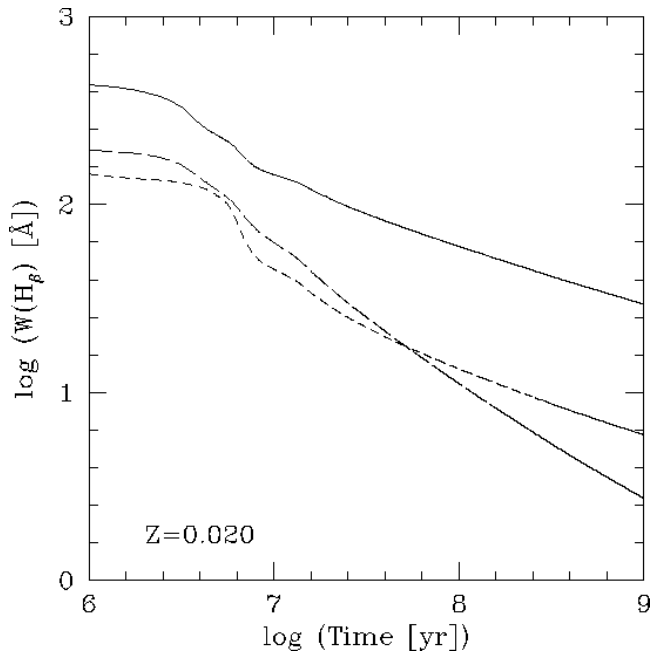


FIG. 86b

FIG. 86.—H β equivalent width vs. time. Star formation law: continuous; solid line, $\alpha = 2.35$, $M_{\text{up}} = 100 M_{\odot}$; long-dashed line, $\alpha = 3.30$, $M_{\text{up}} = 100 M_{\odot}$; short-dashed line, $\alpha = 2.35$, $M_{\text{up}} = 30 M_{\odot}$; (a) $Z = 0.040$; (b) $Z = 0.020$; (c) $Z = 0.008$; (d) $Z = 0.004$; (e) $Z = 0.001$.

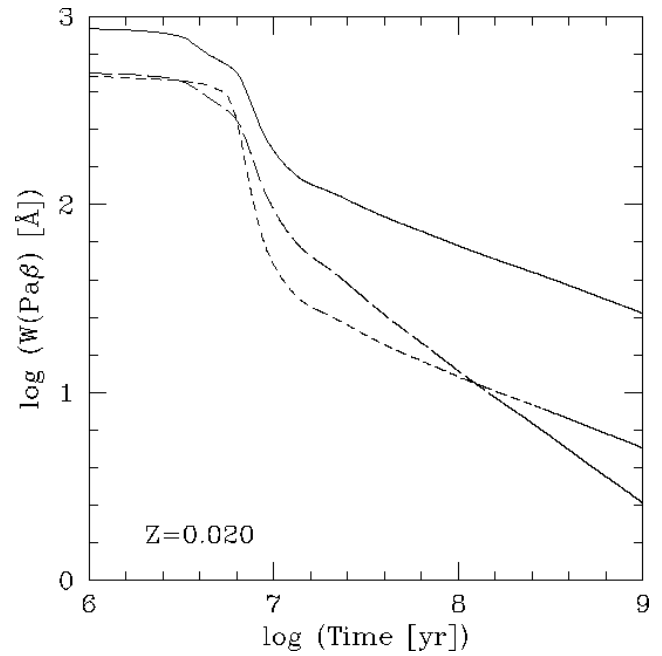


FIG. 88b

FIG. 88.—Pa β equivalent width vs. time. Star formation law: continuous; solid line, $\alpha = 2.35$, $M_{\text{up}} = 100 M_{\odot}$; long-dashed line, $\alpha = 3.30$, $M_{\text{up}} = 100 M_{\odot}$; short-dashed line, $\alpha = 2.35$, $M_{\text{up}} = 30 M_{\odot}$; (a) $Z = 0.040$; (b) $Z = 0.020$; (c) $Z = 0.008$; (d) $Z = 0.004$; (e) $Z = 0.001$.

account. The individual plots are for H α (Figs. 83a–83e and 84a–84e), H β (Figs. 85a–85e and 86a–86e), Pa β (Figs. 87a–87e and 88a–88e), and Br γ (Figs. 89a–89e and 90a–90e). The transformation relations from $N(\text{H}^0)$ to the line luminosities are in LH95.

9. OTHER DIAGNOSTIC LINES

In this section we present a few more diagnostics that can be useful to isolate a stellar population in a galaxy spectrum. They are all related to stars off the main sequence: WR stars, RSGs, and SNe.

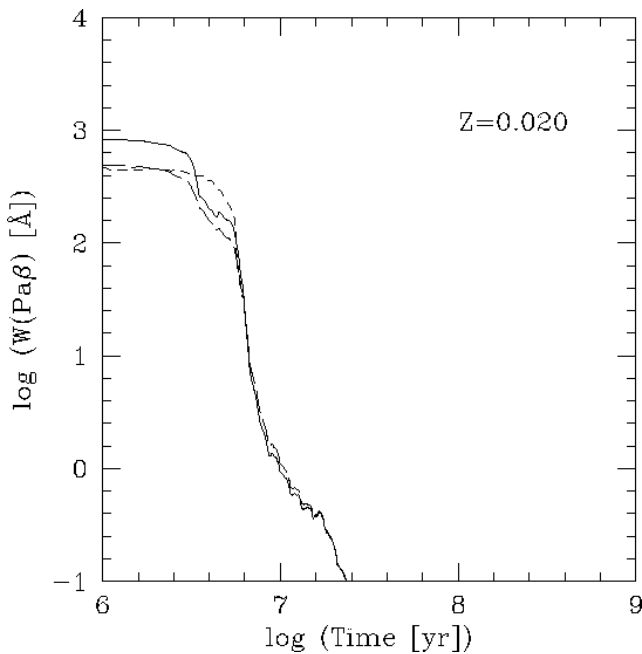


FIG. 87b

FIG. 87.—Pa β equivalent width vs. time. Star formation law: instantaneous; solid line, $\alpha = 2.35$, $M_{\text{up}} = 100 M_{\odot}$; long-dashed line, $\alpha = 3.30$, $M_{\text{up}} = 100 M_{\odot}$; short-dashed line, $\alpha = 2.35$, $M_{\text{up}} = 30 M_{\odot}$; (a) $Z = 0.040$; (b) $Z = 0.020$; (c) $Z = 0.008$; (d) $Z = 0.004$; (e) $Z = 0.001$.

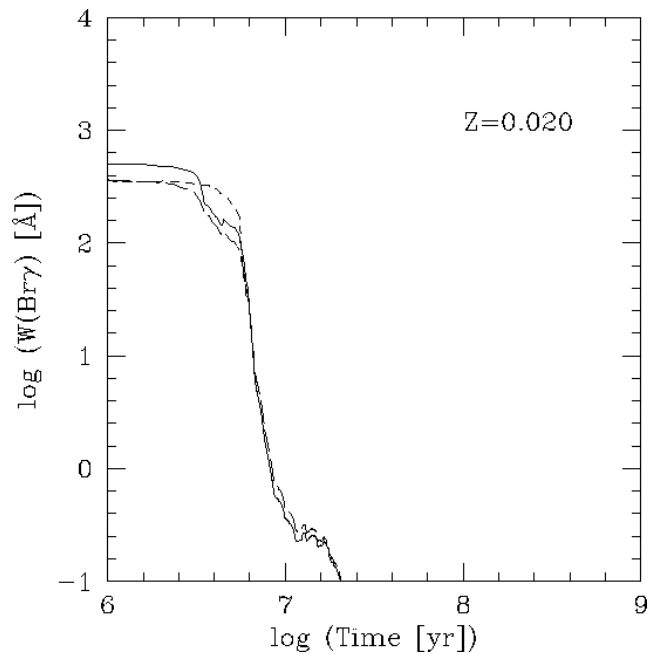


FIG. 89b

FIG. 89.—Br γ equivalent width vs. time. Star formation law: instantaneous; solid line, $\alpha = 2.35$, $M_{\text{up}} = 100 M_{\odot}$; long-dashed line, $\alpha = 3.30$, $M_{\text{up}} = 100 M_{\odot}$; short-dashed line, $\alpha = 2.35$, $M_{\text{up}} = 30 M_{\odot}$; (a) $Z = 0.040$; (b) $Z = 0.020$; (c) $Z = 0.008$; (d) $Z = 0.004$; (e) $Z = 0.001$.

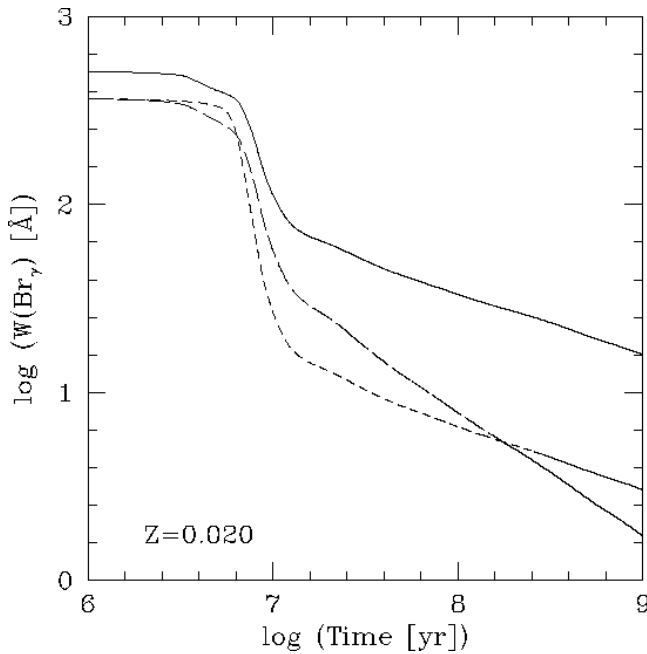


FIG. 90b

FIG. 90.—Br γ equivalent width vs. time. Star formation law: continuous; solid line, $\alpha = 2.35$, $M_{\text{up}} = 100 M_{\odot}$; long-dashed line, $\alpha = 3.30$, $M_{\text{up}} = 100 M_{\odot}$; short-dashed line, $\alpha = 2.35$, $M_{\text{up}} = 30 M_{\odot}$; (a) $Z = 0.040$; (b) $Z = 0.020$; (c) $Z = 0.008$; (d) $Z = 0.004$; (e) $Z = 0.001$.

In Figures 81 and 82 we predicted $N(\text{He}^+)$, which can immediately be converted into the emission-line flux of nebular He II $\lambda 4686$. Generally, a hot-star population capable of producing nebular He II will also show broad, stellar He II $\lambda 4686$ (Schaerer & Vacca 1998). Our model predictions for the stellar line are in Figures 91a–91e and 92a–92e. The feature is commonly referred to as the “WR bump.” It includes only He II and none of the other nearby spectral features like C III, N III, [Ar IV], and [Fe III]. Note that our code predicts other WR lines from the list of Schaerer & Vacca, but they are not given here.

[Fe II] $\lambda 1.26$ is useful to count supernovae in starbursts (Figs. 93a–93e and 94a–94e). The supernova shock wave destroys interstellar dust grains, thereby releasing iron atoms and ions which had condensed on the dust grains. We adopted the scaling relation of Calzetti (1997) to convert the supernova rates into [Fe II] line luminosities.

The remaining figures in this section are related to RSG properties. We repeat again that the predicted properties of post-main-sequence stars are not reliable and that all phases dependent on RSG properties at subsolar metallicity are suspect. We begin with the spectroscopic CO index at $2.2 \mu\text{m}$ (Figs. 95a–95e and 96a–96e). We follow the definition of Doyon, Joseph, & Wright (1994), who expressed the CO strength as a function of temperature for dwarfs, giants, and supergiants. The index is set to 0 for $T_{\text{eff}} > 6000 \text{ K}$. We also computed the strength of the calcium triplet at 8498, 8542, and 8662 Å (Figs. 97a–97e and 98a–98e). The equivalent width of the sum of all three lines is related to gravity ($\log g$) and metallicity by the relation $W(\text{CaT}) = 10.21 - 0.95 \log g + 2.18 \log Z/Z_{\odot}$ (Díaz, Terlevich, & Terlevich 1989; García-Vargas, Mollá, & Bressan 1998). The predicted values neither take into account nebular emission nor stellar absorption of higher Paschen lines which fall in

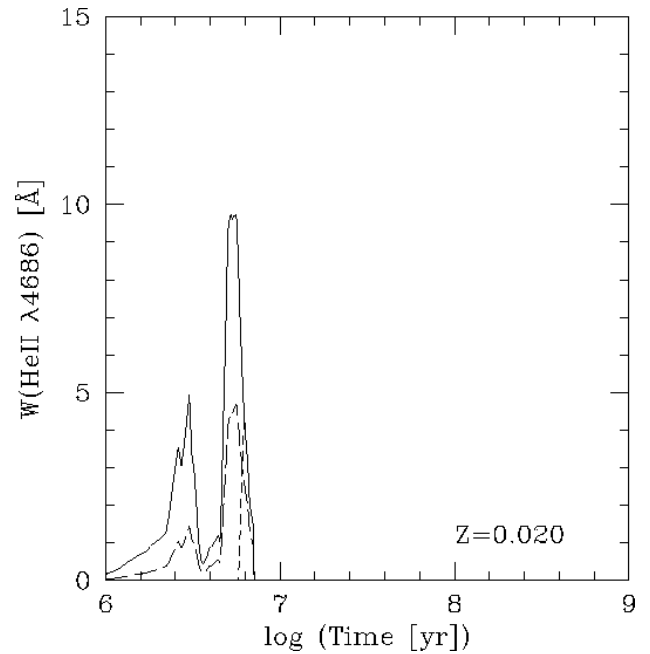


FIG. 91b

FIG. 91.—Equivalent width of stellar He II $\lambda 4686$ vs. time. Star formation law: instantaneous; solid line, $\alpha = 2.35$, $M_{\text{up}} = 100 M_{\odot}$; long-dashed line, $\alpha = 3.30$, $M_{\text{up}} = 100 M_{\odot}$; short-dashed line, $\alpha = 2.35$, $M_{\text{up}} = 30 M_{\odot}$; (a) $Z = 0.040$; (b) $Z = 0.020$; (c) $Z = 0.008$; (d) $Z = 0.004$; (e) $Z = 0.001$.

this wavelength region. Observations must be corrected for these lines, if present, before a comparison is made.

Evolutionary synthesis models for the first and second overtones of CO at 2.29 and $1.62 \mu\text{m}$ and for Si I at $1.59 \mu\text{m}$ were presented by Origlia et al. (1998). The models in

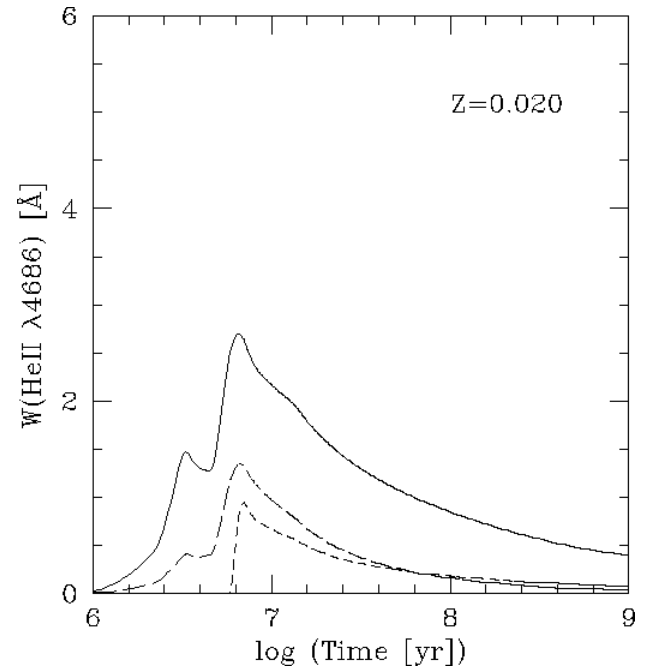


FIG. 92b

FIG. 92.—Equivalent width of stellar He II $\lambda 4686$ vs. time. Star formation law: continuous; solid line, $\alpha = 2.35$, $M_{\text{up}} = 100 M_{\odot}$; long-dashed line, $\alpha = 3.30$, $M_{\text{up}} = 100 M_{\odot}$; short-dashed line, $\alpha = 2.35$, $M_{\text{up}} = 30 M_{\odot}$; (a) $Z = 0.040$; (b) $Z = 0.020$; (c) $Z = 0.008$; (d) $Z = 0.004$; (e) $Z = 0.001$.

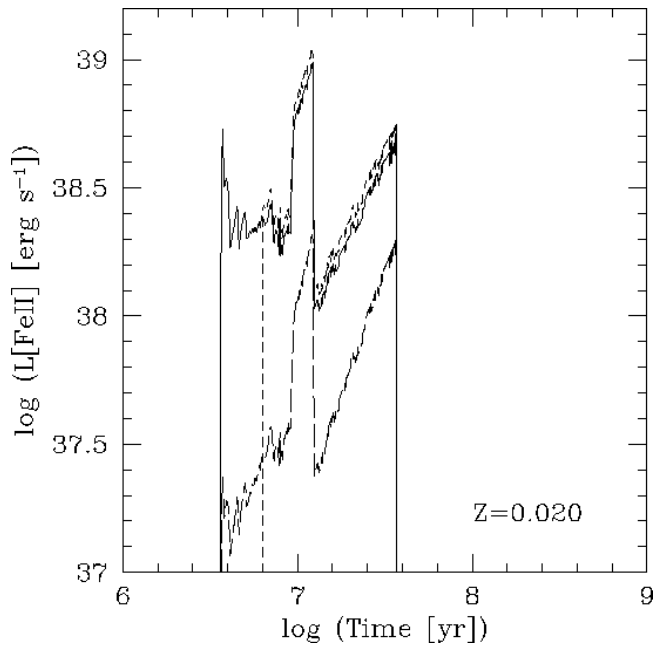


FIG. 93b

FIG. 93.—Luminosity of [Fe II] $\lambda 1.26 \mu\text{m}$ vs. time. Star formation law: instantaneous; solid line, $\alpha = 2.35$, $M_{\text{up}} = 100 M_{\odot}$; long-dashed line, $\alpha = 3.30$, $M_{\text{up}} = 100 M_{\odot}$; short-dashed line, $\alpha = 2.35$, $M_{\text{up}} = 30 M_{\odot}$; (a) $Z = 0.040$; (b) $Z = 0.020$; (c) $Z = 0.008$; (d) $Z = 0.004$; (e) $Z = 0.001$.

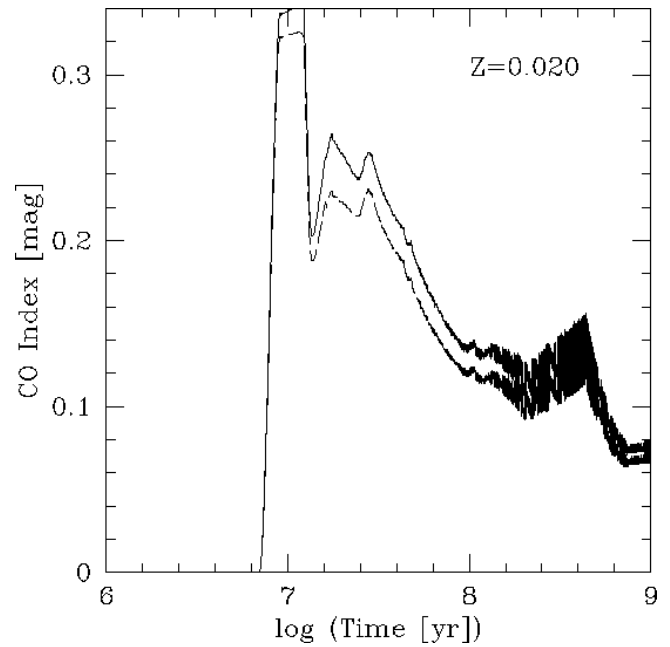


FIG. 95b

FIG. 95.—CO index vs. time. Star formation law: instantaneous; solid line, $\alpha = 2.35$, $M_{\text{up}} = 100 M_{\odot}$; long-dashed line, $\alpha = 3.30$, $M_{\text{up}} = 100 M_{\odot}$; short-dashed line, $\alpha = 2.35$, $M_{\text{up}} = 30 M_{\odot}$; (a) $Z = 0.040$; (b) $Z = 0.020$; (c) $Z = 0.008$; (d) $Z = 0.004$; (e) $Z = 0.001$.

Figures 99a–99e and 100a–100e (CO $\lambda 1.62 \mu\text{m}$), Figures 101a–101e and 102a–102e (CO $\lambda 2.2 \mu\text{m}$), and in Figures 103a–103e and 104a–104e (Si I $\lambda 1.59 \mu\text{m}$) are expanded versions of the *unmodified* case discussed by Origlia et al. In that paper, the effect of modifying the evolutionary tracks

was studied and several sets of IR-line models were published. To be consistent with the other quantities shown here, we opted for including only the standard models. The models for Si I $\lambda 1.59 \mu\text{m}$ were not covered by Origlia et al.

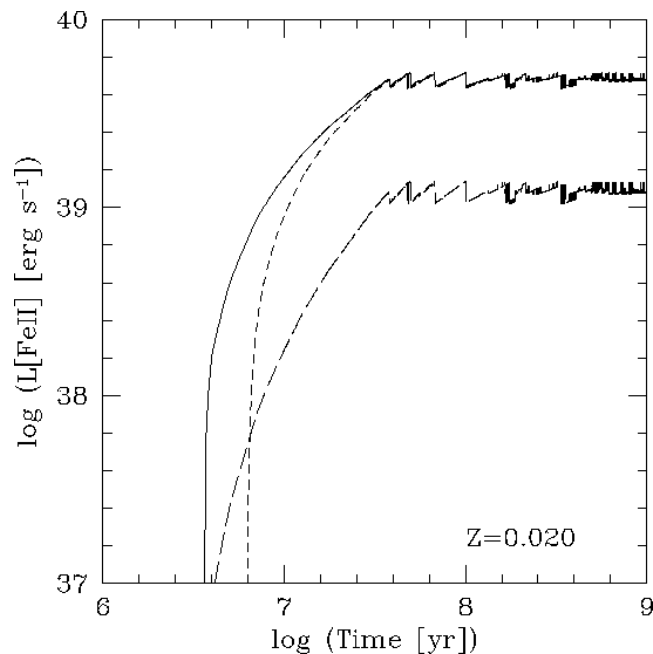


FIG. 94b

FIG. 94.—Luminosity of [Fe II] $\lambda 1.26 \mu\text{m}$ vs. time. Star formation law: continuous; solid line, $\alpha = 2.35$, $M_{\text{up}} = 100 M_{\odot}$; long-dashed line, $\alpha = 3.30$, $M_{\text{up}} = 100 M_{\odot}$; short-dashed line, $\alpha = 2.35$, $M_{\text{up}} = 30 M_{\odot}$; (a) $Z = 0.040$; (b) $Z = 0.020$; (c) $Z = 0.008$; (d) $Z = 0.004$; (e) $Z = 0.001$.

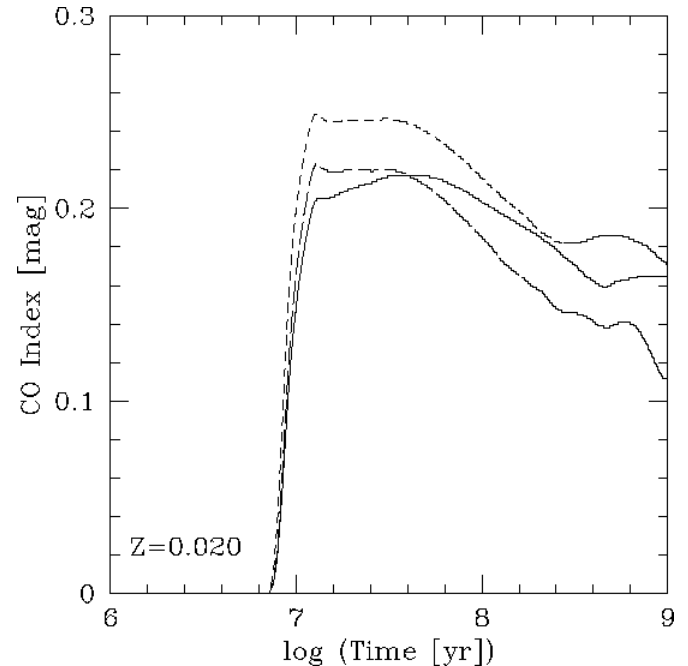


FIG. 96b

FIG. 96.—CO index vs. time. Star formation law: continuous; solid line, $\alpha = 2.35$, $M_{\text{up}} = 100 M_{\odot}$; long-dashed line, $\alpha = 3.30$, $M_{\text{up}} = 100 M_{\odot}$; short-dashed line, $\alpha = 2.35$, $M_{\text{up}} = 30 M_{\odot}$; (a) $Z = 0.040$; (b) $Z = 0.020$; (c) $Z = 0.008$; (d) $Z = 0.004$; (e) $Z = 0.001$.

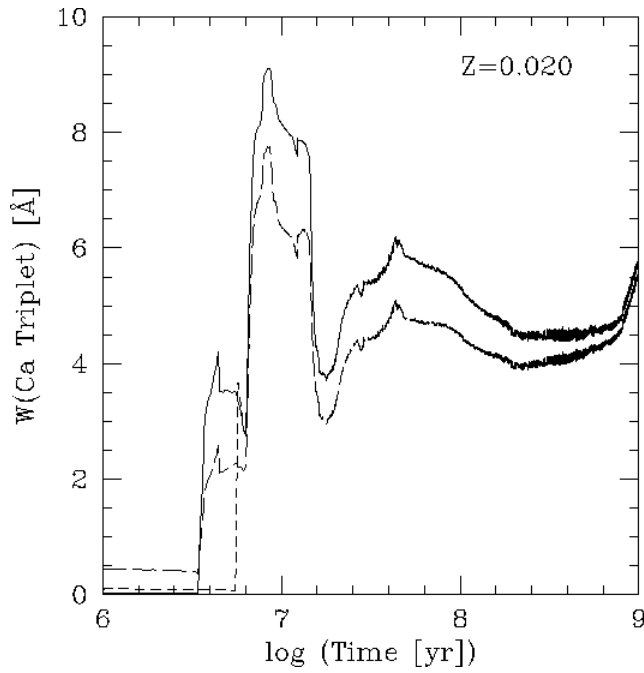


FIG. 97b

FIG. 97.—Calcium triplet equivalent width vs. time. Star formation law: instantaneous; solid line, $\alpha = 2.35$, $M_{\text{up}} = 100 M_{\odot}$; long-dashed line, $\alpha = 3.30$, $M_{\text{up}} = 100 M_{\odot}$; short-dashed line, $\alpha = 2.35$, $M_{\text{up}} = 30 M_{\odot}$; (a) $Z = 0.040$; (b) $Z = 0.020$; (c) $Z = 0.008$; (d) $Z = 0.004$; (e) $Z = 0.001$.

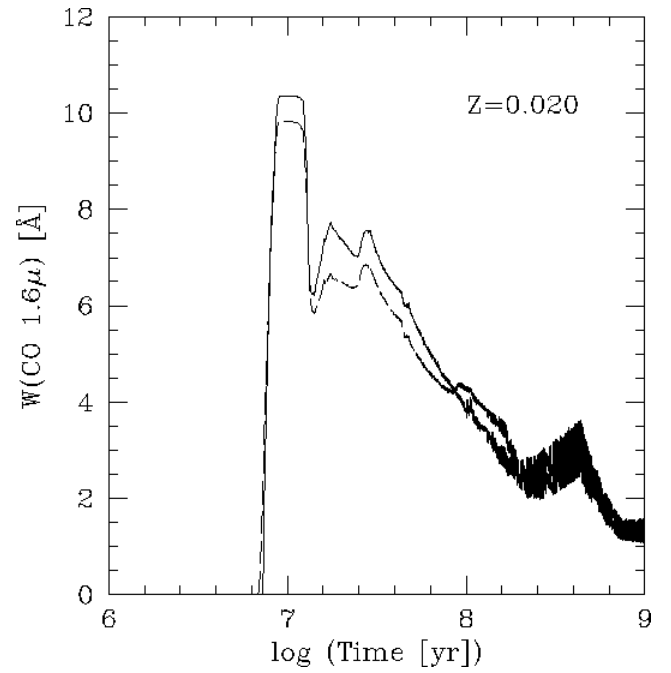


FIG. 99b

FIG. 99.—Equivalent width of CO $\lambda 1.62 \mu\text{m}$ vs. time. Star formation law: instantaneous; solid line, $\alpha = 2.35$, $M_{\text{up}} = 100 M_{\odot}$; long-dashed line, $\alpha = 3.30$, $M_{\text{up}} = 100 M_{\odot}$; short-dashed line, $\alpha = 2.35$, $M_{\text{up}} = 30 M_{\odot}$; (a) $Z = 0.040$; (b) $Z = 0.020$; (c) $Z = 0.008$; (d) $Z = 0.004$; (e) $Z = 0.001$.

and are shown here for the first time. The theoretical library of Origlia et al. (1993) which was used for Si I is less reliable than that for CO so that care is required when using the Si I models.

10. MASS AND ENERGY RETURN

The previous sections cover stellar numbers and radiative properties. Here we turn to nonradiative properties of the stellar population. The input physics is discussed in greater

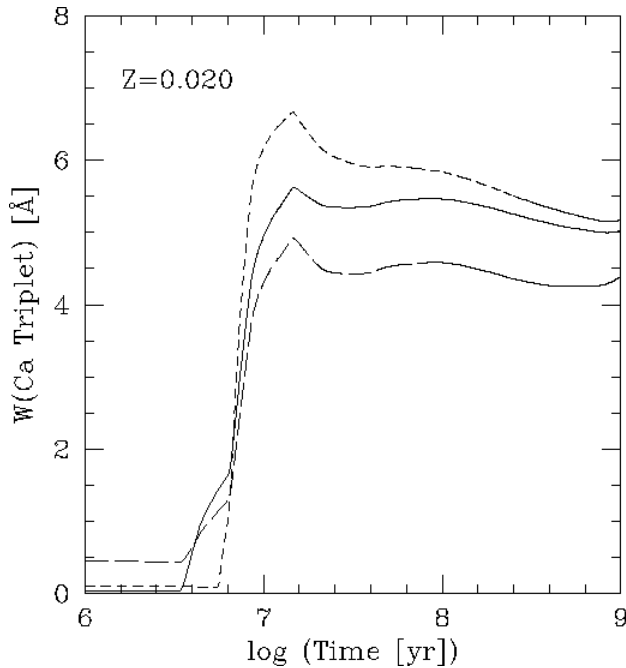


FIG. 98b

FIG. 98.—Calcium triplet equivalent width vs. time. Star formation law: continuous; solid line, $\alpha = 2.35$, $M_{\text{up}} = 100 M_{\odot}$; long-dashed line, $\alpha = 3.30$, $M_{\text{up}} = 100 M_{\odot}$; short-dashed line, $\alpha = 2.35$, $M_{\text{up}} = 30 M_{\odot}$; (a) $Z = 0.040$; (b) $Z = 0.020$; (c) $Z = 0.008$; (d) $Z = 0.004$; (e) $Z = 0.001$.

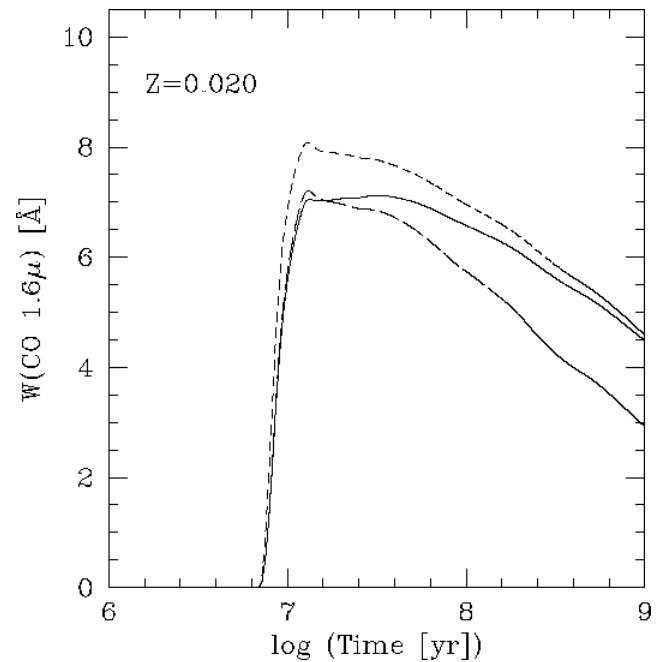


FIG. 100b

FIG. 100.—Equivalent width of CO $\lambda 1.62 \mu\text{m}$ vs. time. Star formation law: continuous; solid line, $\alpha = 2.35$, $M_{\text{up}} = 100 M_{\odot}$; long-dashed line, $\alpha = 3.30$, $M_{\text{up}} = 100 M_{\odot}$; short-dashed line, $\alpha = 2.35$, $M_{\text{up}} = 30 M_{\odot}$; (a) $Z = 0.040$; (b) $Z = 0.020$; (c) $Z = 0.008$; (d) $Z = 0.004$; (e) $Z = 0.001$.

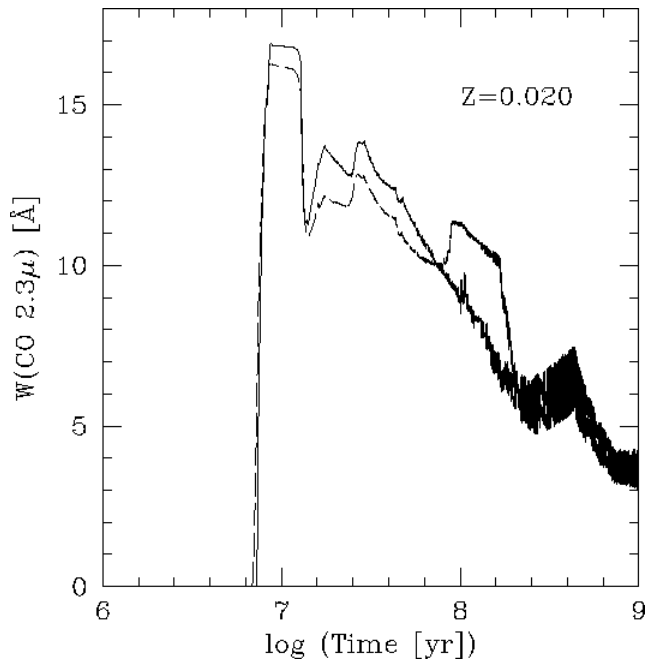


FIG. 101b

FIG. 101.—Equivalent width of CO $\lambda 2.29 \mu\text{m}$ vs. time. Star formation law: instantaneous; solid line, $\alpha = 2.35$, $M_{\text{up}} = 100 M_{\odot}$; long-dashed line, $\alpha = 3.30$, $M_{\text{up}} = 100 M_{\odot}$; short-dashed line, $\alpha = 2.35$, $M_{\text{up}} = 30 M_{\odot}$; (a) $Z = 0.040$; (b) $Z = 0.020$; (c) $Z = 0.008$; (d) $Z = 0.004$; (e) $Z = 0.001$.

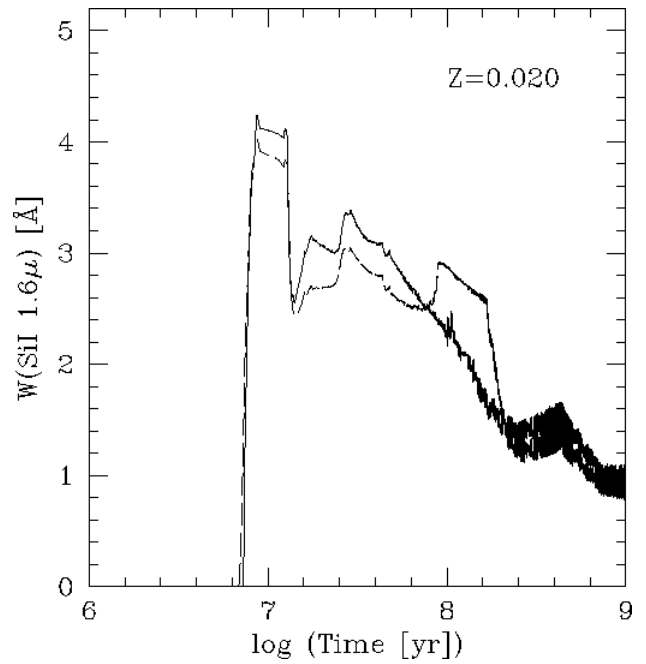


FIG. 103b

FIG. 103.—Equivalent width of Si I $\lambda 1.59 \mu\text{m}$ vs. time. Star formation law: instantaneous; solid line, $\alpha = 2.35$, $M_{\text{up}} = 100 M_{\odot}$; long-dashed line, $\alpha = 3.30$, $M_{\text{up}} = 100 M_{\odot}$; short-dashed line, $\alpha = 2.35$, $M_{\text{up}} = 30 M_{\odot}$; (a) $Z = 0.040$; (b) $Z = 0.020$; (c) $Z = 0.008$; (d) $Z = 0.004$; (e) $Z = 0.001$.

detail in Leitherer, Robert, & Drissen (1992). The figures in this section show the mass and energy input by stars and SNe. Only core-collapse SNe are considered. They are assumed to release 10^{51} ergs per event in the form of kinetic

energy, independent of metallicity. We do not address the efficiency of thermalization which would require hydrodynamical modeling. The simulations of Thornton et al. (1998) suggest that about 10% of the available kinetic energy can

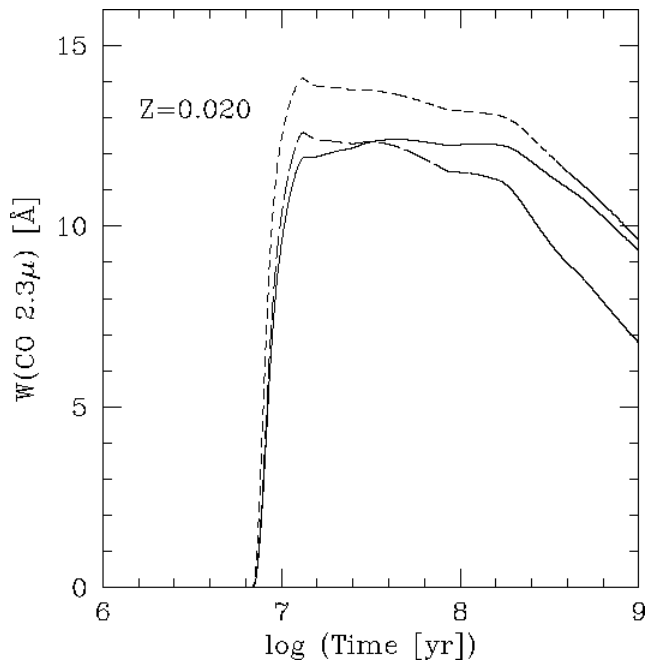


FIG. 102b

FIG. 102.—Equivalent width of CO $\lambda 2.29 \mu\text{m}$ vs. time. Star formation law: continuous; solid line, $\alpha = 2.35$, $M_{\text{up}} = 100 M_{\odot}$; long-dashed line, $\alpha = 3.30$, $M_{\text{up}} = 100 M_{\odot}$; short-dashed line, $\alpha = 2.35$, $M_{\text{up}} = 30 M_{\odot}$; (a) $Z = 0.040$; (b) $Z = 0.020$; (c) $Z = 0.008$; (d) $Z = 0.004$; (e) $Z = 0.001$.

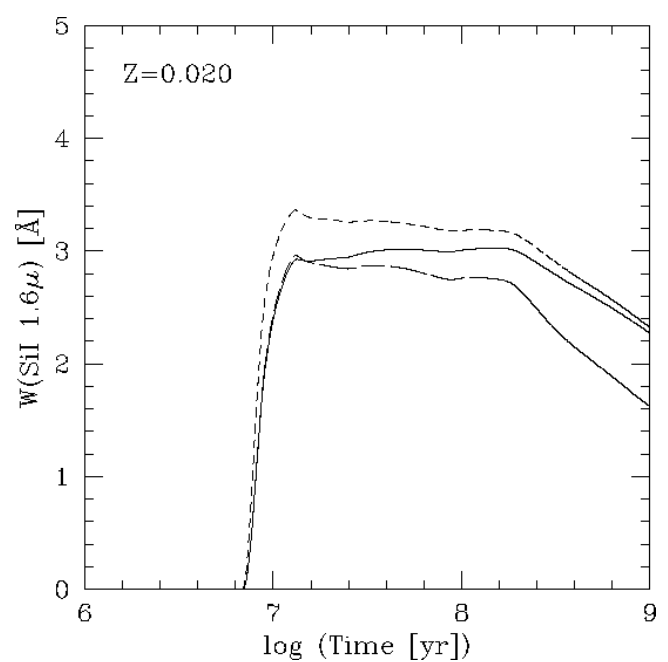


FIG. 104b

FIG. 104.—Equivalent width of Si I $\lambda 1.59 \mu\text{m}$ vs. time. Star formation law: continuous; solid line, $\alpha = 2.35$, $M_{\text{up}} = 100 M_{\odot}$; long-dashed line, $\alpha = 3.30$, $M_{\text{up}} = 100 M_{\odot}$; short-dashed line, $\alpha = 2.35$, $M_{\text{up}} = 30 M_{\odot}$; (a) $Z = 0.040$; (b) $Z = 0.020$; (c) $Z = 0.008$; (d) $Z = 0.004$; (e) $Z = 0.001$.

actually be used to pressurize the interstellar gas. The remaining 90% are radiated away.

The rate of mass return of stellar-wind and SN material is plotted in Figures 105a–105e and 106a–106e. The adopted mass-loss rates are *not* those of the evolutionary models but

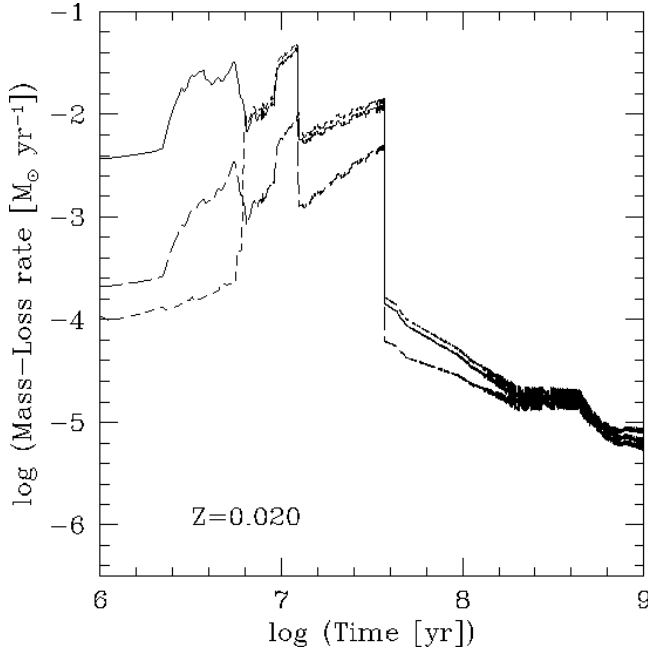


FIG. 105b

FIG. 105.—Mass-loss rate (stellar winds and SNe) vs. time. Star formation law: instantaneous; solid line, $\alpha = 2.35$, $M_{\text{up}} = 100 M_{\odot}$; long-dashed line, $\alpha = 3.30$, $M_{\text{up}} = 100 M_{\odot}$; short-dashed line, $\alpha = 2.35$, $M_{\text{up}} = 30 M_{\odot}$; (a) $Z = 0.040$; (b) $Z = 0.020$; (c) $Z = 0.008$; (d) $Z = 0.004$; (e) $Z = 0.001$.

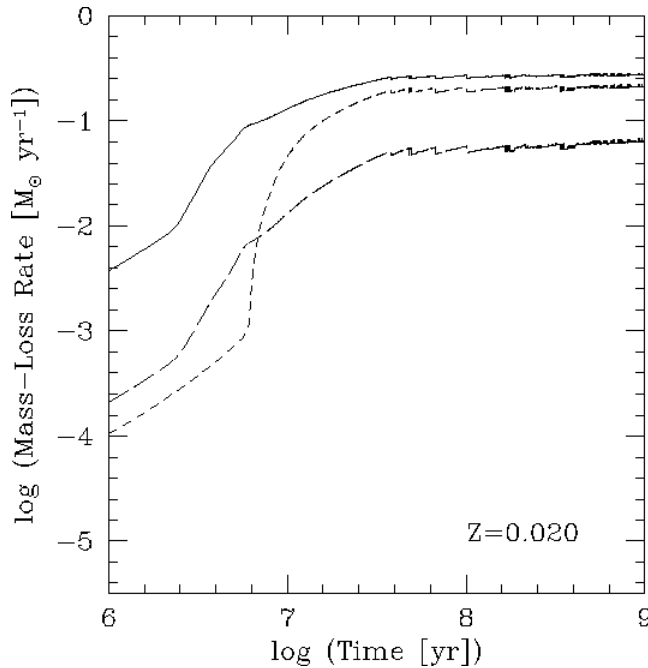


FIG. 106b

FIG. 106.—Mass-loss rate (stellar winds and SNe) vs. time. Star formation law: continuous; solid line, $\alpha = 2.35$, $M_{\text{up}} = 100 M_{\odot}$; long-dashed line, $\alpha = 3.30$, $M_{\text{up}} = 100 M_{\odot}$; short-dashed line, $\alpha = 2.35$, $M_{\text{up}} = 30 M_{\odot}$; (a) $Z = 0.040$; (b) $Z = 0.020$; (c) $Z = 0.008$; (d) $Z = 0.004$; (e) $Z = 0.001$.

those favored by Leitherer et al. (1992) and LH95. We prefer this approach over simply using the evolutionary mass-loss rates. In our opinion, the evolutionary mass-loss rates are too high (see § 2) and should be considered only as an adjustable parameter in evolution models but are not directly related to the observed mass-loss rate. Slight differences between Figures 105 and 106 and the corresponding figures in LH95 are not due to a different mass-loss parameterization but because of different stellar parameters (T_{eff} , L) in the revised tracks. The individual contributions from stellar winds and SNe are broken down in Figures 107a–107e and 108a–108e for the standard IMF case. Stellar winds are generally more important for young bursts, whereas SNe take over at later times.

The total mass return from winds and SNe is in Figures 109a–109e and 110a–110e. The quantity plotted is $\int \dot{M} dt$, i.e., the integral of the curves in Figures 107 and 108 over time. This quantity is useful to evaluate the exhaustion of the gas supply in a galaxy or the degree of chemical pollution by wind and supernova material.

Figures 111a–111e and 112a–112e give the mechanical luminosity L_{mech} released by winds and supernovae. The curves are similar to those for the mass return in Figures 105 and 106. The relative contributions to L_{mech} from stellar winds and SNe are in Figures 113a–113e and 114a–114e. A further breakdown into individual stellar-wind components is given in Leitherer et al. (1992). Generally, most of the wind power comes from WR stars, with some contribution from O stars. All other stellar phases are negligible since wind velocities of cool stars are lower by 2 orders of magnitude. The energy return ($\int L_{\text{mech}} dt$) from winds and SNe is in Figures 115a–115e and 116a–116e.

It is instructive to perform a differential comparison between the radiative and the nonradiative energy output of

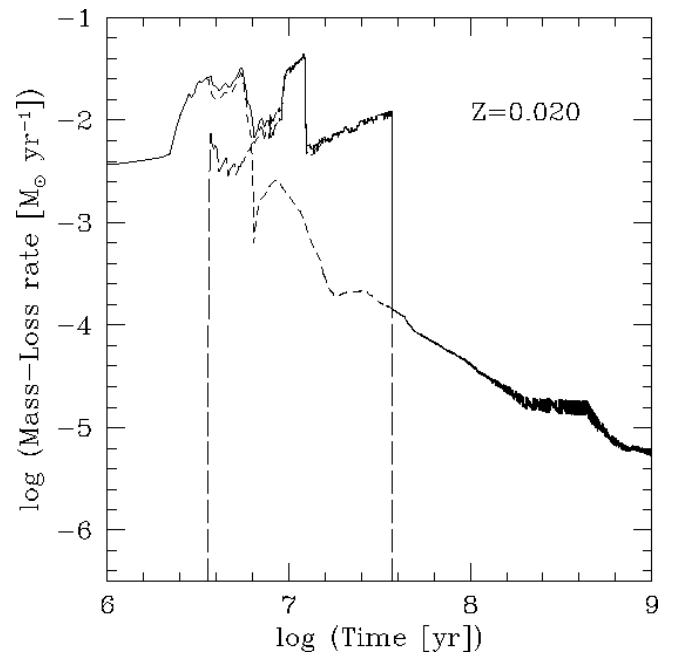


FIG. 107b

FIG. 107.—Mass-loss rate vs. time. Star formation law: instantaneous; IMF: $\alpha = 2.35$, $M_{\text{up}} = 100 M_{\odot}$; solid line, total; long-dashed line, supernovae; short-dashed line, stellar winds; (a) $Z = 0.040$; (b) $Z = 0.020$; (c) $Z = 0.008$; (d) $Z = 0.004$; (e) $Z = 0.001$.

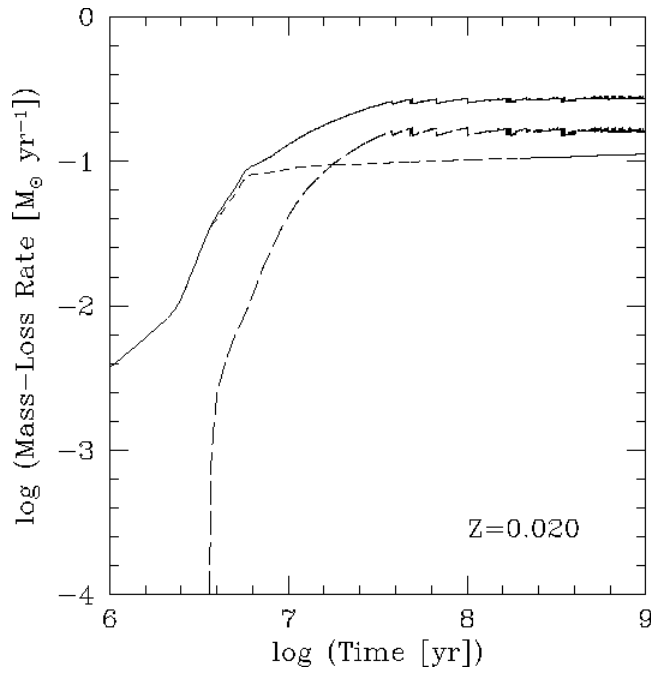


FIG. 108b

FIG. 108.—Mass-loss rate vs. time. Star formation law: continuous; IMF: $\alpha = 2.35$, $M_{\text{up}} = 100 M_{\odot}$; solid line, total; long-dashed line, supernovae; short-dashed line, stellar winds; (a) $Z = 0.040$; (b) $Z = 0.020$; (c) $Z = 0.008$; (d) $Z = 0.004$; (e) $Z = 0.001$.

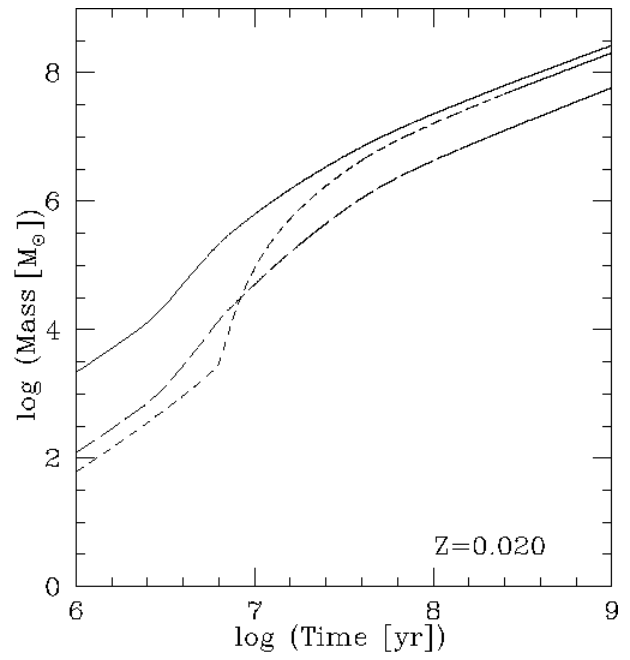


FIG. 110b

FIG. 110.—Mass loss (stellar winds and SNe) vs. time. Star formation law: continuous; solid line, $\alpha = 2.35$, $M_{\text{up}} = 100 M_{\odot}$; long-dashed line, $\alpha = 3.30$, $M_{\text{up}} = 100 M_{\odot}$; short-dashed line, $\alpha = 2.35$, $M_{\text{up}} = 30 M_{\odot}$; (a) $Z = 0.040$; (b) $Z = 0.020$; (c) $Z = 0.008$; (d) $Z = 0.004$; (e) $Z = 0.001$.

young stellar populations. This is done in Figures 117a–117e and 118a–118e for the ratio of the ionizing ($<912 \text{ \AA}$) over the bolometric luminosity and in Figures 119a–119e and 120a–120e for the ratio of the mechanical (L_{mech}) over

the bolometric luminosity. The nonradiative energy input into the interstellar medium becomes significant in comparison with ionizing radiation once the strong WR winds are turned on. For a single population, nonthermal and

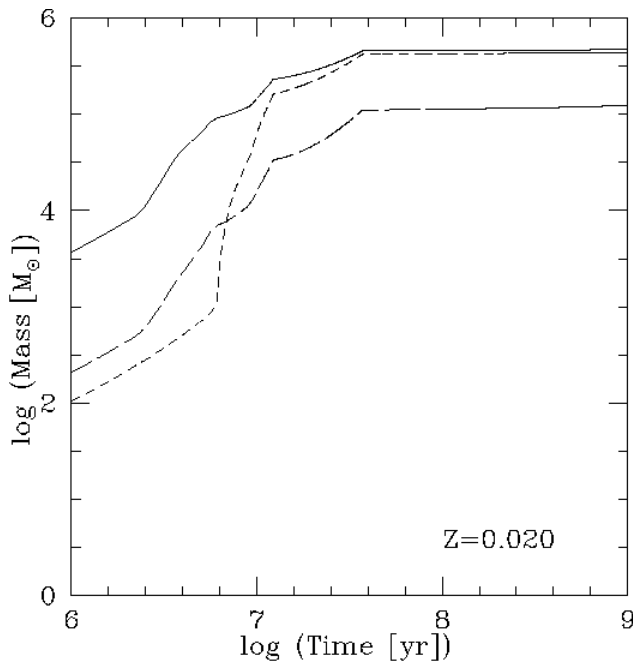


FIG. 109b

FIG. 109.—Mass loss (stellar winds and SNe) vs. time. Star formation law: instantaneous; solid line, $\alpha = 2.35$, $M_{\text{up}} = 100 M_{\odot}$; long-dashed line, $\alpha = 3.30$, $M_{\text{up}} = 100 M_{\odot}$; short-dashed line, $\alpha = 2.35$, $M_{\text{up}} = 30 M_{\odot}$; (a) $Z = 0.040$; (b) $Z = 0.020$; (c) $Z = 0.008$; (d) $Z = 0.004$; (e) $Z = 0.001$.

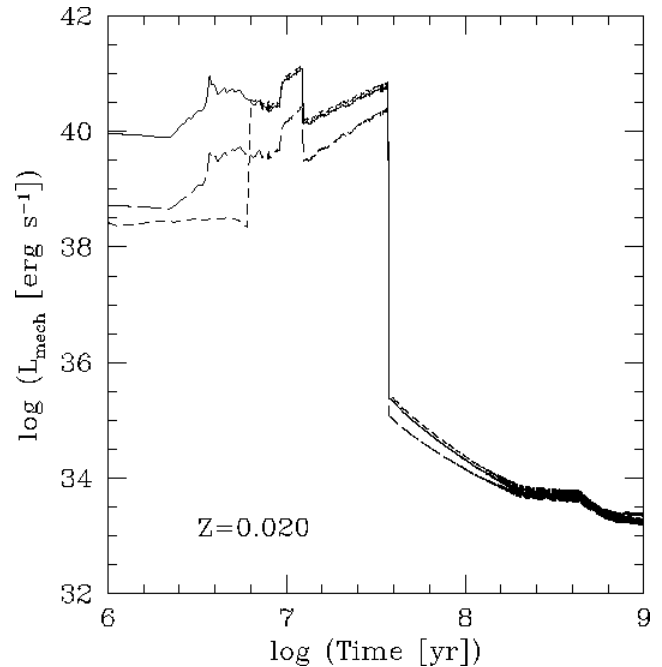


FIG. 111b

FIG. 111.—Mechanical luminosity (stellar winds and SNe) vs. time. Star formation law: instantaneous; solid line, $\alpha = 2.35$, $M_{\text{up}} = 100 M_{\odot}$; long-dashed line, $\alpha = 3.30$, $M_{\text{up}} = 100 M_{\odot}$; short-dashed line, $\alpha = 2.35$, $M_{\text{up}} = 30 M_{\odot}$; (a) $Z = 0.040$; (b) $Z = 0.020$; (c) $Z = 0.008$; (d) $Z = 0.004$; (e) $Z = 0.001$.

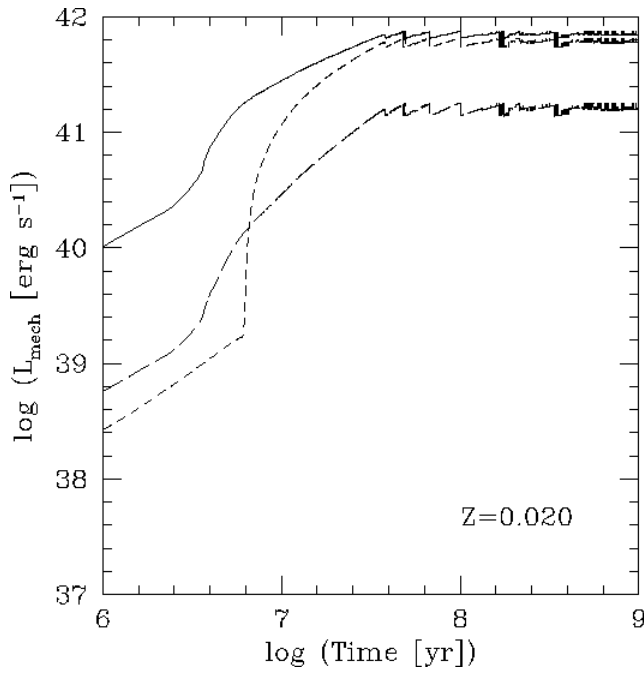


FIG. 112b

FIG. 112.—Mechanical luminosity (stellar winds and SNe) vs. time. Star formation law: continuous; IMF: $\alpha = 2.35$, $M_{\text{up}} = 100 M_{\odot}$; long-dashed line, $\alpha = 3.30$, $M_{\text{up}} = 100 M_{\odot}$; short-dashed line, $\alpha = 2.35$, $M_{\text{up}} = 30 M_{\odot}$; (a) $Z = 0.040$; (b) $Z = 0.020$; (c) $Z = 0.008$; (d) $Z = 0.004$; (e) $Z = 0.001$.

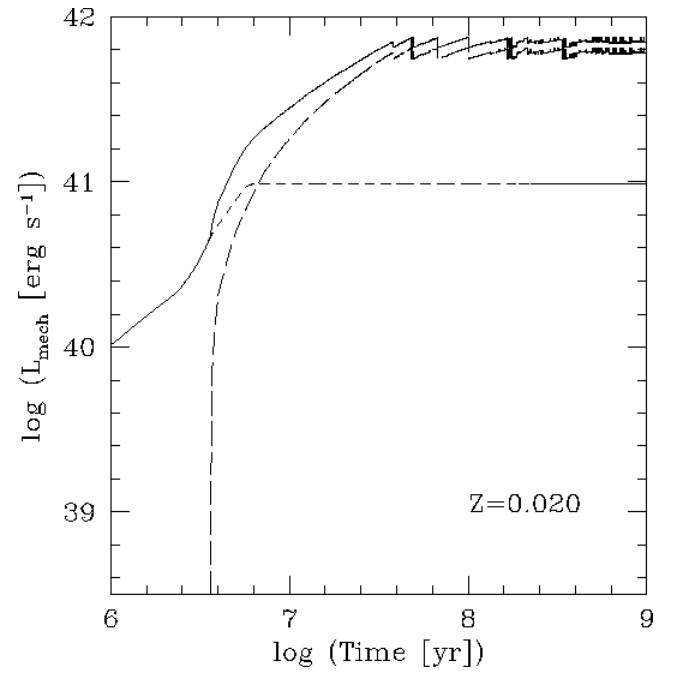


FIG. 114b

FIG. 114.—Mechanical luminosity vs. time. Star formation law: continuous; IMF: $\alpha = 2.35$, $M_{\text{up}} = 100 M_{\odot}$; solid line, total; long-dashed line, supernovae; short-dashed line, stellar winds; (a) $Z = 0.040$; (b) $Z = 0.020$; (c) $Z = 0.008$; (d) $Z = 0.004$; (e) $Z = 0.001$.

ionizing energy input become equally important around ~ 10 Myr.

11. CONCLUSIONS

We have computed a large grid of predictions for observ-

able properties of galaxies with active star formation. The distribution of the models is purely Web-based. We believe the community will find this method more useful than a printed publication. All the figures discussed in this paper can be found in the electronic edition of the Astrophysical

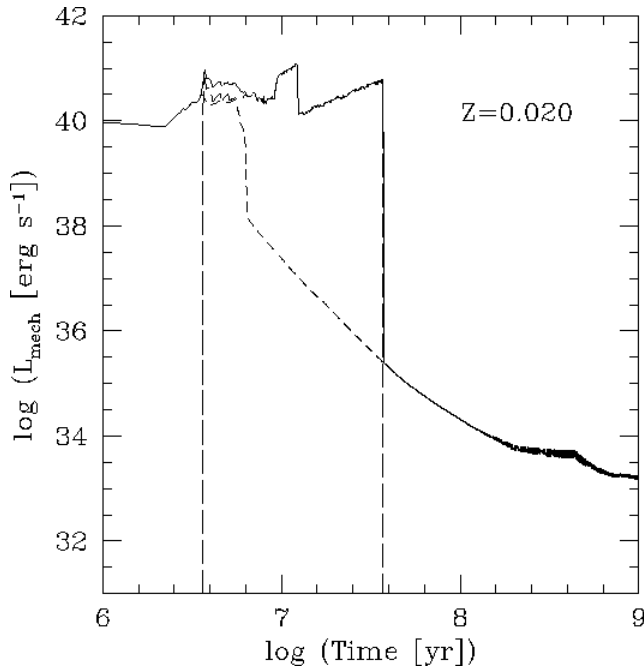


FIG. 113b

FIG. 113.—Mechanical luminosity vs. time. Star formation law: instantaneous; IMF: $\alpha = 2.35$, $M_{\text{up}} = 100 M_{\odot}$; solid line, total; long-dashed line, supernovae; short-dashed line, stellar winds; (a) $Z = 0.040$; (b) $Z = 0.020$; (c) $Z = 0.008$; (d) $Z = 0.004$; (e) $Z = 0.001$.

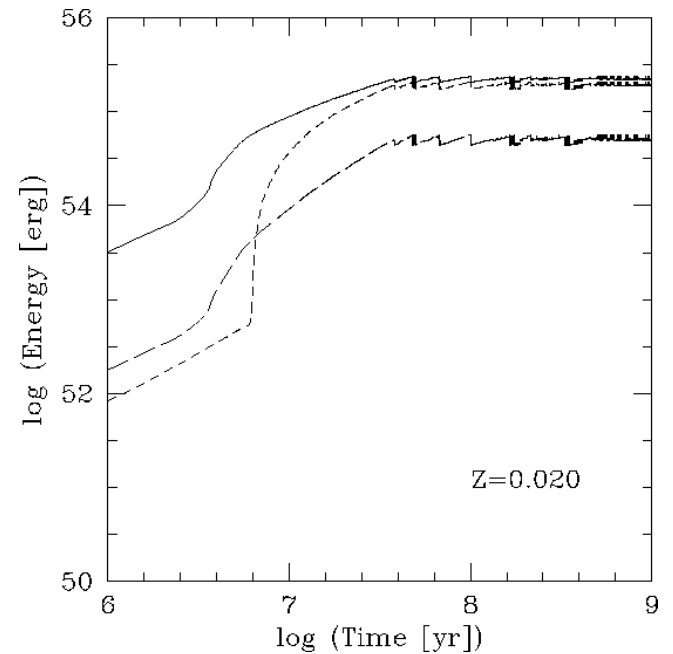


FIG. 115b

FIG. 115.—Energy input (stellar winds and SNe) vs. time. Star formation law: instantaneous; IMF: $\alpha = 2.35$, $M_{\text{up}} = 100 M_{\odot}$; solid line, total; long-dashed line, $\alpha = 3.30$, $M_{\text{up}} = 100 M_{\odot}$; short-dashed line, $\alpha = 2.35$, $M_{\text{up}} = 30 M_{\odot}$; (a) $Z = 0.040$; (b) $Z = 0.020$; (c) $Z = 0.008$; (d) $Z = 0.004$; (e) $Z = 0.001$.

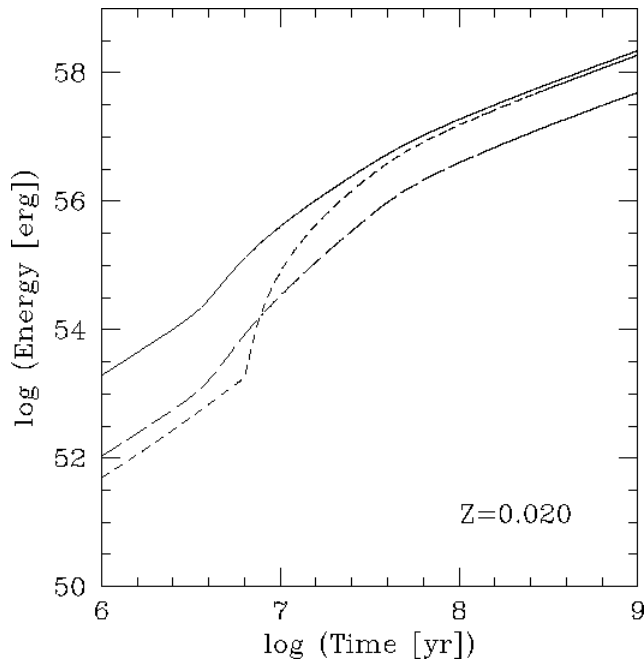


FIG. 116b

FIG. 116.—Energy input (stellar winds and SNe) vs. time. Star formation law: continuous; solid line, $\alpha = 2.35$, $M_{\text{up}} = 100 M_{\odot}$; long-dashed line, $\alpha = 3.30$, $M_{\text{up}} = 100 M_{\odot}$; short-dashed line, $\alpha = 2.35$, $M_{\text{up}} = 30 M_{\odot}$; (a) $Z = 0.040$; (b) $Z = 0.020$; (c) $Z = 0.008$; (d) $Z = 0.004$; (e) $Z = 0.001$.

Journal and also at <http://www.stsci.edu/science/starburst99/>. This Web page provides links to other spectrophotometric databases as well.

It is worthwhile to recall the most important shortcomings and uncertainties of the models:

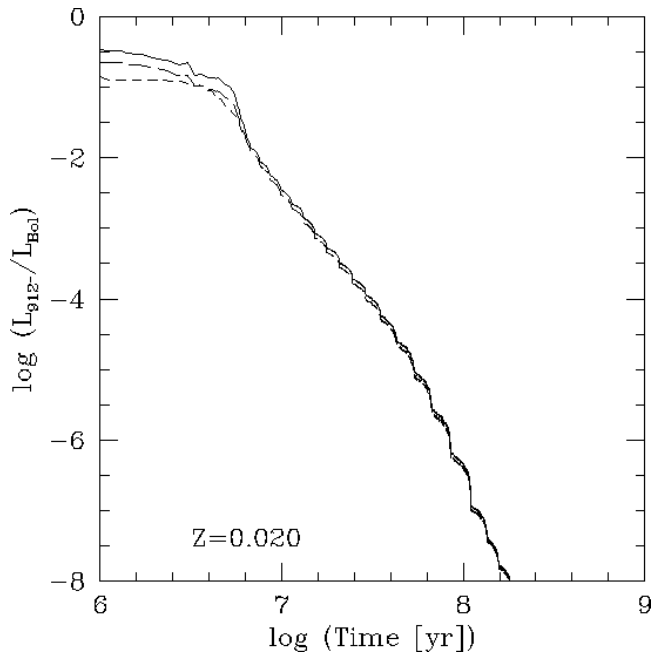


FIG. 117b

FIG. 117.—Ratio of ionizing over bolometric luminosity vs. time. Star formation law: instantaneous; solid line, $\alpha = 2.35$, $M_{\text{up}} = 100 M_{\odot}$; long-dashed line, $\alpha = 3.30$, $M_{\text{up}} = 100 M_{\odot}$; short-dashed line, $\alpha = 2.35$, $M_{\text{up}} = 30 M_{\odot}$; (a) $Z = 0.040$; (b) $Z = 0.020$; (c) $Z = 0.008$; (d) $Z = 0.004$; (e) $Z = 0.001$.

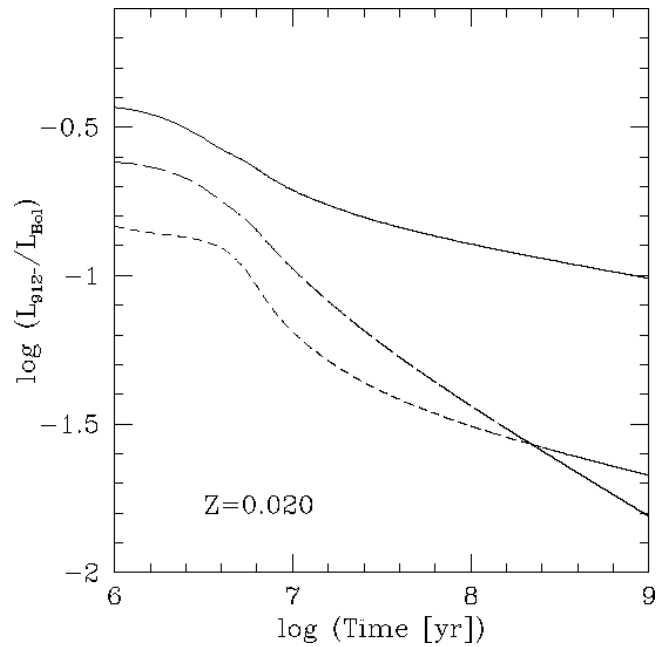


FIG. 118b

FIG. 118.—Ratio of ionizing over bolometric luminosity vs. time. Star formation law: continuous; solid line, $\alpha = 2.35$, $M_{\text{up}} = 100 M_{\odot}$; long-dashed line, $\alpha = 3.30$, $M_{\text{up}} = 100 M_{\odot}$; short-dashed line, $\alpha = 2.35$, $M_{\text{up}} = 30 M_{\odot}$; (a) $Z = 0.040$; (b) $Z = 0.020$; (c) $Z = 0.008$; (d) $Z = 0.004$; (e) $Z = 0.001$.

Chemical evolution is not treated self-consistently. Each stellar generation has the same chemical composition. This becomes a concern for models which are evolved over times during which significant changes in the metallicity of the

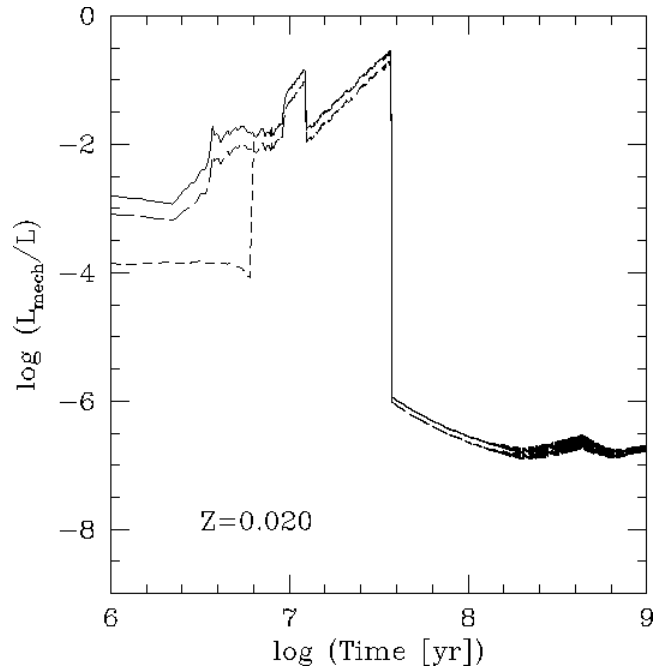


FIG. 119b

FIG. 119.—Ratio of mechanical over bolometric luminosity vs. time. Star formation law: instantaneous; solid line, $\alpha = 2.35$, $M_{\text{up}} = 100 M_{\odot}$; long-dashed line, $\alpha = 3.30$, $M_{\text{up}} = 100 M_{\odot}$; short-dashed line, $\alpha = 2.35$, $M_{\text{up}} = 30 M_{\odot}$; (a) $Z = 0.040$; (b) $Z = 0.020$; (c) $Z = 0.008$; (d) $Z = 0.004$; (e) $Z = 0.001$.

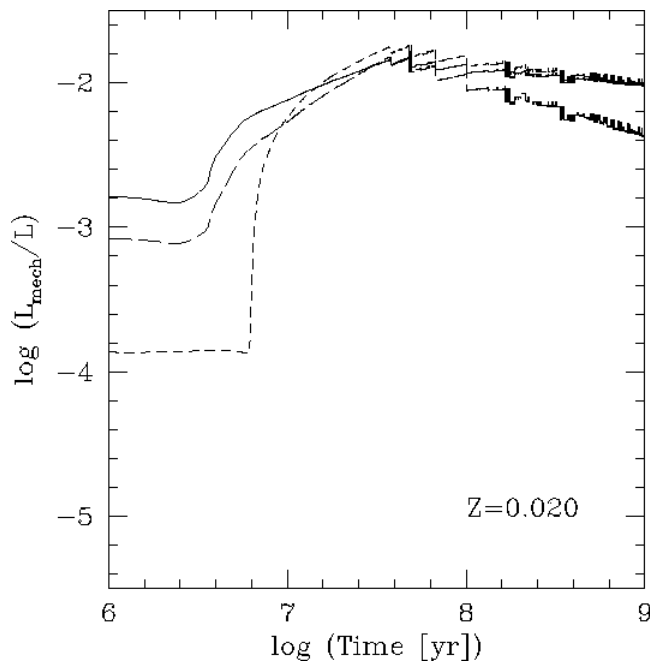


FIG. 120b

FIG. 120.—Ratio of mechanical over bolometric luminosity vs. time. Star formation law: continuous; solid line, $\alpha = 2.35$, $M_{\text{up}} = 100 M_{\odot}$; long-dashed line, $\alpha = 3.30$, $M_{\text{up}} = 100 M_{\odot}$; short-dashed line, $\alpha = 2.35$, $M_{\text{up}} = 30 M_{\odot}$; (a) $Z = 0.040$; (b) $Z = 0.020$; (c) $Z = 0.008$; (d) $Z = 0.004$; (e) $Z = 0.001$.

ISM occur. In this case spectra will have a wavelength-dependent metallicity. Generally, light at shorter wavelengths is produced by more massive and younger stars, which are chemically more evolved than older stars.

Binary evolution has been neglected. Although about 50% of all stars form in binaries, it is not clear if a significant fraction of these binaries has an evolutionary history that differs substantially from single-star evolution. There is disagreement in the literature on this point. Under these circumstances we took the approach of implementing the simpler of the two alternatives, as nature itself often prefers to do.

Mass loss and mixing processes in stellar evolution are still poorly understood. Stellar phases, like WR stars or

RSGs, are particularly affected by such uncertainties. The main culprit is the lack of a self-consistent theory, which makes the introduction of adjustable parameters necessary. These parameters then are sometimes extrapolated into a regime for which they were not calibrated, such as metallicity.

The situation is particularly disturbing for *red supergiants*, whose properties are badly reproduced at low metallicity. There is no easy work-around for the user of evolutionary models, except for an empirical adjustment of the tracks. We have discussed such an adjusted model set. Clearly, a strong effort on the stellar evolution modeling side is called upon for improvements.

Our models put most of the emphasis on early evolution phases. *Later phases*, like AGB stars or white dwarfs, are covered only crudely or not at all. While improvements to our code can be made, our prime goal and expertise is related to massive, hot stars, and we decided to optimize this stellar species first.

Despite the warnings, the model set should turn out to be useful for the interpretation of observations of star-forming galaxies. For maximum benefit, the user is encouraged to compare our model predictions with those of other groups, such as those mentioned earlier in the paper.

To provide maximum flexibility, we offer the user to run tailored models at our Web site. Instructions on how to run the code and how to access the results are given at the Web site. The FORTRAN code is distributed freely and can be retrieved from the Web site as well.

Harry Payne helped us trouble-shoot numerous bugs and pitfalls we encountered during the construction of our Web page. D. F. K. acknowledges financial support from the STScI Summer Student Program. Salary support for D. D. and D. S. came from the STScI Director's Discretionary Research Fund. We appreciate advice on electronic publishing and data maintenance from Bob Hanisch. Partial support for this work was provided by NASA through grant number NAG 5-6903, from the Space Telescope Science Institute, which is operated by the Association of Universities for Research in Astronomy, Inc., under NASA contract NAS 5-26555.

REFERENCES

- Calzetti, D. 1997, *AJ*, 113, 162
 Calzetti, D., & Heckman, T. M. 1999, *ApJ*, 519, in press
 Calzetti, D., Kinney, A. L., & Storchi-Bergmann, T. 1994, *ApJ*, 429, 582
 Carico, D. P., Sanders, D. B., Soifer, B. T., Elias, J. H., Mathews, K., & Neugebauer, G. 1988, *AJ*, 95, 356
 Cassinelli, J. P., et al. 1995, *ApJ*, 438, 932
 Cerviño, M., & Mas-Hesse, J. M. 1994, *A&A*, 284, 749
 Cerviño, M., Mas-Hesse, J. M., & Kunth, D. 1997, in *Starburst Activity in Galaxies*, ed. J. Franco, R. Terlevich, & A. Serrano (Rev. Mexicana Astron. Astrofis. Conf. Ser. 6), 188
 Charbonnel, D., Meynet, G., Maeder, A., Schaller, G., & Schaerer, D. 1993, *A&AS*, 101, 415
 Charlot, S., & Bruzual G. A. 1991, *ApJ*, 367, 126
 Conti, P. S. 1991, *ApJ*, 377, 115
 Conti, P. S., Leep, E. M., & Perry, D. N. 1983, *ApJ*, 268, 228
 Diaz, A. I., Terlevich, E., & Terlevich, R. 1989, *MNRAS*, 239, 325
 Dionne, D. 1999, in *IAU Symp. 193, Wolf-Rayet Phenomena in Massive Stars and Starburst Galaxies*, ed. K. A. van der Hucht, G. Koenigsberger, & P. R. J. Eenens (San Francisco: ASP), in press
 Doyon, R., Joseph, R. D., & Wright, G. S. 1994, *ApJ*, 421, 101
 Ferland, G. J. 1980, *PASP*, 92, 596
 Fioc, M., & Rocca-Volmerange, B. 1997, *A&A*, 326, 950
 García-Vargas, M. L. 1996, in *From Stars to Galaxies: The Impact of Stellar Physics on Galaxy Evolution*, ed. C. Leitherer, U. Fritze-von Alvensleben, & J. Huchra (San Francisco: ASP), 244
 García-Vargas, M. L., Mollá, M., & Bressan, A. 1998, *A&AS*, 130, 513
 Girardi, L., & Bertelli, G. 1998, *MNRAS*, 300, 533
 González Delgado, R. M., Leitherer, C., & Heckman, T. M. 1997, *ApJ*, 489, 601
 Johnson, H. L. 1966, *ARA&A*, 4, 193
 Kurucz, R. L. 1992, in *IAU Symp. 149, The Stellar Populations of Galaxies*, ed. B. Barbuy & A. Renzini (Dordrecht: Kluwer), 225
 Langer, N., & Maeder, A. 1995, *A&A*, 295, 685
 Leitherer, C. 1998, in *38th Herstmonceux Conference, The Stellar Initial Mass Function*, ed. G. Gilmore, I. Parry, & S. Ryan (San Francisco: ASP), 61
 Leitherer, C., et al. 1996a, *PASP*, 108, 996
 Leitherer, C., Chapman, J., & Koribalski, B. 1995, *ApJ*, 481, 898
 Leitherer, C., Fritze-v. Alvensleben, U., & Huchra, J. 1996b, *From Stars to Galaxies—The Impact of Stellar Physics on Galaxy Evolution* (San Francisco: ASP)
 Leitherer, C., & Heckman, T. M. 1995, *ApJS*, 96, 9 (LH95)
 Leitherer, C., Robert, C., & Drissen, L. 1992, *ApJ*, 401, 596
 Leitherer, C., Robert, C., & Heckman, T. M. 1995, *ApJS*, 99, 173
 Lejeune, T., Buser, R., & Cuisinier, F. 1997, *A&AS*, 125, 229
 Maeder, A. 1990, *A&AS*, 84, 139
 ———. 1992, *A&A*, 264, 105
 ———. 1995, in *Astrophysical Applications of Stellar Pulsation*, ed. R. S. Stobie & P. A. Whitelock (San Francisco: ASP), 1
 Maeder, A., & Meynet, G. 1994, *A&A*, 287, 803

- Mayya, Y. D. 1997, *ApJ*, 482, 149
- Meynet, G. 1995, *A&A*, 298, 767
- Meynet, G., Maeder, A., Schaller, G., Schaerer, D., & Charbonnel, C. 1994, *A&AS*, 103, 97
- Möller, C., Fritze-v. Alvensleben, U., & Fricke, K. J. 1997, *A&A*, 317, 676
- Moorwood, A. F. M. 1996, *Space Sci. Rev.*, 77, 303
- Origlia, L., Goldader, J. D., Leitherer, C., Schaerer, D., & Oliva, E. 1998, *ApJ*, 514, 96
- Origlia, L., Moorwood, A. F. M., & Oliva, E. 1993, *A&A*, 280, 536
- Pettini, M., Steidel, C. C., Dickinson, M. E., Kellog, M., Giavalisco, M., & Adelberger, K. L. 1997, in *The Ultraviolet Universe at Low and High Redshift*, ed. W. H. Waller, M. N. Fanelli, J. E. Hollis, & A. C. Danks (Woodbury: AIP), 279
- Robert, C. 1999, in *IAU Symp. 193, Wolf-Rayet Phenomena in Massive Stars and Starburst Galaxies*, ed. K. A. van der Hucht, G. Koenigsberger, & P. R. J. Eenens (San Francisco: ASP), in press
- Robert, C., Leitherer, C., & Heckman, T. M. 1993, *ApJ*, 418, 749
- Sahnow, D. J., Friedman, S. D., Oegerle, W. R., Moos, H. W., Green, J. C., & Siegmund, O. H. 1996, *Proc. SPIE*, 2807, 2
- Salpeter, E. E. 1955, *ApJ*, 121, 161
- Scalo, J. 1998, in *38th Herstmonceux Conference, The Stellar Initial Mass Function*, ed. G. Gilmore, I. Parry, & S. Ryan (San Francisco: ASP), 201
- Schaerer, D., Charbonnel, C., Meynet, G., Maeder, A., & Schaller, G. 1993a, *A&AS*, 102, 339
- Schaerer, D., & de Koter, A. 1997, *A&A*, 322, 598
- Schaerer, D., Meynet, G., Maeder, A., & Schaller, G. 1993b, *A&AS*, 98, 523
- Schaerer, D., & Vacca, W. D. 1998, *ApJ*, 497, 618
- Schaller, G., Schaerer, D., Meynet, G., & Maeder, A. 1992, *A&AS*, 96, 269
- Schmidt-Kaler, T. 1982, in *Landolt-Börnstein, New Series, Group VI, Vol. 2b*, ed. K. Schaifers & H. H. Voigt (Berlin: Springer), 1
- Schmutz, W., Leitherer, C., & Gruenwald, R. 1992, *PASP*, 104, 1164
- Shull, J. M., & Saken, J. M. 1995, *ApJ*, 444, 663
- Smith, L. F., & Hummer, D. G. 1988, *MNRAS*, 230, 511
- Smith, L. F., & Maeder, A. 1991, *A&A*, 241, 77
- Stasińska, G., & Leitherer, C. 1996, *ApJS*, 107, 427
- Stasińska, G., & Schaerer, D. 1997, *A&A*, 322, 615
- Thornton, K., Gaudlitz, M., Janka, H.-Th., & Steinmetz, M. 1998, *ApJ*, 500, 95
- Vanbeveren, D., Van Bever, J., & de Donder, E. 1997, *A&A*, 317, 487
- Walborn, N. R., & Bohlin, R. C. 1996, *PASP*, 108, 477
- Weedman, D. W. 1987, in *Star Formation in Galaxies*, ed. C. J. Lonsdale (Washington: NASA), 351
- Weedman, D. W., Feldman, F. R., Balzano, V. A., Ramsey, L. W., Sramek, R. A., & Wu, C.-C. 1981, *ApJ*, 248, 105